Titre: Title:	Development of a Durable Thin-on-Thick Icephobic Coating System for Aerospace Applications
Auteur: Author:	Stephen Brown
Date:	2018
Type:	Mémoire ou thèse / Dissertation or Thesis
Référence: Citation:	Brown, S. (2018). Development of a Durable Thin-on-Thick Icephobic Coating System for Aerospace Applications [Mémoire de maîtrise, École Polytechnique de Montréal]. PolyPublie. https://publications.polymtl.ca/3718/

URL de PolyPublie: PolyPublie URL:	https://publications.polymtl.ca/3718/
Directeurs de recherche: Advisors:	Ludvik Martinu, & Jolanta-Ewa Sapieha
Programme: Program:	Génie physique

UNIVERSITÉ DE MONTRÉAL

DEVELOPMENT OF A DURABLE THIN-ON-THICK ICEPHOBIC COATING SYSTEM FOR AEROSPACE APPLICATIONS

STEPHEN BROWN

DÉPARTEMENT DE GÉNIE PHYSIQUE

ÉCOLE POLYTECHNIQUE DE MONTRÉAL

MÉMOIRE PRÉSENTÉ EN VUE DE L'OBTENTION

DU DIPLÔME DE MAÎTRISE ÈS SCIENCES APPLIQUÉES

(GÉNIE PHYSIQUE)

DÉCEMBRE 2018

UNIVERSITÉ DE MONTRÉAL

ÉCOLE POLYTECHNIQUE DE MONTRÉAL

Ce mémoire intitulé :

DEVELOPMENT OF A DURABLE THIN-ON-THICK ICEPHOBIC COATING SYSTEM FOR AEROSPACE APPLICATIONS

présenté par : BROWN Stephen

en vue de l'obtention du diplôme de : Maîtrise ès sciences appliquées

a été dûment accepté par le jury d'examen constitué de :

M. PETER Yves-Alain, D. Sc., président

Mme KLEMBERG-SAPIEHA Jolanta-Ewa, Doctorat, membre et directrice de recherche

M. MARTINU Ludvik, Ph. D., membre et codirecteur de recherche

M. ROBERT Étienne, Ph. D., membre

ACKNOWLEDGEMENTS

I would like to thank my directors, Jolanta Sapieha and Ludvik Martinu, for providing me with valuable insights and support throughout my project, as well as giving me the opportunity to participate in this project which has travelled me more kilometers than any other undertaking in my life. In addition, I would like to thank all of the collaborators in the Phobic2Ice project, in particular Navid, Hani, and Ali from Concordia, for providing me with a multitude of samples, and allowing me the many hours spent at their icing wind tunnel. I'd also like to thank Alex Laroche, for repeatedly honoring my last-minute requests for more details on the rain erosion and ice adhesion tests.

I would like to thank all of my LARFIS colleagues, especially Jacques Lengaigne, who introduced me to the core concepts of icephobicity, and continued to send me articles up until the completion of this thesis. He also forced deadlines on me and let me know that "You have too many results already! You need to start writing!" All of these things were very much appreciated. I'd like to thank Damian Batory, Antonin Riera, and Henri Cardinal-Pilote for making the summers more productive and more enjoyable.

I would like to thank Sara, for being by my side through this whole journey, from program acceptance to scrambled completion.

Finally, I would like to thank my parents, whose continued support allows me to partake in adventures such as the one detailed over the next hundred or so pages.

RÉSUMÉ

La formation de glace sur les composants des aéronefs est un problème majeur dans l'aviation depuis ses débuts et continue de nuire à ce secteur aujourd'hui. La cause principale de la formation de glace est les gouttelettes en surfusion qui se trouvent suspendues dans les nuages. La basse température de l'air à haute altitude et l'absence de sites de nucléation dans les nuages permettent aux gouttelettes d'eau de se refroidir jusqu'à -40 °C sans jamais geler. Ces gouttelettes sont dans un état très instable et vont se geler presque instantanément à la surface d'un avion qui vole dans ce type de nuage. Le givrage des avions diminue la portance tout en augmentant le poids, la traînée et la consommation de carburant. Cela peut également faire en sorte de geler les pièces mobiles ensemble ou de bloquer les entrées d'air, provoquant des pannes mécaniques et même des accidents. Bien qu'il existe des solutions actives de prévention et d'élimination de la glace, celles-ci ajoutent du poids et de la complexité à l'aéronef, et ne sont pas compatibles avec tous les composants. Pour cette raison, une solution passive est souhaitable.

De nombreuses stratégies ont été proposées pour développer des surfaces antigel, et parmi celles-ci, l'utilisation de surfaces superhydrophobes est l'une des plus prometteuses. Les surfaces superhydrophobes sont extrêmement hydrofuges, permettant à l'eau de rouler sur leur surface comme une bille sur du bois. Il a été démontré qu'ils retardent la formation de glace sur les surfaces et réduisent l'adhérence de la glace formée. Le principal obstacle à l'utilisation des surfaces superhydrophobes est leur faible durabilité.

Le but de ce travail est de développer un revêtement durable qui démontre de la glaciophobicité à travers de la superhydrophobicité. Ceci est réalisé en utilisant un système de revêtement « mince-sur-épais » qui consiste en un revêtement épais de TiO2 (~ 50 µm) déposé par projection plasma en suspension, et une superposition de couches minces déposées par dépôt chimique en phase vapeur assisté par plasma. Il a été démontré dans des travaux antérieurs que le revêtement de TiO2 par projection plasma en suspension présentait une rugosité hiérarchique et qu'il était superhydrophobe lorsqu'il était recouvert d'une couche de finition hydrophobe. La superposition de couches minces est constituée de trois couches: une couche inférieure en SiNx de 150 nm, pour une adhérence améliorée, une couche intermédiaire DLC: SiOx à 250 nm à dureté et mouillabilité réglables, et une couche de finition de 100 nm d'hexaméthyldisiloxane polymérisée au plasma qui est souple, mais très hydrophobe. D'abord, le développement de cette superposition de revêtements

y est exploré en détail. Puis, la glaçiophobicité du système de revêtement complet est prouvée par des tests d'adhérence de glace. Finalement, la durabilité supérieure par rapport aux autres surfaces superhydrophobes est démontrée par des tests d'érosion par pluie et des cycles de givrage/dégivrage dans une soufflerie de givrage.

ABSTRACT

The formation of ice on aircraft components has been a major issue in aviation since its beginning, and continues to plague the industry today. A leading cause of ice formation is supercooled droplets suspended in clouds. The low air temperature at high altitudes and lack of nucleation sites in clouds means that water droplets can cool to as low as -40°C without ever freezing. These droplets are in a very unstable state and will freeze almost instantly to the surface of an aircraft as it flies through an icing cloud. Icing on aircraft decreases lift, while increasing weight, drag, and fuel consumption. It can also freeze moving parts together or freeze over air intakes, resulting in mechanical failures and even crashes. While active solutions for ice prevention and removal do exist, these add weight and complexity to the aircraft, and are not compatible with all components. For this reason, a passive solution is desirable.

Many different strategies have been proposed for developing anti-icing surfaces, and of these, the use of superhydrophobic surfaces is among the most promising. Superhydrophobic surfaces are highly water-repellent, allowing water to roll across their surface like a marble on wood. They have been shown to delay the formation of ice on surfaces, as well as decreasing the adhesion of ice which is formed. Their main barrier to usage is their low durability.

The aim of this work is to develop a durable coating which exhibits icephobicity via superhydrophobicity. This is achieved by using a thin-on-thick coating system which consists of a thick (~50 µm) TiO_2 coating deposited by suspension plasma spray, and a thin coating stack deposited by plasma-enhanced chemical vapor deposition. The suspension plasma spray TiO_2 coating has been shown in previous works to exhibit hierarchical roughness and is superhydrophobic when coated with a hydrophobic topcoat. The thin stack is newly developed, and consists of three layers: a 150 nm SiN_x bottom layer for improved adhesion, a 250 nm DLC:SiOx middle layer with tunable hardness and wettability, and a soft but highly hydrophobic 100 nm plasma polymerized hexamethyldisiloxane topcoat. Development of this coating stack is explored in detail, while the icephobicity of the full coating system is shown through ice adhesion tests, and a superior durability compared to other superhydrophobic surfaces is shown through rain erosion tests and icing/deicing cycles in an icing wind tunnel.

TABLE OF CONTENTS

ACKNOWLEDGEMENTS III

RÉSUMÉ IV

ABSTRACT VI

TABLE OF CONTENTS VII

LIST OF TABLES X

LIST OF FIGURES XII

LIST OF SYMBOLS AND ABBREVIATIONS XVIII

CHAPTER 1 INTRODUCTION 1

1.1 Project context 4

1.2 Research objectives 4

1.3 Thesis outline 5

CHAPTER 2 LITERATURE REVIEW 6

2.1 Hydrophobicity and superhydrophobicity 6

2.1.1 Surface wettability and contact angle 7

2.1.2 Effect of roughness 9

2.1.3 Superhydrophobic surfaces 11

2.1.4 Reentrant topography 18

2.1.5 Superhydrophobicity in practice 19

2.2 Icing & icephobicity 23

2.2.1 Ice adhesion 26

2.2.2 Ice accretion 34

2.2.3 Freezing delay 36

2.2.4 Durability of icephobic surfaces 38

2.3 HMDSO and DLC:SiO_x coatings 44
2.4 Fabrication methods 51
2.4.1 Plasma-enhanced chemical vapor deposition 51
2.4.2 Thermal Spray 52
CHAPTER 3 METHODOLOGY 55
3.1 Coating deposition 55
3.1.1 Plasma-enhanced chemical vapor deposition 55
3.1.2 Suspension-plasma-spray 57
3.1.3 Other depositions 58
3.2 Physical Characterization 58
3.2.1 Optical interferometry and roughness calculations 58
3.2.2 Mechanical profilometry 61
3.2.3 Scanning electron microscopy 61
3.2.4 Water contact angle measurements 62
3.2.5 Nanoindentation 62
3.2.6 X-ray photoelectron spectroscopy 63
3.3 Icephobicity & Durability tests 64
3.3.1 Icing/Deicing cycles 64
3.3.2 Ice adhesion 65
3.3.3 Rain erosion 66
CHAPTER 4 DEVELOPMENT AND TESTING OF DURABLE ICEPHOBIC COATINGS. 68
4.1 Plasma-polymerized HMDSO 68
4.1.1 Effect of bias 68
4.1.2 Effects of pressure and HMDSO flow 70

4.1.3 HMDSO coating summary 71
4.2 Development of DLC:SiO_x coatings 72
4.2.1 Hydrophobic DLC:SiO_x coatings 73
4.2.2 Properties of final coatings and other remarks 76
4.3 Deposition on Suspension Plasma Spray TiO_2 78
4.3.1 Maximum coating thickness 80
4.3.2 Deposition of thin-on-thick coating system 82
4.4 Sample performance in durability and icephobicity testing 83
4.4.1 Ice adhesion 84
4.4.2 Rain erosion 87
4.4.3 Durability in icing/de-icing cycle tests 89
4.5 General discussion 97
CHAPTER 5 CONCLUSIONS AND FURTHER SUGGESTIONS 100
BIBLIOGRAPHY 102

LIST OF TABLES

Table 2.1: Feature sizes and measured contact angle vs. Cassie-Baxter calculated contact angle for nano-pillar surface. 21

Table 2.2: Conditions for greatest risk of icing. 23

Table 2.3: Two theoretical superhydrophobic surfaces, showing the potential mis-alignment of CAH and θ_{rec}. 33

Table 2.4: Changes to CA, sliding angle, average height (h), average roughness (R_a) before and after multiple icing/deicing cycles. 41

Table 2.5: XPS measurements of elemental composition of the surface before and after cycling. 44

Table 3.1: Icing conditions for icing/deicing cycling. 65

Table 4.1: Conditions used for DLC deposition. 72

Table 4.2: Properties of several DLC:SiO_x coatings. Samples "SB_170508_DLC2" and "SB_170529_DLC1" were determined to be the most promising. 77

Table 4.3: Roughness parameters for a SPS TiO_2 surface. 79

Table 4.4 : Effect of coating thickness on samples wettability. 81

Table 4.5: Wettability properties of SPS TiO_2 with different stacks. 82

Table 4.6: Surface roughness properties before and after coating. 83

Table 4.7: Icing conditions for ice adhesion tests. 84

Table 4.8: Ice adhesion for balanced, hard, and stearic acid coatings in 4 different icing conditions. 86

Table 4.9: Number of droplet impacts required for water to adhere to surface for all samples and droplet velocities. 88

Table 4.10: Icing Wind Tunnel conditions for icing/deicing cycles 89

Table 4.11: Cycles required for one or all droplets to stick to sample surface during contact angle hysteresis measurements. 91

Table 4.12: Roughness properties of the balanced stack before and after cycling. 95

Table 4.13: Identification and quantification of elements from XPS survey scans 96

Table 4.14: Identification of chemical bonding from high resolution XPS scans 96

LIST OF FIGURES

Figure 1.1: Icing on the leading edge of an airplane wing. 1

Figure 1.2: Common active methods for ice removal, including a) pneumatic boots, b) heating systems, and c) manual deicing. 2

Figure 1.3: Droplet of liquid mercury on a taro leaf, demonstrating Cassie-Baxter wetting and the "lotus effect". 3

Figure 2.1: Schematic of Young's equation showing the contact angle as a function of the solid-liquid, solid-vapor, and liquid-vapor interfacial energies. The contact angle is measured as the angle between the solid-liquid and the liquid-vapor interface. 8

Figure 2.2: The effect of Wenzel roughness. a) Hydrophilic and b) hydrophobic flat surfaces, and a c) rough hydrophobic surface exhibiting Wenzel wetting. 10

Figure 2.3: The effect of Cassie-Baxter roughness. a) Hydrophobic flat surface, b) a rough hydrophobic surface exhibiting Wenzel wetting, and c) a rough hydrophobic surface exhibiting Cassie-Baxter wetting. 10

Figure 2.4: The first SEM image captured of a lotus leaf, detailing its hierarchical roughness. ... 12

Figure 2.5: Wenzel (a) and Cassie-Baxter (b) wetting, as well as the lotus-style Cassie-Baxter wetting resulting from hierarchical roughness (c). 12

Figure 2.6: The Gibbs energy for a water droplet on a rough surface. 13

Figure 2.7: Droplet inflation/deflation method for measuring CAH. The initial droplet and beginning of droplet inflation can be seen in a) and b). At some point, the baseline begins to advance, and the advancing CA can be measured during this time. After the droplet is fully inflated, deflation begins as seen in d). The baseline decreases as in e), and the receding contact angle can be measured from the last frame before the baseline change. It is important to note that when the droplet size becomes too small (< 3µl), its shape will be highly distorted from its contact with the needle, and measurements taken at this point are not valid (f). 15

Figure 2.8: Tilting method for contact angle hysteresis measurement. α represents the roll-off angle, and the points of measurement for the advancing (θ_{adv}) and receding (θ_{rec}) contact angles are indicated. 16

Figure 2.9: A droplet suspended from a surface which exhibits Wenzel-type wetting. The droplet adheres to the surface even when tilted to 180 °. 17

Figure 2.10: SEM images of silicon surfaces etched to give them reentrant topography. 18

Figure 2.11: Three cases of reentrant topography. Shows the effects of a) $\theta_{overhang} > \theta_{flat}$, b) $\theta_{overhang} = \theta_{flat}$, c) $\theta_{overhang} < \theta_{flat}$. 19

Figure 2.12: Definition of a unit cell for the calculation of the CB fractional area φ_s. *S* is the center-to-center distance between pillars, *d* is the diameter of a pillar top. 20

Figure 2.13: Water droplet bouncing on a superhydrophobic surface. 21

Figure 2.14: Three different surface patterns used to test droplet bouncing. a) small, dense pillars, b) larger, sparse pillars and c) closed-cell bricks. Inlays show contact angle and droplets bouncing off of each surface. 22

Figure 2.15: Average supercooled liquid water content in clouds across the globe. 24

Figure 2.16: Persons/km^2 on Earth in 2015, as modelled by Gridded Population of the World (GPW) v4. 24

Figure 2.17: Glaze, mixed, and rime ice formed on steel plates (top) and aerodynamic profiles (bottom). 25

Figure 2.18: A common method for testing the adhesion strength of a surface. a) Water is poured into molds which are then placed in direct contact with the samples. b) Water is frozen onto the surface, whether via Peltier plate or simply by placing samples in a freezer. (c) The molds are removed, and a force transducer is used to apply a force until the ice breaks or is dislodged. This force is noted, and from this an ice adhesion strength value is obtained. 27

Figure 2.19: A breakdown of ice adhesion values reported in the literature for different types of surfaces. 28

Figure 2.20: Finite element strain analysis for ice on PDMS films. The locations of possible crack initiation for a homogenous film are shown in a), while b) shows that MACI causes macroscopic cracks at multiple locations along the interface. The black arrows are representative of the forces applied. 30

Figure 2.21: Ice adhesion vs. Areal fraction for hydrophobic nano-pillars. Also shown are SEM cross-sections and tilted images, as well as droplet images for each pillar size. 31

Figure 2.22: Ice adhesion for hydrophobic and superhydrophobic samples. Circles show samples which were spray-coated, whereas triangles are spin-coated samples. a) Shows that there is no correlation between CA and sheer stress, while b) shows a clear correlation between CAH and shear stress. 32

Figure 2.23: Values for ice adhesion strength as a function of θ_{rec} for 33 different samples across three labs. $R^2 = 0.92$. 33

Figure 2.24: High-speed images of droplet impact at freezing temperatures for a) hydrophilic, b) hydrophobic, and c) superhydrophobic surfaces. 35

Figure 2.25: a) Time required for four superhydrophobic or near-superhydrophobic surfaces to form a uniform layer of ice. B) Sample St-SHC after 90 seconds of icing, compared to uncoated sample. 36

Figure 2.26: Time required for a 5 µl droplet to freeze on nanopillars at -20 °C. 37

Figure 2.27: Time to freeze a 7 µl water droplet on a -10 °C surface with micro- and nano-scale features (MN-), a surface with only nano-scale features (N-), only micro-scale features (M-), and a smooth surface (S). 38

Figure 2.28: Ice adhesion on anodized aluminium with HMDSO coating, over 15 icing/deicing cycles. 39

Figure 2.29: Anodized aluminium with HMDSO coating a) before and b) after 15 icing/deicing cycles. 40

Figure 2.30: Comparison of changes in ice adhesion over a) 20 cycles deicing by forced ice removal b) 40 cycles deicing by melting. 40

Figure 2.31: Degradation mechanism of the etched aluminium surface. Nano-scale asperities are broken during icing/deicing cycling. 41

Figure 2.32: Contact angle and contact angle hysteresis over 20 icing/deicing cycles for micropillars (diamonds) and honeycomb cells (triangles). 42

Figure 2.33: Degradation of surface via a) shear stress (ice adhesion) and b) contact angle and hysteresis measurements after 15 icing/deicing cycles. 43

Figure 2.34: HMDSO-coated anodized aluminium a) before and b) after 15 icing/deicing cycles. 43

Figure 2.35 : Ball and stick model of hexamethyldisiloxane molecule. 44

Figure 2.36: Contact angle and chemical ratios (via FT-IR) for plasma-polymerized HMDSO… 45

Figure 2.37: AFM images of etched silicon a) before and b) after 50nm coating with PP-HMDSO. Preferential nucleation at the sites of surface features creates "globs" which smooth the surface. 46

Figure 2.38: The types of DLC which can be deposited depending on the content of sp^2 carbon bonds, sp^3 carbon bonds, and hydrogen. 48

Figure 2.39: Microhardness for commonly deposited materials, with a-C:H highlighted. Depending on deposition conditions, a-C:H may be soft or hard, but will not be superhard. 48

Figure 2.40: Contact angle as a function of O/Si atomic concentration ratio. Black-filled shapes are deposited by capacitively coupled PECVD, grey-filled shapes by high-frequency PECVD, and unfilled shapes by closed drift ion beam. Different shapes indicate that the data comes from different sources. 50

Figure 2.41: Schematic of a simple PECVD deposition. Positively charged particles are present in the plasma. These particles then adsorb to the surface, desorption of some species may occur, and gaseous by-products are extracted by the vacuum system. 52

Figure 2.42: The steps of thermal spray deposition. 53

Figure 2.43: SEM image of thermal sprayed MCrAlY, coated with a low surface energy material. Inset shows the contact angle of this surface. 54

Figure 3.1: Schematic of the PECVD deposition system. 56

Figure 3.2: PECVD chamber, showing both the biased (bottom) and grounded (top) electrodes. 57

Figure 3.3: Schematic of an optical interferometer. 59

Figure 3.4: Profiles associated with negative and positive skewness. 60

Figure 3.5: Profiles associated with kurtosis values less than and greater than 3. 61

Figure 3.6 Load-displacement curve. 63

Figure 3.7: The icing wind tunnel at Concordia University. Inlay shows the nozzle. 64

Figure 3.8: a) Focused water jet cut into segments by rotating disk. b) pattern used for number of impacts. 67

Figure 4.1: Contact angle of grounded and biased samples as a function of electrode bias. The red line indicates the 109.4° value obtained for a fluoropolymer coating. 69

Figure 4.2: Deposition rate of grounded and biased samples as a function of electrode bias. 69

Figure 4.3: Contact angle and deposition rate for biased and grounded samples as a function of HMDSO partial pressure. 70

Figure 4.4: Contact angle and deposition rate for 150 and 200 mTorr working pressures as a function of bias. 71

Figure 4.5: Bias vs. contact angle and hardness for DLC:SiO_x samples. Also shown are the deposited films on glass slides. 73

Figure 4.6: Contact angle as a function of bias and HMDSO partial pressure. At working pressure of 50 mTorr was used for the measurements where the HMDSO partial pressure is varied. 74

Figure 4.7: Contact angle dependence on bias and HMDSO flow at 50 and 100 mTorr. 75

Figure 4.8: Contact angle dependence on bias and HMDSO flow with 5 sccm C_2H_2 at 25 mTorr chamber pressure. 76

Figure 4.9: DLC:SiO_x coating on Ti-6Al-4V after contact angle measurements. a) Without interlayer, film delaminates easily, b) with interlayer, coating adheres well to the surface. .77

Figure 4.10: SPS TiO_2 a) without and b) with a hydrophobic coating 78

Figure 4.11: Surface profile scan of a non-coated TiO_2 surface at 5x. 79

Figure 4.12: Suspension plasma sprayed TiO2 surface, without any topcoat. 80

Figure 4.13: SPS TiO_2 a) without coating, b) with 0.5 µm coating, c) with 1 µm coating, and d) with 2 µm coating. The reduction of nanoscale roughness is clear as coatings become thicker. 81

Figure 4.14: Schematic the coating system used for icephobicity and durability testing 82

Figure 4.15: Surface profile of TiO_2 at 20x a) before and b) after coating with balanced stack. ..83

Figure 4.16: Iced surfaces showing a) rime b) mixed/rime c) mixed glaze and d) glaze ice obtained in the Airbus icing wind tunnel. 85

Figure 4.17: a) balanced stack b) hard stack and c) stearic acid samples after rain erosion tests and dipping samples into deionized water. Droplet velocities are 165, 180, 200, and 225 m/s, moving clockwise from the top left. Impacts are in rows of five, for 20, 50, 100, 250, 500, 1000, 2000, 3000, and 6000 impacts, from the bottom of each group. 87

Figure 4.18: Balanced stack, stearic acid, and HMDSO stack TiO_2 samples used for icing/deicing cycling. 89

Figure 4.19: SPS TiO_2 samples installed in IWT a) before and b) after 1 minute of icing.....90

Figure 4.20: Contact angle (top) and contact angle hysteresis (bottom) for tested samples after up to 170 icing/deicing cycles. 91

Figure 4.21: Water adhering to the surface after CAH measurement for a) stearic acid after 70 cycles, b) HMDSO coating after 70 cycles and c) HMDSO coating after 170 cycles. 92

Figure 4.22: SEM images of the balanced stack sample before (left) and after (right) 170 icing/deicing cycles. 93

Figure 4.23: SEM images of the stearic acid sample before (left) and after (right) 170 icing/deicing cycles. 94

LIST OF SYMBOLS AND ABBREVIATIONS

a-C:H	Hydrogenated Amorphous Carbon
BE	Binding Energy
CA	Contact Angle
CAH	Contact Angle Hysteresis
CB	Cassie-Baxter
CVD	Chemical Vapor Deposition
CH_3	Methyl group
DLC	Diamond-like carbon
DLC:SiO_x	Silicon and oxygen networked diamond-like carbon
EDX	Energy Dispersive X-ray Spectroscopy
ER	Erosion Rate
HMDSO	Hexamethyldisiloxane
HVOF	High-velocity oxyfuel
IWT	Icing Wind Tunnel
MVD	Median volume diameter
PDMS	Polydimethylsiloxane
PECVD	Plasma-enhanced chemical vapor deposition
PVD	Physical Vapor Deposition
RoA	Roll-off Angle
RF	Radio Frequency
RMS	Root Mean Square
SEM	Scanning Electron Microscopy
SHS	Superhydrophobic Surface

SPS	Suspension plasma spray
SPE	Solid Particle Erosion
SLD	Supercooled Large Droplets
SWD	Supercooled Water Droplets
XPS	X-ray photoelectron spectroscopy

Symbols

S_a	Average surface roughness
S_{ku}	Kurtosis
S_q	RMS surface roughness
S_{sk}	Skewness
S_z	Maximum peak-to-valley surface roughness
γ	Interfacial Energy
r	Ratio of surface area to projected surface area
φ_s	Fraction of a surface in contact with water droplet
θ_a	Advancing contact angle
θ_r	Receding contact angle

CHAPTER 1 INTRODUCTION

Transportation and sub-zero temperatures have always been a tricky pair. A cursory glance through the literature will yield hundred-year-old scientific contributions detailing the struggles of dealing with ice for railways [1], sea vessels [2], and transportation in general [3]. As we push forward into the 1920's, a new challenge appears: icing on aircraft [4]–[6]. And while the field of aerospace has become dramatically more sophisticated in the past hundred years, icing remains an issue to this day.

While icing is hazardous in almost any circumstance, the potential for catastrophe when combined with flight is particularly high. Indeed, it has been found that 12% of all weather-related aircraft accidents in the United States are caused by icing, and of these, 27% are fatal. When accidents occur, it is almost always due to ice which forms in-flight; this is the cause of 92% of all icing accidents, compared to 8% resulting from ground accumulation of ice [7]. Further complicating the matter is the fact that the method of ice formation seen in-flight is not the same as those typically seen at ground level, where bodies of water slowly freeze, or temperature fluctuations around 0 °C cause melting of snow followed by icing of sidewalks.

Figure 1.1: Icing on the leading edge of an airplane wing. Taken from [8].

The leading cause of in-flight ice formation in aviation is supercooled water droplets suspended in clouds [9][10]. The low air temperature at high altitudes means that water droplets can cool to

temperatures as low as -40 °C without ever freezing [11]. This leads to droplets which are in a very unstable state, and any disturbance could provide the activation energy to begin ice nucleation. So, as an airplane contacts these supercooled droplets, they freeze easily to the surface. The practical issues presented by aircraft icing are many: it changes the profile of the airplane, decreasing lift and increasing drag and fuel consumption [12]; it adds weight to the airplane, again increasing fuel consumption [13]; and it can freeze over sensors, rendering them useless. It can also freeze moving parts together or freeze over air intakes, leading to mechanical failures and even crashes [7], [11]. Figure 1.1 shows a wing which has been subject to in-flight icing.

Currently, icing is dealt with through active techniques, the most common of which can be seen in Figure 1.2. These include pneumatic boots, which can be inflated to break the ice along leading edges [14], as well as surface heating techniques, which can use either electrical systems or engine bleed air to melt the ice and/or prevent its formation [15]. The issues with these solutions is that they require an increase in power or fuel usage, add weight to the plane, and are not compatible with all exposed surfaces; generally, they are used only with leading edges. Finally, the most well-known method is the of deicing planes after landing or before takeoff. While this ensures a safe take-off, it does not guarantee the prevention of more ice forming during flights, and the spraying of deicing chemicals is not environmentally friendly [16]. The preferred solution would be to use components which simply do not ice up in the first place.

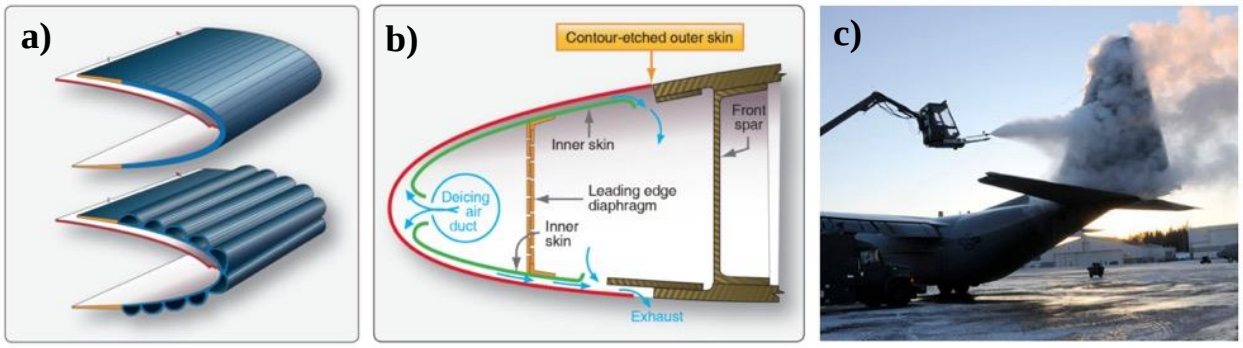

Figure 1.2: Common active methods for ice removal, including a) pneumatic boots, b) heating systems, and c) manual deicing. Taken from [14](a, b), [17] (c) .

Many different strategies have been proposed for developing passive anti-icing surfaces, and of these, superhydrophobic surfaces (SHS) are among the most promising [18][19]. A superhydrophobic surface is a surface which exhibits an extreme degree of water repellency,

allowing a droplet of water to roll across its surface like a marble across wood. They use a biomimetic design inspired by plants, in particular the lotus, whose leaves are covered with micro-scale bumps, which themselves are covered with grass-like nanostructures. The combination of these is often referred to as “hierarchical”, or “dual-scale” roughness. The structures are covered by a waxy film, and the combination of this with the surface morphology leads to extremely low water adhesion [20]. The low water adhesion comes from the fact that the water droplets are sitting on top of the micro-scale bumps, with air pockets present between the bumps. This is referred to as the Cassie-Baxter state for a droplet and can be seen in Figure 1.3. As a whole, this phenomenon is known as the “lotus effect”.

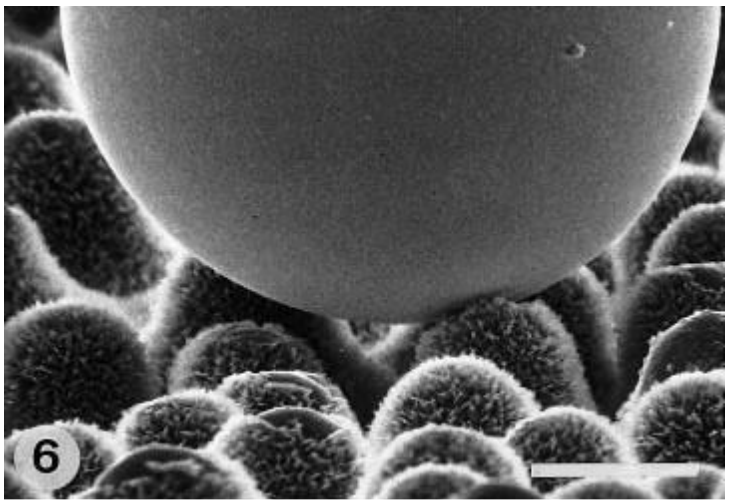

Figure 1.3: Droplet of liquid mercury on a taro leaf, demonstrating Cassie-Baxter wetting and the “lotus effect”. Scale bar is 20 μm. Taken From [21].

The relationship between superhydrophobicity and icephobicity is the result of multiple contributing factors. The first is the reduction of ice formation due to the low adhesion of water droplets with the surface: their high impact velocity and the shear force of the airflow in flight conditions means that droplets impinging on superhydrophobic surfaces can bounce off before having time to freeze, even at sub-zero temperatures [16][22]. A second factor is the reduction of ice adhesion strength. Ice which forms on a SHS will have the same air pockets which are present for water droplets, and as ice adhesion correlates with contact area, lowering this will lower the adhesion [23]. Finally, the air pockets between the micro-scale surface features promote the development of micro-cracks at the ice-solid interface, leading to easier ice removal [24]. The biggest barrier into aerospace usage for superhydrophobic surfaces is their low durability, which

depends on maintaining the nanoscale roughness as well as the desired surface chemistry [18]; addressing the durability issue is the aim of this work.

1.1 Project context

This work was performed within the context of the Phobic2Ice project, an international collaboration between five research partners and four industrial partners which aims to develop icephobic coatings for aerospace. The Canadian research partners include Polytechnique Montreal and Concordia University, while European research partners include the Consejo Superior de Investigaciones Científicas and Instituto Nacional de Técnica Aeroespacial in Spain, and the Technology Partners foundation in Poland. The Canadian industrial partners are Pratt & Whitney Canada, Plasmionique, and Dema Aeronautics, and the European industrial partner is Airbus Defence & Space. Phobic2Ice is funded by NSERC and CARIC in Canada, as well as by the European Union's Horizon 2020 research and innovation program.

1.2 Research objectives

With the overall aim of improving the durability of icephobic surfaces based on superhydrophobicity, the main objective of my project was defined as follows:

- Design coatings and coating systems for aircraft components which reduce ice adhesion to below 100 kPa, and which retain water droplet mobility after 50 icing/deicing cycles performed in an icing wind tunnel. The final solution must be compatible with existing aircraft components.

To achieve this main objective, a series of specific objectives were then defined:

1. Develop a coating which has properties of high hardness and hydrophobicity.
2. Coat hierarchically rough TiO_2 surfaces (provided by Concordia University) with the hard hydrophobic coating.
3. Characterize coated TiO_2 surfaces noting wettability, film thickness, chemical composition, and surface morphology.
4. Perform ice adhesion tests to verify the icephobicity of the surfaces.

5. Perform icing wind tunnel experiments to test the durability after numerous icing/deicing cycles.
6. Determine the degradation mechanism of surfaces due to icing/deicing cycling.

1.3 Thesis outline

This thesis is divided into five chapters, including the introduction. Chapter 2 will present a literature review, which aims to acquaint the reader with the idea of icephobicity, as well as to demonstrate some of the ways in which it is achieved. In particular, it will focus on surface wettability, beginning with the basic concepts of water-surface interaction, and building through to superhydrophobicity. This will be followed by a review of hexamethyldisiloxane-based films, as well as a look at the deposition techniques used in the project.

Chapter 3 will detail the methodologies used in the project, including coating deposition and characterization. A brief theoretical background will be presented for all of the systems used throughout the course of this thesis, as well as an explanation of the specific conditions used. It will close with a section on the icephobicity and durability tests used in this work.

Chapter 4 presents the main results of this thesis, that is, the development of a durable icephobic thin-on-thick coating system. It will detail both soft and hard thin hydrophobic coatings which have been developed, as well their deposition on thick TiO_2 coatings to create a thin-on-thick coating system. This coating system will be shown to provide a low ice adhesion, as well as showing a superior durability in icing/deicing tests and rain erosion tests compared to competing solutions.

Finally, chapter 5 will present the conclusions of this thesis, as well as looking at future work to be done on the subject.

CHAPTER 2 LITERATURE REVIEW

This chapter aims to provide the reader with the necessary background to understand the elements at play in the development and assessment of icephobic coatings. While the notion of a hydrophobic surface is well defined, there is no single accepted cause or definition for icephobicity. As such, there is a wide range of approaches used for both the development and validation of potentially icephobic surfaces. The current state of icephobic coatings will be presented, exploring the advantages and disadvantages of different design approaches and testing methodologies. The discussion of icephobicity will be prefaced by a discussion on superhydrophobicity, as icephobicity-by-superhydrophobicity is the experimental approach taken in this work.

Following the introduction to superhydrophobicity and icephobicity, this chapter will explore the use of hexamethyldisiloxane (HMDSO) to create hard, hydrophobic coatings. This will begin by looking at the deposition of hydrophobic coatings through the plasma polymerization of HMDSO and expand to the combination of HMDSO with diamond-like carbon (DLC) to deposit silicon- and oxygen-containing DLC, commonly referred to as DLC:SiO_x. The limitations on both hardness and hydrophobicity of such coatings will be explored, to determine benchmarks which are appropriate for the films developed as part of this work.

Finally, the specific deposition techniques used in this study will be discussed. First discussed will be plasma enhanced chemical vapor deposition (PECVD), which is used to deposit the thin coatings in this work, and this will be followed by a brief discussion of thermal spray techniques, used to deposit the thick coaintgs. If the reader would like to further broaden their knowledge of icephobic surfaces, it is highly recommended that they read Kreder *et al.*'s 2016 review "Design of anti-icing surfaces: smooth, textured or slippery?" [18], as well as what is in my opinion the most ground-breaking paper to be published on the subject in recent years, Irajizad *et al.*'s "Magnetic slippery extremely icephobic surfaces" [25].

2.1 Hydrophobicity and superhydrophobicity

Superhydrophobic surfaces arise from the combination of two distinct properties: surface chemistry and surface morphology. To fully develop the concept, this section will build up to superhydrophobicity by first looking at water-surface interactions for ideal flat surfaces. This will be followed by a discussion on the addition of roughness to surfaces, and the effects that this can

have based on their flat-surface wettability. This will be expanded into the exact properties needed to obtain superhydrophobicity, and will finish with a discussion on superhydrophobic surfaces in practice, and the effects of different patterning techniques.

2.1.1 Surface wettability and contact angle

When a liquid comes into contact with a solid, there is an interface which is formed. If we are not operating in a vacuum, there exists also the liquid-vapor interface which defines the boundaries of the droplet itself, and the solid-vapor interface. The relation between these will define whether a liquid droplet wets a surface or beads, and was first explained by Young in 1805 [26]. Young's equation examines the balance of these interfacial energies and uses this balance to define a "contact angle" (CA) between the liquid and the solid. The equation is defined as follows:

$$\cos(\theta) = \frac{\gamma_{sv} - \gamma_{sl}}{\gamma_{lv}} \tag{2.1}$$

where θ is the contact angle of the liquid with the surface, and γ_{sv}, γ_{sl}, and γ_{lv} are the specific energies of the solid-vapor, solid-liquid, and liquid-vapor interfaces, respectively. The point at which these interfaces meet is called the triple line, and it is here that the contact angle is defined. The balance between these energies and an illustration of how they affect the contact angle can be seen in Figure 2.1. The possible values of θ are bounded as $0\ ^\circ \leq \theta \leq 180\ ^\circ$, since $\theta = 0\ ^\circ$ would indicate a completely wetted surface, and $\theta = 180\ ^\circ$ would indicate an unwettable surface. Looking at equation (2.1), it then becomes apparent that if $\gamma_{sl} < \gamma_{sv}$, we have a positive value of $\cos(\theta)$ and thus a contact angle $\theta < 90\ ^\circ$. This makes sense, because we have defined the energy required to create a solid-vapor interface as higher than the energy required to create a solid-liquid interface, causing the droplet to increase the area of its solid-liquid interface by spreading along the surface. If we take the opposite situation, $\gamma_{sl} > \gamma_{sv}$, then the equation yields a contact angle $\theta > 90^\circ$. Considering that it is now our solid-liquid interface whose creation requires more energy, we will see a reduction in its area, and our droplet will bead on the surface. It is worth noting that this equation assumes both a perfectly flat and perfectly homogeneous surface.

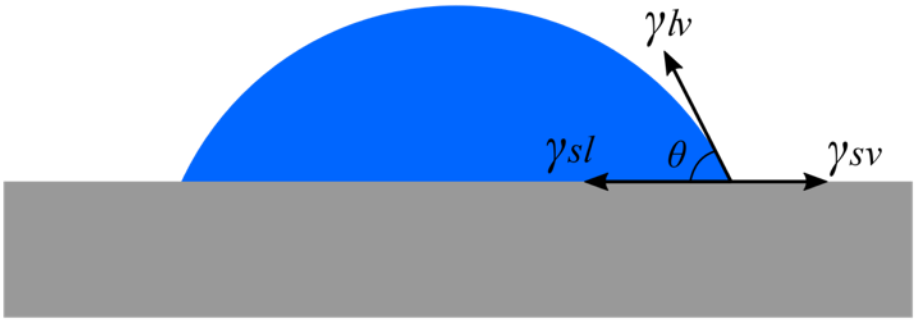

Figure 2.1: Schematic of Young's equation showing the contact angle as a function of the solid-liquid, solid-vapor, and liquid-vapor interfacial energies. The contact angle is measured as the angle between the solid-liquid and the liquid-vapor interfaces.

The most common type of contact angle measurement is performed using water as the liquid and air as the vapor. In this case, what we are measuring is specifically the water contact angle (WCA), and it is a very important property in any application where a surface is expected to come into direct contact with water. When the WCA of a surface is greater than 90°, that surface is said to bez` hydrophobic, and when it is less than 90°, that surface is said to be hydrophilic.

The water contact angle is a specific case of the surface energy and can thus be considered a property which is intrinsic to the material. Surface energy itself "arises from the imbalance of the force between atoms or molecules at the surface." [27] It is a sum of a polar component, which is a result of existing covalent bonds, hydrogen bonds, and dipole-dipole interactions, and a dispersive component, which is the result of Van der Walls interactions [27]. By definition, a low surface energy material will always have a high water contact angle, but a water contact angle measurement on its own is not enough to determine the surface energy of the material. This is because water is a primarily polar liquid and will not give information about the dispersive component of surface energy. To obtain the surface energy, contact angle measurements for at least one primarily dispersive liquid, such as diiodomethane, must also be performed [28].

In some cases, such as oleophobic (oil-repelling) or omniphobic (repellant of all liquids) surfaces, it is very important to be aware of both the polar and dispersive components of surface energy, as well as its total value, since a coating which is hydrophobic may also allow for easy wetting by other liquids such as hexadecane [29]. When dealing with surface which only need to repel water, however, it is sufficient to only perform contact angle measurements with water. Indeed, it is rare to find articles which focus on hydrophobicity and also give an exact value for surface energy.

Because of this, this thesis will use the term "contact angle" to mean "water contact angle" unless otherwise noted, and wettability will be reported in terms of water contact angle rather than surface energy.

It was previously mentioned that surfaces which repel water are said to be hydrophobic. As per Shafrin and Zisman [30], there are two types of surfaces which will give hydrophobicity:

1. Surfaces exposing only fluorine atoms.
2. Surfaces exposing only carbon and hydrogen atoms.

Of these, the first group is more hydrophobic, and it has been shown that the highest contact angle which can be achieved on a flat surface is 120°, for a perfluoronated monolayer [31]. In the case of a surface exposing only carbon and hydrogen atoms, the highest contact angle of 111° is achieved when the surface is comprised entirely of methyl groups (CH_3) [30].

2.1.2 Effect of roughness

While Young's equation assumes a perfectly flat surface, these are rarely encountered in reality. Moving beyond the inherent roughness of any surface, which should be kept in mind when making "flat sample" contact angle measurements, the addition of micro- and/or nano-scale features to a surface can have a drastic effect on its wettability. In general, the effect of roughness is to exaggerate the already-present contact angle properties of a surface. That is to say, if roughness is added to a hydrophilic surface, it becomes even more hydrophilic, and if it is added to a hydrophobic surface, it becomes even more hydrophobic.

In 1936, Wenzel developed an equation to determine the measured contact angle of a surface, based on the contact angle of a flat surface with the same chemical composition [32]. This became known as the Wenzel equation and defines the apparent contact angle of a rough surface as:

$$\cos(\theta^*) = r\cos(\theta) \tag{2.2}$$

where θ^* is the apparent contact angle, θ is the contact angle for a flat surface, and r is the ratio of the actual surface area to the projected surface area. Since any change to the surface can only increase its actual surface area, it is clear that r > 1 for any non-flat surface, and for a perfectly flat surface, $r = 1$ and $\theta^* = \theta$. Considering that real-world values for the flat-surface contact angle are $0° < \theta < 120°$, it also becomes apparent that an increase in roughness will cause any hydrophobic

surface ($\theta > 90$ °) to exhibit a higher contact angle than a chemically identical flat surface, while a surface which is initially hydrophilic ($\theta < 90$ °) will have its apparent contact angle decreased. Also important to understand about Wenzel-type wetting is that it describes the situation where water is able to fully wet the surface features below the droplet, as can be seen in Figure 2.2. This means that the droplet becomes anchored into the surface, and has a higher adhesion than on a flat surface of identical chemistry [33].

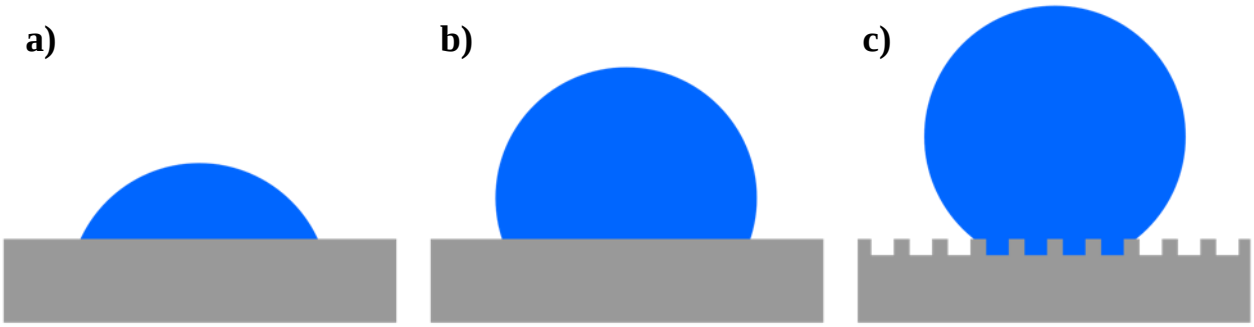

Figure 2.2: The effect of Wenzel roughness. a) Hydrophilic and b) hydrophobic flat surfaces, and c) a rough hydrophobic surface exhibiting Wenzel wetting.

In 1944, the effect of roughness was extended to porous surfaces by Cassie and Baxter [34]. While their work was on the subject of water repellency in clothing, it has since been applied to any situation where a water droplet sits on a composite solid-air interface, as demonstrated in Figure 2.3. The composite interface means that there are air pockets between surface features, and that only a fraction of the area under the droplet is actually in contact with the surface.

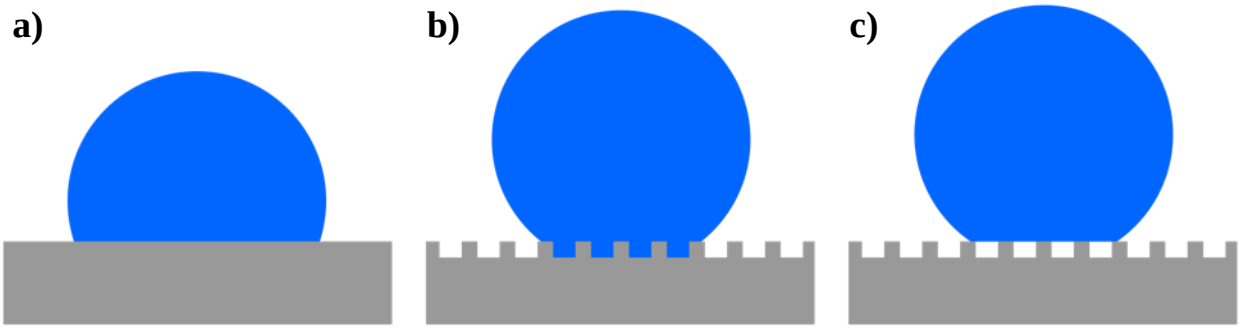

Figure 2.3: The effect of Cassie-Baxter roughness. a) Hydrophobic flat surface, b) a rough hydrophobic surface exhibiting Wenzel wetting, and c) a rough hydrophobic surface exhibiting Cassie-Baxter wetting.

The Cassie-Baxter equation is given by:

$$\cos(\theta^*) = -1 + \varphi_s[\cos(\theta) + 1] \quad (2.3)$$

where θ^* is again the apparent contact angle, θ is the contact angle for a flat surface, and φ_s is the solid fractional area of the interface which makes contact with the liquid. As with the Wenzel equation, the Cassie-Baxter equation reduces to $\theta^* = \theta$ when a flat surface is considered ($\varphi_s = 1$). Unlike the Wenzel equation, the Cassie-Baxter equation will give a value of $\theta^* > \theta$ if there is any surface roughness present. Because of this, it is important to be sure that Cassie-Baxter wetting is indeed happening if using this equation to describe a system. Compared to Wenzel wetting, it can also be seen in Figure 2.3 that the same "anchor" effect is not present. Instead, we have a reduction of solid-liquid contact area, which has the effect of reducing water adhesion compared to a flat surface of identical chemistry.

It should be noted that when a rough surface is being reported on in the literature, it is the apparent contact angle which is most regularly presented. Unless a study is specifically referencing the effect of morphology on a surface with known chemical properties, the "apparent" is dropped, and the term "contact angle" is used to describe the results obtained when performing goniometry on the sample. The system as a whole is considered, rather than dividing into chemical and morphological contributions.

2.1.3 Superhydrophobic surfaces

The next major breakthrough in understanding wettability came in 1997, with the identification of the physical principles behind "superhydrophobic" surfaces. While it has long been known that lotus leaves are extremely water-repellant, it was not until Barthlott and Neinhuis imaged a lotus leaf by SEM that the reason for this was understood [21]. Figure 2.4 shows this image, where we can clearly see micro-scale bumps along the surface, which themselves are covered in needle-like nano-scale hairs. This combination of micro and nano surface features has become known as hierarchical or dual-scale roughness [35]. When combined with the epicuticular wax which covers the lotus leaf, a surface is obtained which allows water roll across it with ease; this phenomenon is known as the lotus effect [21].

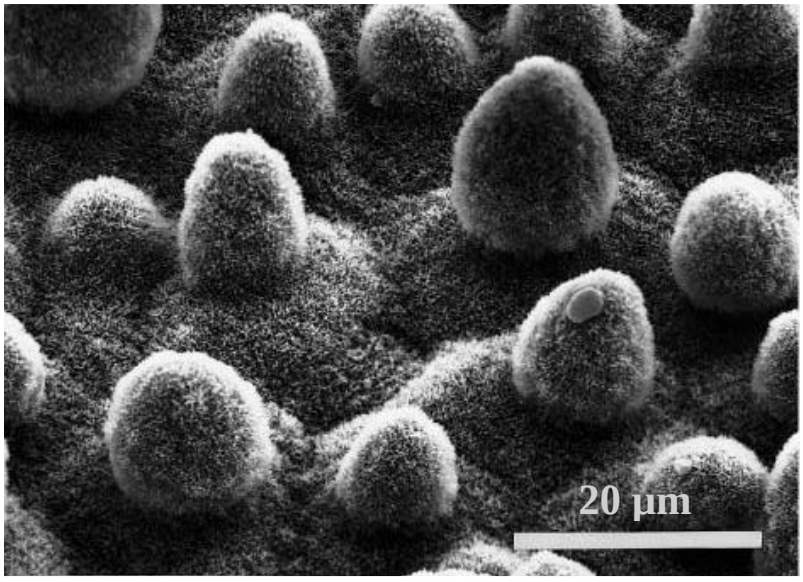

Figure 2.4: The first SEM image captured of a lotus leaf, detailing its hierarchical roughness. Taken from [21].

The reason for this low droplet adhesion can be seen in Figure 2.5, which compares lotus-style wetting with its Wenzel and Cassie-Baxter counterparts. In effect, lotus wetting it is an extension of the composite interface seen in Cassie-Baxter wetting, except that now the droplet is sitting on nano-scale – rather than micro-scale – surface features. This creates an even lower φ_s value, and the fact that water droplet has so little true contact with the surface means that it can easily roll across it. For this reason, these surfaces are also said to exhibit Cassie-Baxter wetting [36].

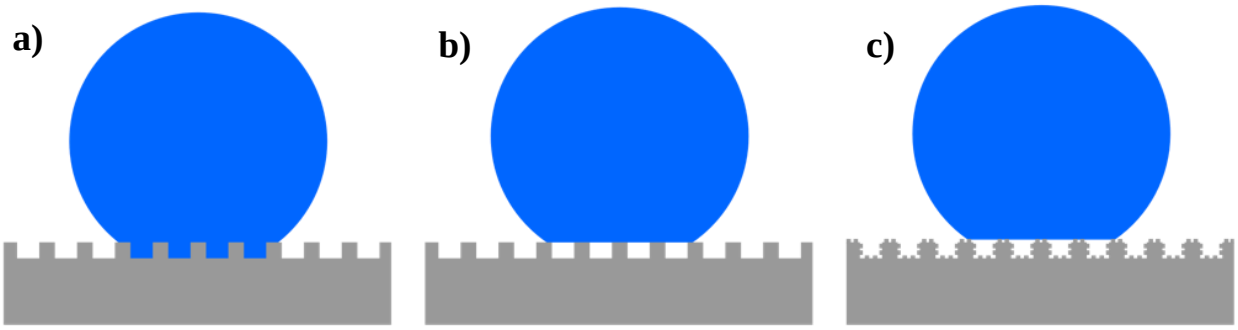

Figure 2.5: Wenzel (a) and Cassie-Baxter (b) wetting, as well as the lotus-style Cassie-Baxter wetting resulting from hierarchical roughness (c).

While the contact angle shows us how water sits on a surface, it tells us nothing about the mobility of droplets which are placed on it. To quantify the adhesion of a water droplet to a surface, a

measurement called the contact angle hysteresis (CAH) is used [37]. Contact angle hysteresis is defined via the advancing and receding contact angles, where

$$CAH = \theta_{adv} - \theta_{rec} \tag{2.4}$$

The advancing contact angle (θ_{adv}) is defined as the highest contact angle which can be measured on a surface. Similarly, the receding contact angle (θ_{rec}) is the lowest contact angle which can be measured on a surface. Both of these are metastable states which will only be achieved when some sort of external energy is applied to the system [38]. An illustration of this can be seen in the Gibbs energy for a water droplet on a rough surface in Figure 2.6. Because of this, these properties are sometime referred to as "dynamic" contact angle measurements, as opposed to the "static" most stable contact angle, achieved by simply placing a droplet onto the surface [39].

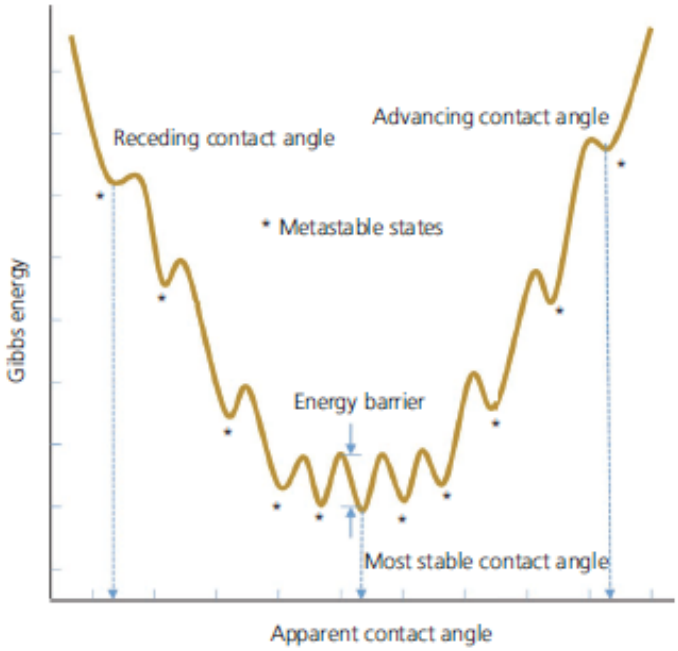

Figure 2.6: The Gibbs energy for a water droplet on a rough surface. Taken from [38].

In particular, the contact angle hysteresis is useful for determining what type of wetting is occurring on a surface. Indeed, the fundamental difference between Wenzel and CB wetting can be most easily seen by looking at the hysteresis measurements for corresponding samples [40]. A surface with Wenzel wetting will have a very high (CAH > 40°) or even unmeasurable hysteresis because the base of the droplet is anchored in place, and as such large external forces can be applied to the droplet, distorting its shape without causing the droplet to move and to return to a more stable state.

A surface with Cassie-Baxter wetting will have a low hysteresis (CAH < 10°), because with any disturbance the droplet simply rolls across the surface until it falls off or settles into a more stable state. A measurement similar to the contact angle hysteresis (though not directly related to it) is the roll-off angle (RoA), which is a represents the angle at which a sample must be tilted for a droplet to begin rolling off of the surface.

With definitions of contact angle and contact angle hysteresis in place, we can now define superhydrophobicity itself. The most common definition of a superhydrophobic surface is one which satisfies the following three conditions:

1. A contact angle greater than or equal to 150°.
2. A contact angle hysteresis less than or equal to 10°.
3. A roll-off angle less than or equal to 10°. [41]

It should be noted that there is not a full consensus on these last two points in the literature. Some authors present only their hysteresis results [42][43][44], while others state only the roll-off angle [45][46][20]. In the author's experience, CAH is always higher than RoA, and as such, it can be difficult to be sure that a surface is indeed superhydrophobic when only the RoA is reported, especially if its value is close to the 10° cut-off point. Beyond this, the literature is ripe with publications which call their surfaces "superhydrophobic", but state only the contact angle, specifying neither a CAH nor a RoA value [47][48][49]. In this case it is literally impossible for the reader to be sure of the sample's superhydrophobicity, as even surfaces with a seemingly high droplet mobility can fall short of the requirements for superhydrophobicity. Also noteworthy is the fact that hierarchical roughness is not explicitly required for superhydrophobicity. While this is the easiest path to obtaining superhydrophobicity, it can potentially also be achieved with Cassie-Baxter wetting on surfaces which only have nano-scale roughness, but a very low φ_s value.

Due to the importance of contact angle hysteresis, it is worth the time to take a closer look at how it is measured and gain a full understanding of the physical phenomena it represents. There are two techniques which are commonly used to measure contact angle hysteresis: The droplet inflation/deflation method, and the tilting method [50].

The droplet inflation/deflation method is performed by first placing the droplet dispenser very close to the sample surface. A small amount of water is then dispensed, so that there is a small droplet

sits on the surface while still being in contact with the dispenser itself. A video recording of the droplet is started. The droplet is then inflated by continuously dispensing water (~10 µl total). The droplet will increase in size until eventually the baseline of the droplet expands. The video frame immediately before this baseline expansion is used to determine the advancing contact angle. When all of the water has been dispensed, deflation of the droplet is performed by removing water. The droplet will now decrease in size until the baseline of the droplet contracts. The frame immediately before this change in the baseline will be used to determine the receding contact angle [51]. A schematic of this process can be seen in Figure 2.7.

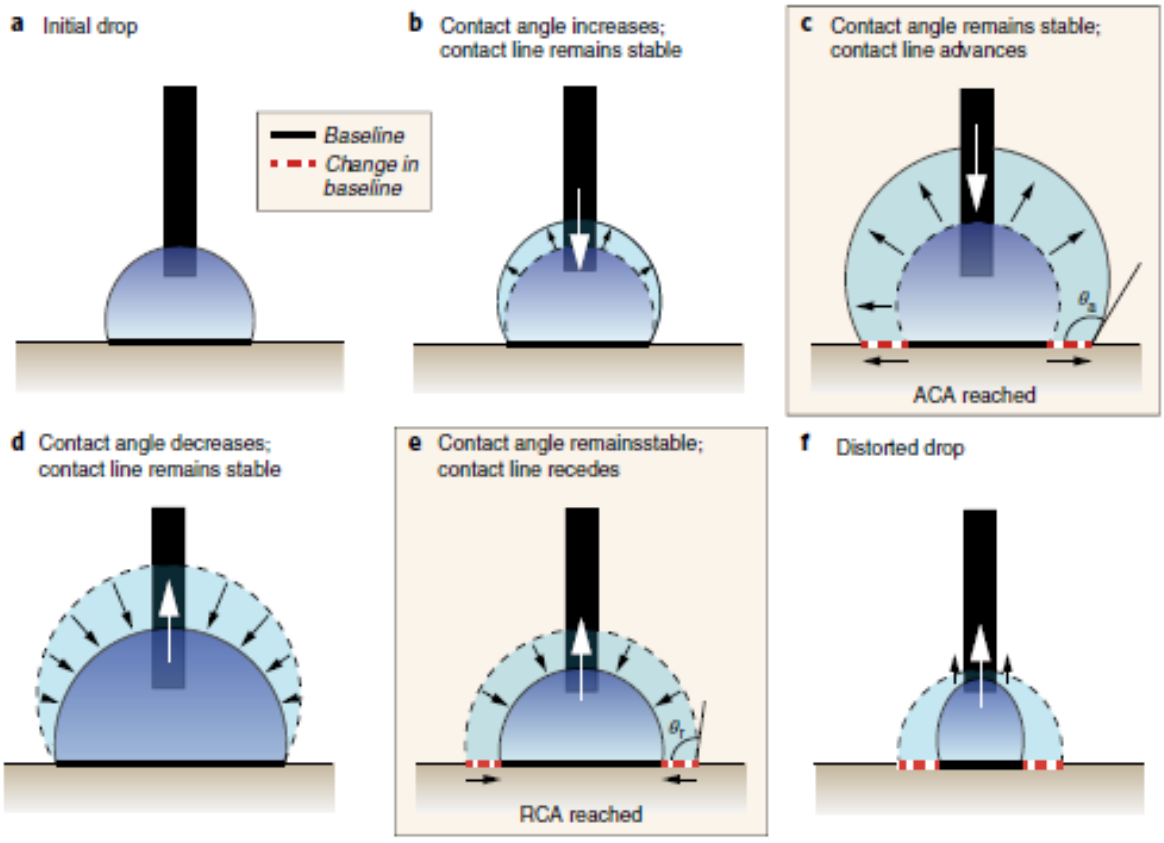

Figure 2.7: Droplet inflation/deflation method for measuring CAH. The initial droplet and beginning of droplet inflation can be seen in a) and b). At some point, the baseline begins to advance, and the advancing CA can be measured during this time. After the droplet is fully inflated, deflation begins as seen in d). The baseline decreases as in e), and the receding contact angle can be measured from the last frame before the baseline change. It is important to note that when the droplet size becomes too small (< 3µl), its shape will be highly distorted from its contact with the needle, and measurements taken at this point are not valid (f). Taken from [39].

The biggest advantage of this method is that it is relatively simple to perform; a bare-minimum setup can be achieved with a microliter syringe and a camera. It also relies only on interactions between water and the surface itself, rather than the effects of gravity as is the case in the tilting method. Disadvantages are that it does not provide a RoA value, and that for high-quality measurements, an automatic dispensing system with a consistent water flow rate is needed [39]. It is also very important to perform a careful analysis after the video has been captured. Especially on a superhydrophobic surface, it can be difficult to pinpoint the frame at which θ_{adv} and θ_{rec} should be calculated, since the baseline may appear to move consistently with droplet inflation and deflation. In this case, multiple measurements must be made across multiple frames if there is no software to analyze the video, which can be quite tedious. The possibility of droplet distortion by the needle must also be considered for any frame to be used for measurement; while Figure 2.7 shows a droplet which is perfectly centered around the dispenser, this is rarely the case in reality. So while the methodology is rather basic, obtaining accurate measurements is not always so simple, and it has been estimated that it takes 20 minutes to obtain one high-quality CAH measurement with this methodology [39].

The tilting method is performed by first placing a water droplet on the sample surface, starting a video recording of the sample surface, and then tilting the sample until the droplet begins to move [50]. The video is examined to find the last frame before the droplet begins to move, and this frame is used to make all measurements. The roll-off-angle is recorded as the angle of the sample which causes the droplet to roll, while the advancing contact angle is the measured from the front of the droplet, and the receding contact angle is measured from the back, as can be seen in Figure 2.8.

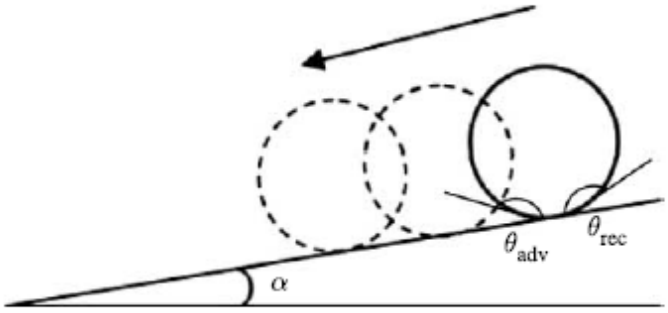

Figure 2.8: Tilting method for contact angle hysteresis measurement. α represents the roll-off angle, and the points of measurement for the advancing (θ_{adv}) and receding (θ_{rec}) contact angles are indicated. Taken from [35].

One advantage of the tilting method is that it allows the capture of the roll-off angle, as well as the advancing and receding contact angles from a single image. It also gives a greater intuitive sense for the superhydrophobicity of a surface by allowing the user to see how little tilt is required to cause a droplet to roll off. While a superhydrophobic surface with Cassie-Baxter wetting will have a roll-off angle below 10°, a surface which exhibits Wenzel wetting can have droplets adhere to the surface even when turned upside down (Figure 2.9). There is a correlation between CAH and RoA values, however, there is no calculation which can give one from the other, and the difference between these will vary from surface to surface. RoA can be particularly important in certain applications, such as in controlling liquid flow in microchannels and for surfaces where self-cleaning properties are desired [50].

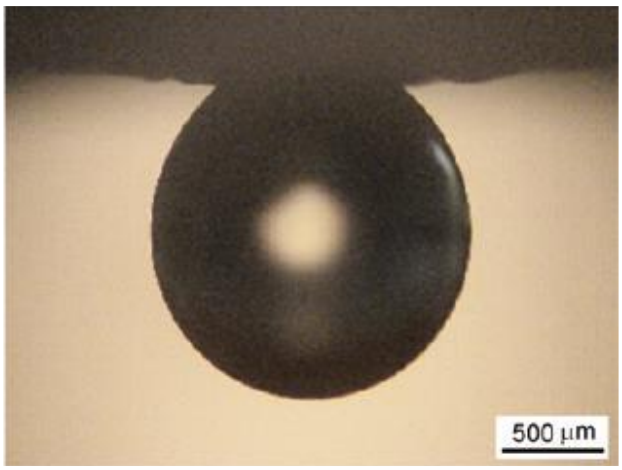

Figure 2.9: A droplet suspended from a surface which exhibits Wenzel-type wetting. The droplet adheres to the surface even when tilted to 180 °. Taken from [33].

One disadvantage of the tilting method is that it is requires more complex equipment to perform. As was the case with droplet flow, an automated system with a consistent tilting rate is required if accurate measurements are to be obtained. Another issue stems from the fact that the droplet rolls because it is being acted on by gravity. This means that the mass of the droplet will be directly related to the downward force it experiences, and because of this it is important to use consistently-sized droplets for all measurements, and to always report the droplet volume used [39].

Like the contact angle itself, contact angle hysteresis is a seemingly simple measurement that nevertheless requires real attention to and thought about the measurements being made. While it has been over 70 years since the concept was first proposed [52] and the theoretical groundwork

was laid [53] one can still find articles set to be published in January of next year which misreport advancing contact angles as being below the corresponding static contact angle [44], and just a few months ago, a Nature protocols article was published with the goal of defining a proper technique for its measurement [39].

2.1.4 Reentrant topography

While the classic model for a superhydrophobic surface is to combine hierarchical roughness with hydrophobicity, it has been shown recently that the effects of superhydrophobicity can be obtained even outside of these parameters. Indeed, the carnauba wax which coats the surface of the lotus leaf was found in 2005 to have a contact angle of 74 ± 9°, making it hydrophilic rather than the supposed hydrophobic [20]. Why then, is the lotus leaf superhydrophobic at all? it is because of what has been termed "reentrant texture" or "reentrant topography" [29]. This means that a vector normal to the surface and placed outside of the interior boundaries of a feature will pass through the feature more than once as it extends outwards. This could also be expressed as a surface whose height is not a function of its (x, y) coordinates due to failing the vertical line test. The first surfaces of this type were created by etching silicon, and can be seen in Figure 2.10

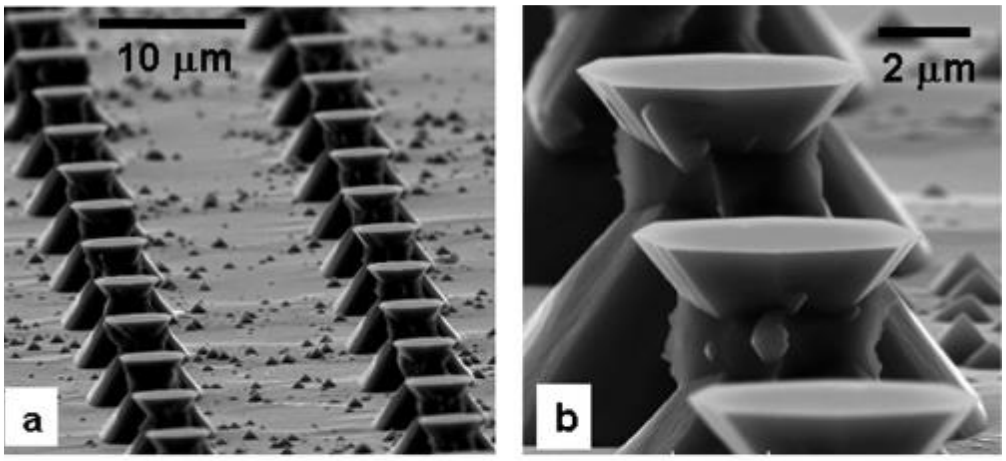

Figure 2.10: SEM images of silicon surfaces etched to give them reentrant topography. This surface had a contact angle of 160° despite the flat hydrogen-terminated Si surface having a contact angle of only 74 ± 3°. Taken from [54].

Superhydrophobicity is not guaranteed simply because a surface has reentrant topography; the droplet behaviour depends on the shape of the structures. In particular, the angle made by the walls of the "indent" and the horizontal plane ($\theta_{overhang}$) is important. This is illustrated in Figure 2.11.

For water to sit on top of the silicon pillars, there must be an energy barrier preventing it from sliding down them and wetting the surface completely. This energy barrier is provided by capillary forces for reentrant surfaces. If $\theta_{overhang}$ is greater than the contact angle of water on the flat surface (θ_{flat}), then a meniscus forms which generates a force F_s downwards into the air pocket, and the surface is wetted completely. In the situation where $\theta_{overhang} = \theta_{flat}$ then there is no meniscus and the water sits parallel to the horizontal plane. It should be noted that this configuration will be extremely unstable and even the effects of gravity could be enough to cause surface wetting. If $\theta_{overhang} < \theta_{flat}$, then the water in the air pocket takes on a convex shape, generating a force away from the surface and maintaining a metastable Cassie-Baxter state.

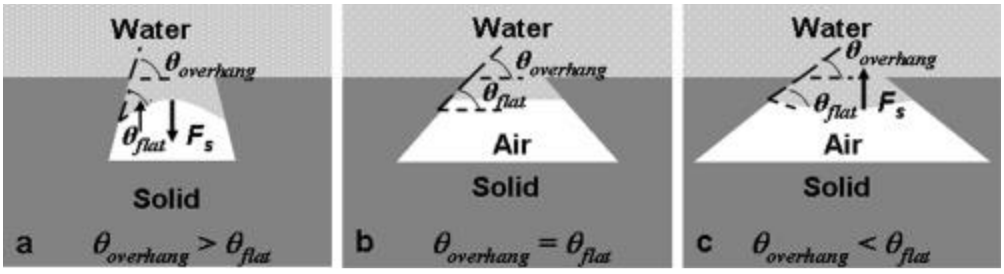

Figure 2.11: Three cases of reentrant topography. Shows the effects of a) $\theta_{overhang} > \theta_{flat}$, b) $\theta_{overhang} = \theta_{flat}$, c) $\theta_{overhang} < \theta_{flat}$. Taken From [54].

While an abundance of available hydrophobic coatings means that reentrant topography is not necessary for the case of superhydrophobic surfaces, it is a very important concept for superoleophobicity, where coatings which are oil-repellant on flat surfaces may not be readily available or even exist [29].

2.1.5 Superhydrophobicity in practice

While the previous sections have aimed to provide an understanding of superhydrophobicity and how it can be measured, this literature review would not be complete without exploring some of the specific surfaces which have been developed by researchers. Ignoring the possibility of reentrant topography on hydrophilic surfaces, there are three main ways in which a superhydrophobic surface can be obtained:

1. Depositing a hydrophobic coating on a surface with the desired roughness. [16][22][44].
2. Depositing hydrophobic nanostructures on a surface with micro-scale roughness [33][37].

3. Modifying a hydrophobic surface so that it exhibits hierarchical roughness [55].

In practice, the first method is seen most often in the literature, as it does not limit the type of material which can be used to obtain the desired surface morphology.

With advancements made to surface patterning over the past 70 years, it is now much easier than in the time of Cassie and Baxter for researchers to design and manufacture surfaces to their liking. An example of this is work done by Nguyen *et al.*, who used plasma etching of quartz glass through nanospheres of varying size to create precise nano-pillar arrangements. These were then coated with a perfluoropolyether solution to render them hydrophobic. The chosen conditions lead to pillars with top diameters of 30 – 145 nm, while all had a 150 nm base.

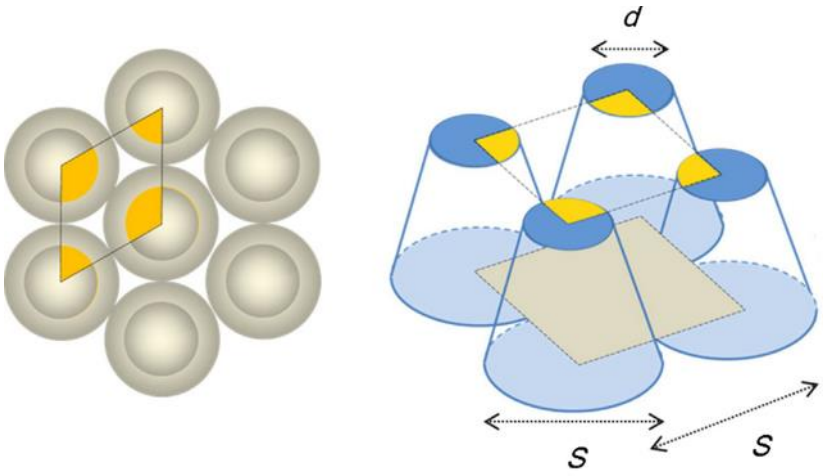

Figure 2.12: Definition of a unit cell for the calculation of the CB fractional area φ_s. S is the center-to-center distance between pillars, d is the diameter of a pillar top. Adapted from [47].

As the nanospheres formed a hexagonal arrangement, so too did the pillars. There could then be divided into unit cells, as seen in Figure 2.12, and from the unit cell the fractional area for the Cassie-Baxter equation (φ_s) of the surface can then be obtained from:

$$\varphi_s = \frac{\pi d^2}{2\sqrt{3}S^2} \tag{2.5}$$

where d is the diameter of the pillar top and S is the center-to-center distance between pillars. Plugging these values into the Cassie-Baxter equation yielded results very close to those obtained by contact angle measurement, as can be seen in Table 2.1.

Table 2.1: Feature sizes and measured contact angle vs. Cassie-Baxter calculated contact angle for nano-pillar surface. Adapted from [47].

Sample	Top diameter (nm)	Areal fraction φ_s	Measured CA (°)	Calculated CA (°)
1	30	0.036	169	169
2	50	0.11	160	161
3	70	0.2	154	153
4	90	0.33	151	148
5	145	0.74	132	127

An additional property of superhydrophobic surfaces is the ability of water to bounce off of them due to its low adhesion. Sharifi *et al.* [56] showed exactly this for a TiO_2 surface deposited by suspension plasma spray and coated with hydrophobic stearic acid, and the bouncing can be seen in Figure 2.13. This surface was tested by measuring the coefficient of restitution (ratio of droplet velocity after impact to the velocity before impact) for bouncing droplets, which was shown to be 0.82 for an impact velocity of 250 mm/s and 0.48 for an impact velocity of 450 mm/s. The values are an improvement over those seen for the lotus leaf, which gave values of 0.75 and 0.40 for the same impact velocities.

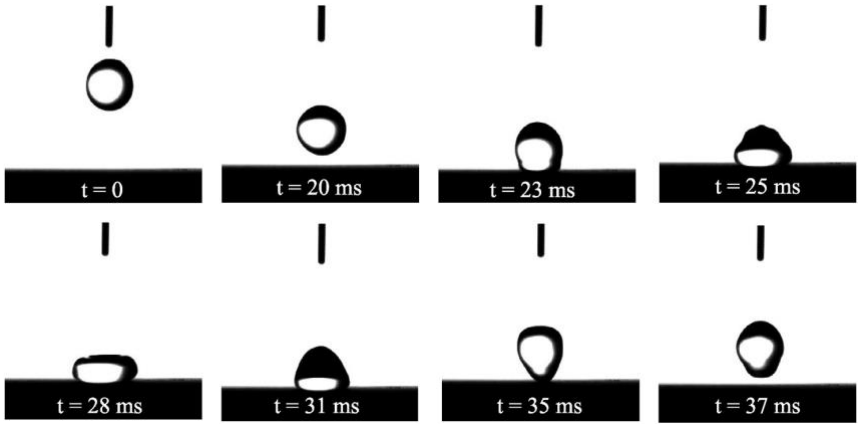

Figure 2.13: Water droplet bouncing on a superhydrophobic surface. Taken from [56].

Further bouncing droplet experiments were performed by Mishchenko *et al.*, this time using highly organized silicon surfaces patterned by photolithography and reactive ion etching steps [16]. Surfaces were then treated with a hydrophobic silane to render them superhydrophobic. The surface structures developed included small densely packed pillars, larger more sparsely placed pillars, and a closed-cell brick structure. All of these can be seen in Figure 2.14.

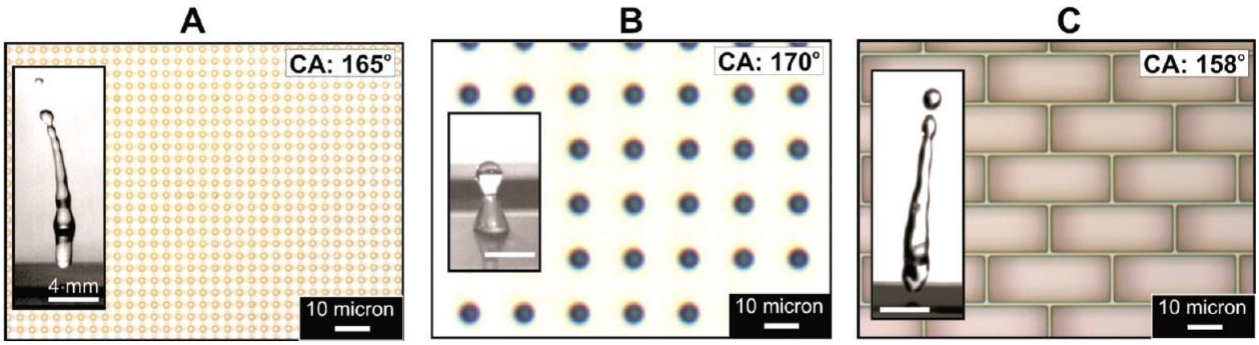

Figure 2.14: Three different surface patterns used to test droplet bouncing. a) small, dense pillars, b) larger, sparse pillars and c) closed-cell bricks. Inlays show contact angle and droplets bouncing off of each surface. Taken from [16].

The droplet-bouncing results in this case were analyzed with the intention of determining temperatures at which the droplet freezes to the surface and will be explored in Section 2.2.2. However, this work also contains a particularly interesting and not often reported analysis of the pressure stability of the developed surfaces. This provides the pressure at which droplets will transition from a Cassie-Baxter state to a Wenzel state. While this is not a great concern for droplets rolling across the surface, it does give interesting data for applications where droplet impacts are expected. It was shown that the closed-cell structure seen in Figure 2.14 (c) rebounded droplets without issue from 10 cm, while droplets falling 5 cm were able to wet the surface of the large-post structure seen in Figure 2.14 (b). The reason given for this is that air becomes trapped in the closed cells upon droplet impact, and its compression pushes back against the droplet allowing it to bounce. In the case of the pillars, the air displaced by the droplet can easily move across the surface, allowing water to contact the surface and establish Wenzel wetting. Further experiments performed in a high-pressure chamber showed no Wenzel wetting on the closed-cell surface even at 40-60 atm, which translates to droplet impact speeds of 90 – 135 m/s.

2.2 Icing & icephobicity

It is well-known that water freezes at 0 °C. In fact, until 1954, the transition temperature of ice to water defined 0 °C [57]. However, if there are a lack a nucleation sites (e.g. dust, impurities, surfaces in contact with the water), then water can be cooled to as low as ~232 K (-41 °C) before homogeneous nucleation occurs, causing the water to freeze spontaneously [58]. When water is below its freezing temperature but ice still has not nucleated, it is said to be supercooled. This is what occurs in clouds which contain supercooled water droplets; there are no nucleation sites so they are allowed to cool with the air, and they have been shown to cool down as low as -35 °C while remaining liquid [11].

It is not only the droplet temperature that affects aircraft icing in clouds. Two other extremely important parameters are the liquid water content (LWC) and the median volume diameter (MVD) [59]. The LWC is measured in g/m^3 and values as low as 0.2 g/m^3 can cause icing. MVD is measured in µm, where droplets above 30 µm are sometimes referred to as supercooled large droplets (SLD). It has been shown that SLD pose the highest risk for icing, while smaller droplets can also cause icing if the LWC is high enough [9]. Table 2.2 lists the conditions which give the greatest risk of in-flight icing.

Table 2.2: Conditions for greatest risk of icing. Taken from [60].

Parameter	Value
Liquid water content	0.2 to 3.0 g/m^3
Temperature	+4°C to -40°C
Droplet diameter (MVD)	Typically 1-50 µm, also up to 400 µm

Given the large range of parameters which can cause icing, it should not be surprising that in-flight icing is not limited to parts of the world with colder climates. This can be easily seen by looking at Figure 2.15, which shows the average supercooled liquid water content of clouds across the globe. It should be stressed that it is supercooled LWC which is being shown, not the total LWC. Comparing Figure 2.15 to the global population map in Figure 2.16, it is seen that many of the

world's most populous areas are in or near locations with an average supercooled liquid water content above 0.2 g/m^3. This means that icing can be a concern on almost any flight.

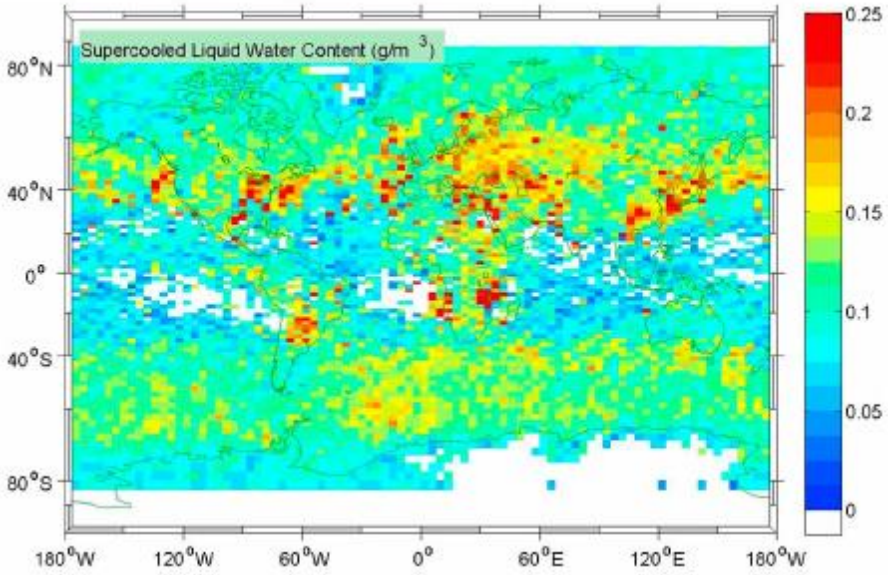

Figure 2.15: Average supercooled liquid water content in clouds across the globe. Taken from [61].

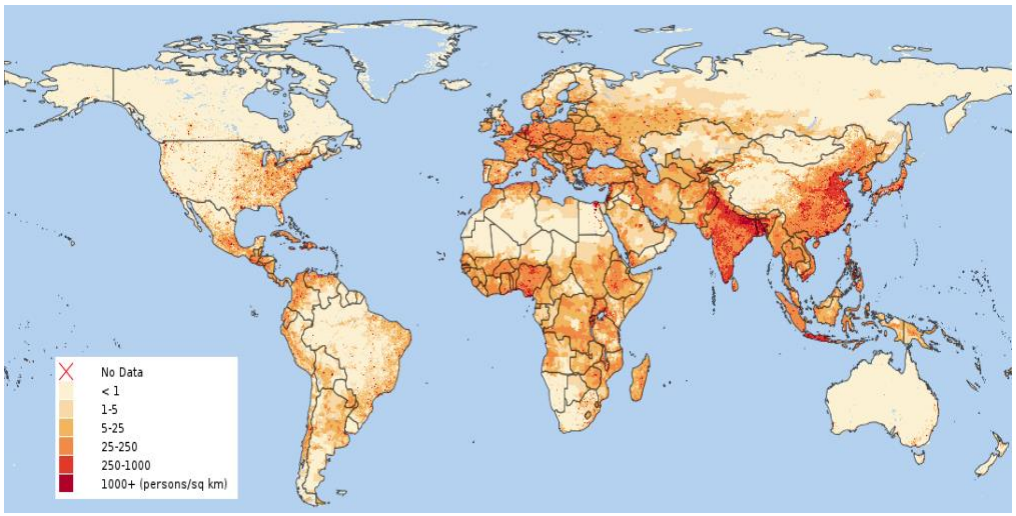

Figure 2.16: Persons/km^2 on Earth in 2015, as modelled by Gridded Population of the World (GPW) v4. Taken from [62].

The ice which forms form SWD can be divided into three types: rime, glaze, and mixed [63]. Examples of each of these on steel plates and aerodynamic profiles can be seen in Figure 2.17. Rime ice is formed when supercooled droplets freeze immediately upon impact, and is easily identified by its milky opaque appearance [60]. Glaze ice is formed when supercooled droplets run back along a surface before freezing. It is denser and harder than rime ice, and is transparent or translucent [7]. Mixed ice is, unsurprisingly, a mix between rime and glaze ice.

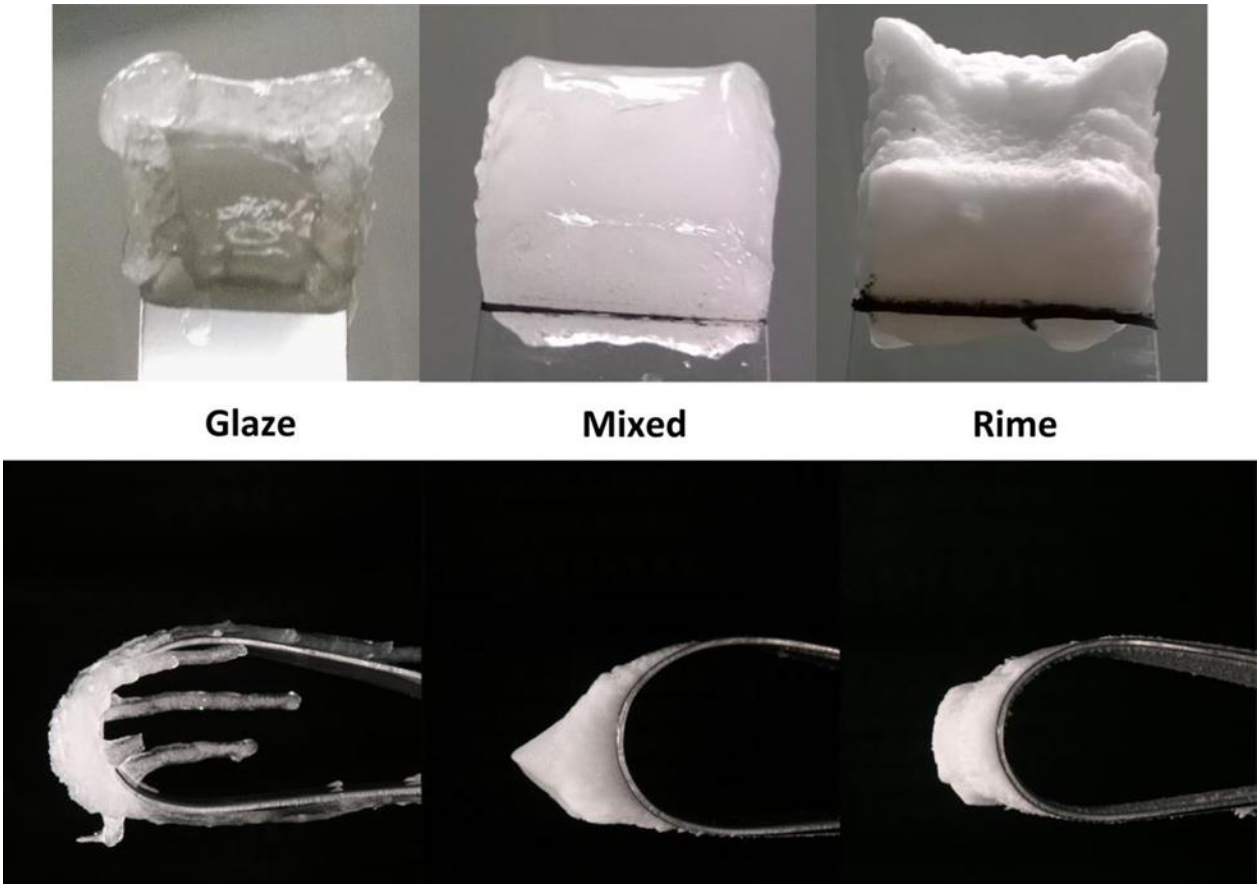

Figure 2.17: Glaze, mixed, and rime ice formed on steel plates (top) and aerodynamic profiles (bottom). Taken from [63].

As was mentioned in the introduction, the issue of icing has been around for a long time, indeed, long before the current verbiage associated with it. The first usage of the term icephobic, then stylized as "ice-phobic" (quotes included), comes from a 1962 work concerning impinging droplets on Teflon surfaces [64]. Around 2004, there was seen a large increase in the research output on icephobicity, which by this time had outgrown both its hyphen and quotation marks [65]. In creating measurable parameters for icephobicity, it makes sense to take cues from the nomenclature

of hydrophobicity. Just as a hydrophobic surface is not one which is completely unwettable, the formation of ice on a surface should not disqualify it from being labelled "icephobic". Instead, we should look at ease of ice removal, and the difficulty of ice formation to decide whether a surface is icephobic. This section will do exactly that, exploring the most common measures of icephobicity: ice adhesion, ice accretion, and freezing delay. A wide variety of sample types which exhibit some level of icephobicity will be presented, and the challenges involved in making durable icephobic surfaces will be explored.

2.2.1 Ice adhesion

The most common definition of icephobicity is related to ice adhesion. In this case, researchers aim to measure the shear stress required to remove ice from a sample, and report this as the "ice adhesion strength". When examining the results, it is said that any surface exhibiting an ice adhesion strength less than 100 kPa may be labelled as "icephobic". This guideline was presented as early as 1993 as a benchmark for anti-icing paved surfaces [66], and was reiterated by Hejazi *et al.* in a 2013 review on the subject [65]. This number has since become a standard value used in the literature [18][67]. Beyond this, the value of 20 kPa is used as a benchmark for surfaces to allow the passive removal of ice, such as by wind or vibration [19].

There are two main techniques used for the formation of ice and testing its adhesion. The first begins with the formation of ice on a surface by spraying it with microdroplets of supercooled water in an icing wind tunnel. The mass and area of ice formed are then recorded, and the sample is mounted onto a centrifuge in a cold chamber, and spun at a constantly increasing speed until the ice detaches from the surface [68][44][23]. The speed at which the ice was removed is recorded, and from this, the centrifugal force can be calculated as:

$$F = mr\omega^2 \tag{2.6}$$

where m is the mass of ice which has been removed, r is the radius of the centrifuge beam, and ω is the rotational speed in rad/s. From this, the shear stress can be calculated simply by taking

$$\tau = \frac{F}{A} \tag{2.7}$$

where *A* is the deiced area. The advantages of this technique are that it allows for testing any type of ice which can be obtained in the icing wind tunnel being used, and that the freezing mechanism is the same as we expect to see in aviation. The downside, of course, is that it requires an icing wind tunnel, which is not a readily available piece of equipment.

The second technique involves freezing ice blocks onto the surface, and then applying a force on the ice, parallel to the surface being tested [19][69][70]. An example of this process can be seen in Figure 2.18. Water is poured into a mold, which is then placed onto the surface, using any variety of methods to keep the water from leaking out. The ice is formed by placing the sample + mold configuration into a freezer or onto a Peltier plate for 10-24 hours until solid blocks of ice are formed. The molds are then removed, and a force transducer is used to apply pressure until the ice is removed. Force is applied as close to the bottom of the ice block as possible (~1 – 2 mm) to minimize torque on the sample. The maximum force required to remove the ice is recorded and from this the ice adhesion strength can be obtained by dividing by the area of ice/sample contact. This technique is relatively simple to set up with common laboratory equipment, but it ignores both the structural differences of different ice types, and the complications which can arise from micro-scale droplets becoming trapped in surface features.

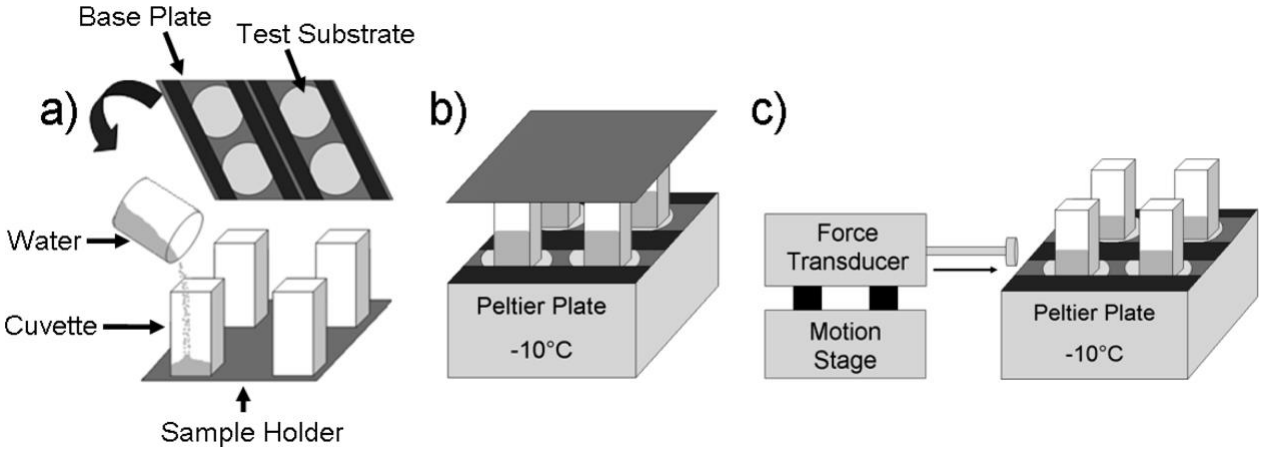

Figure 2.18: A common method for testing the adhesion strength of a surface. a) Water is poured into molds which are then placed in direct contact with the samples. b) Water is frozen onto the surface, whether via Peltier plate or simply by placing samples in a freezer. (c) The molds are removed, and a force transducer is used to apply a force until the ice breaks or is dislodged. This force is noted, and from this an ice adhesion strength value is obtained. Taken from [70].

Results of ice adhesion tests for a wide variety of surfaces were aggregated by Kreder *et al.* [18] and can be seen in Figure 2.19. Here the results are divided into material categories, and they allow us to get a sense of expected values for different surfaces. These results and the types of surfaces used to achieve them will be explored in more detail in the following pages.

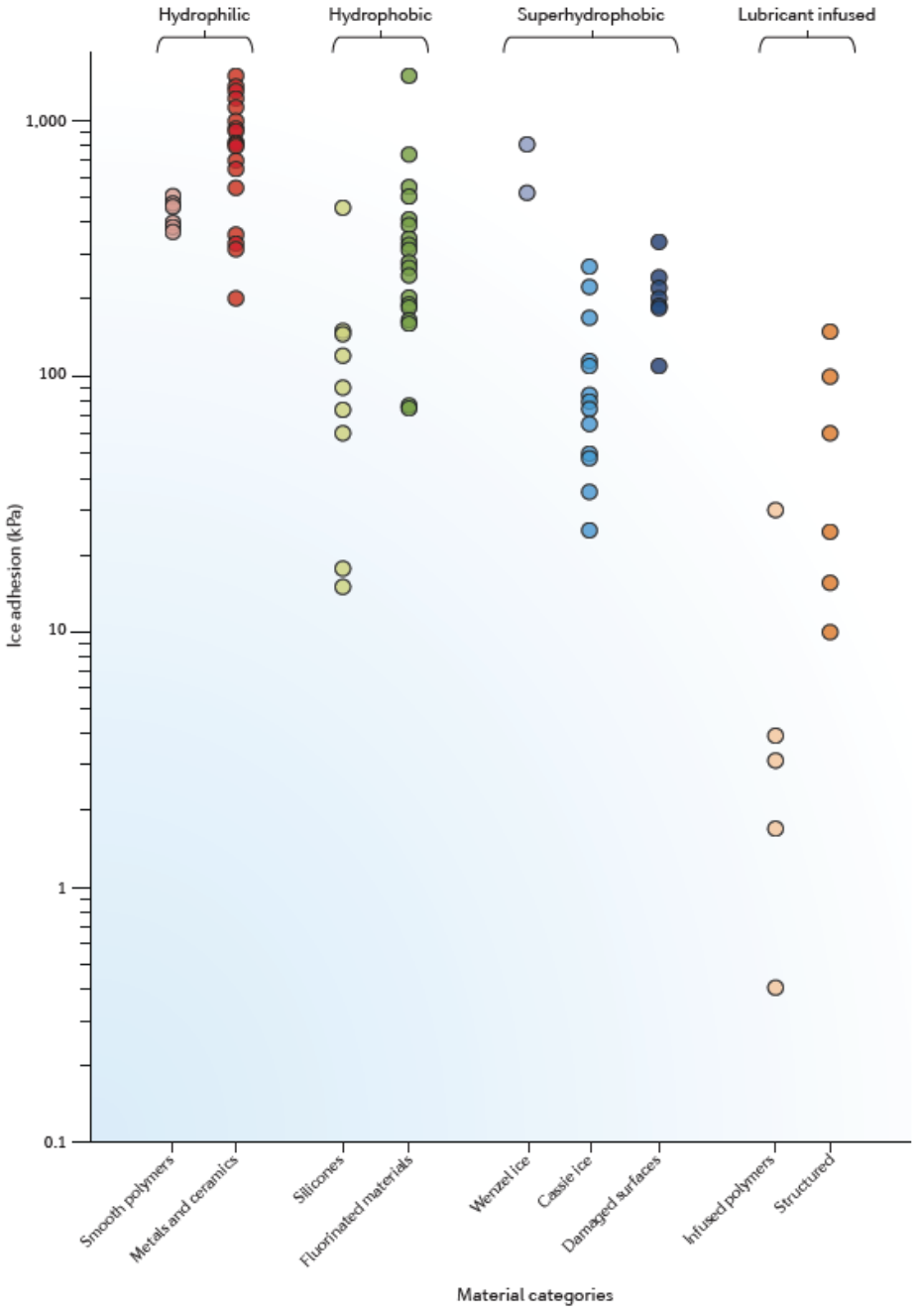

Figure 2.19: A breakdown of ice adhesion values reported in the literature for different types of surfaces. Adapted from [18].

Looking at Figure 2.19, we first see the high ice adhesion for hydrophilic materials such as smooth polymers, and the particularly high ice adhesion for ceramics and metals, which in many cases exceeds 1000 kPa. This high adhesion of ice to metals is the main reason that icephobic coatings are so desirable.

Looking at hydrophobic flat surfaces, we see silicones and fluorinated materials. Fluorinated coatings seem to have the effect of shifting ice adhesion values downward from those seen for metals and ceramics, with the majority of values in the range of 200-400 kPa. There have, however, been some fluorinated smooth sol-gel coatings which have shown ice adhesion values below 100 kPa [71]. More promising results are seen for silicones. A commonly-seen silicone in the literature is PDMS (polydimethylsiloxane) [19] [72]. While the typical reported ice adhesion values for PDMS are in the 200-300 kPa range, Golovin *et al.* [19] showed that this value could be decreased if a coating's physical stiffness was altered through a change in its cross-link density. In this case, ice on the surface is shed through interfacial cavitation: a force applied to the ice causes deformation of the soft elastomer coating, and because the ice is so comparably stiff, it cannot deform with the PDMS coating. The stress from the applied force causes cracks along the ice-solid interface which then cause delamination of ice from the surface. Through the optimization of the PDMS stiffness, they were able to produce coatings with ice adhesion as low as 26 ± 3 kPa.

PDMS coatings have been pushed even further through the development of coatings with internal voids, which function as macroscale crack initiators (MACI) [69]. Figure 2.20 shows a finite element modeling comparison of MACI coatings to flat homogeneous PDMS coatings. By optimizing hole size across a three-layer structure, He *et al.* were able to reduce the ice adhesion to 28 kPa for non-chemically-modified PDMS. By using silanized PDMS for lower surface energy, this was decreased to 25 kPa, and by modifying the cross-link density this was further decreased to only 5.7 kPa [69]. It should be noted that in the case of ice removal by interfacial cavitation, there is no requirement for the surface to be hydrophobic, let alone superhydrophobic.

The downside of this methodology for icephobic surfaces is the lack of mechanical stiffness of PDMS. This prevents the its usage in fields such as aerospace where high-velocity particles impinging on the surface could easily pierce it or become embedded [18]. And while this is a concern for "regular" PDMS, the effect would be exaggerated for coatings rendered even less stiff by the methods described above.

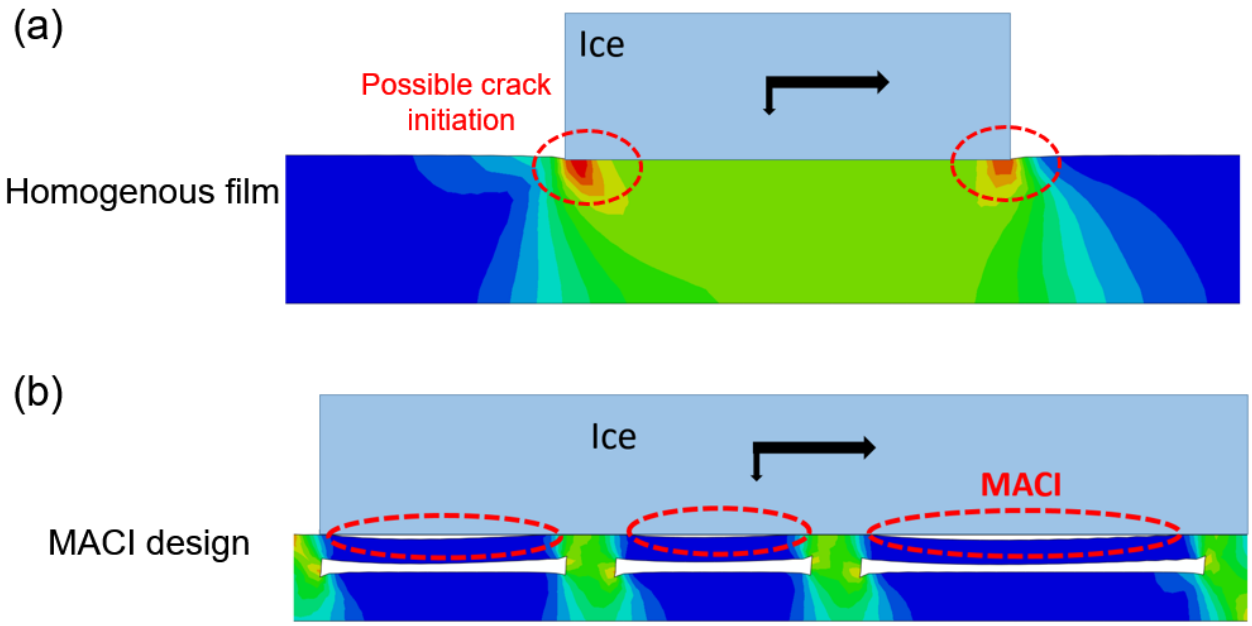

Figure 2.20: Finite element strain analysis for ice on PDMS films. The locations of possible crack initiation for a homogenous film are shown in a), while b) shows that MACI causes macroscopic cracks at multiple locations along the interface. The black arrows are representative of the forces applied. Taken from [69].

Next in Figure 2.19, we see superhydrophobic surfaces, presenting many surfaces at or below the 100 kPa threshold. Wenzel surfaces are included as a reference point, and we can see that these always exhibit high ice adhesion. The reason for this is the same as their high water adhesion: water becomes anchored into the surface features, and upon freezing, it is now locked into place. For this reason, it is extremely important that researchers claiming to include SHS in their testing include a CAH value, an RoA value, or at least some indication that the droplets are in a Cassie-Baxter and not a Wenzel state on the surface. This is not always the case [71].

There have been two reasons given for the decreased ice adhesion of superhydrophobic surfaces: the reduced ice-surface contact area due to the air pockets cause by Cassie-Baxter wetting [23], and the air pockets functioning as surface defects of the ice, promoting the propagation of microcracks [24]. Nguyen *et al.* [47] showed the dependence of ice adhesion strength on contact area using the same hydrophobic nanopillars discussed in section 2.1.5. Surfaces are shown to be icephobic or near-icephobic when the areal fraction is 0.33 or below, for pillars with 30 – 90 nm

top diameters. When the areal fraction increases to 0.74 for the 145 nm pillars, a large increase up to 900 kPa is seen. These values as well as SEM images of the nanopillars can be found in Figure 2.21. A value of ~7 kPa was obtained for the 30 nm pillars with a 0.036 areal fraction.

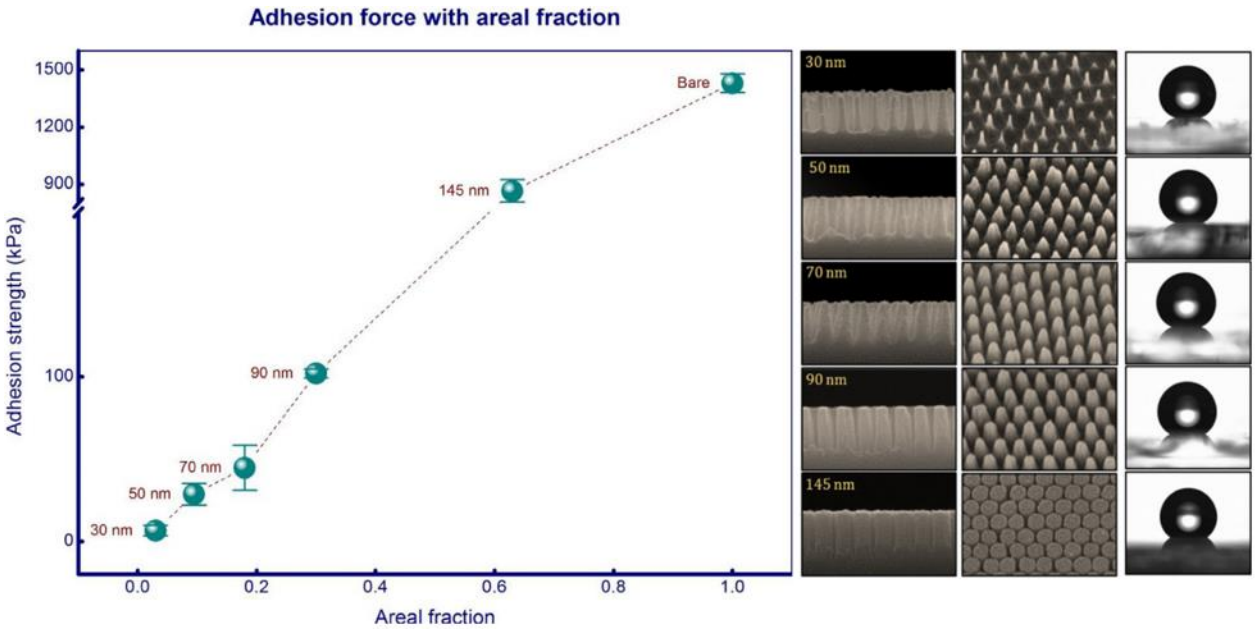

Figure 2.21: Ice adhesion vs. Areal fraction for hydrophobic nano-pillars. Also shown are SEM cross-sections and tilted images, as well as droplet images for each pillar size. Adapted from [47].

For structures which are not so tightly controlled, such as those on thermal sprayed or anodized surfaces, finding the exact areal fraction can be difficult or even impossible. In 2009 Kulinich and Frazaneh [23] suggested that ice adhesion could be linked to contact angle hysteresis for superhydrophobic surfaces. They tested superhydrophobic surfaces deposited from a ZrO_2 nanopowder suspension in deionized water, which were further coated with a perfluoroalkyl methacrylic copolymer. Surfaces with different morphologies and wettabilities were created by varying the quantity of nanopowder in the suspensions. Icing tests were then performed in an icing wind tunnel and adhesion was calculated via the centrifuge method. Figure 2.22 shows the ice adhesion results for various samples with respect to contact angle and contact angle hysteresis. It is immediately apparent that there is no relation between the static CA and ice adhesion, however, there is a clear reduction in ice adhesion as the CAH value diminishes.

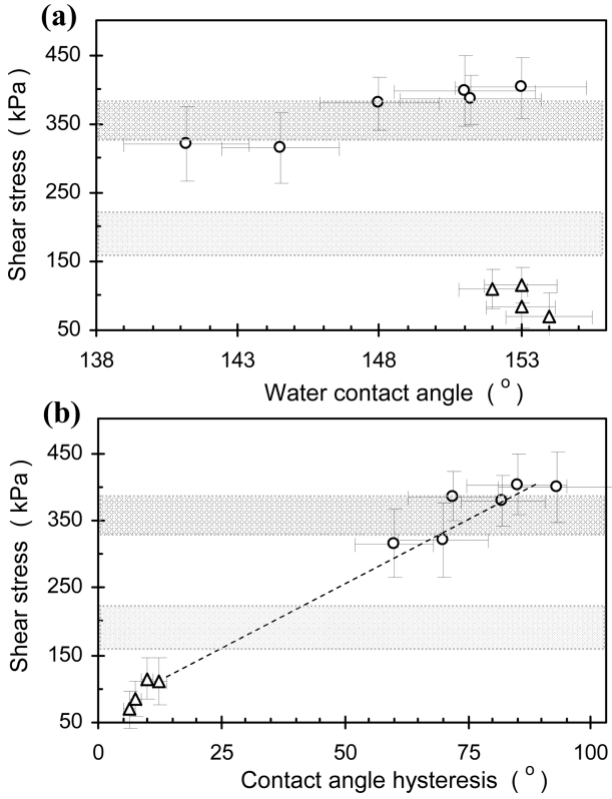

Figure 2.22: Ice adhesion for hydrophobic and superhydrophobic samples. Circles show samples which were spray-coated, whereas triangles are spin-coated samples. a) Shows that there is no correlation between CA and sheer stress, while b) shows a clear correlation between CAH and shear stress. Taken From [23].

This work was expanded upon by Meuler *et al.*[70], who defined a "practical work of adhesion" based on the receding contact angle:

$$W_p = \gamma_{lv}(1 + \cos\theta_{rec}) \tag{2.8}$$

where γ_{lv} is the specific energy of the liquid-vapor interface. Since the equation aims to quantify the behaviour of ice, γ_{lv} will be a constant, and the equation is controlled solely by θ_{rec}. Meuler *et al.* plotted their own results as well as many others seen in the literature, and good agreement with this practical work value was found. This data can be seen in Figure 2.23, and results appear to be consistent across the samples developed by all researchers.

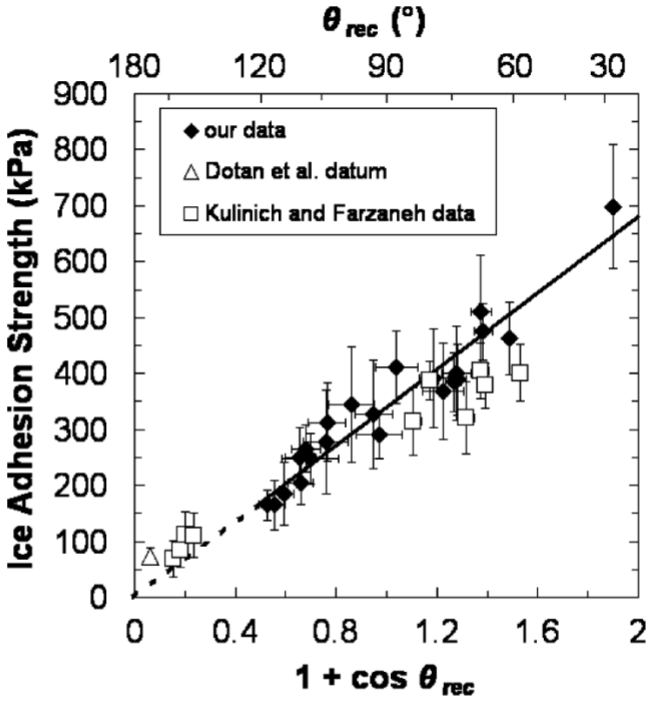

Figure 2.23: Values for ice adhesion strength as a function of θ_{rec} for 33 different samples across three labs, where "our data" is the data measured by Meuler *et al.*, $R^2 = 0.92$. Taken from [70].

This result should be considered when evaluating superhydrophobic surfaces for potential ice adhesion. If we take the theoretical example of two samples presented in Table 2.3, we can see that Sample 1 has a higher hysteresis, but also a higher receding contact angle than Sample 2. It is possible that the hysteresis value of samples 1 is actually being heightened by its superior water repellency (as this gives a higher θ_{adv}), and Sample 1 would indeed be the superior surface in terms of ice adhesion testing. This would be ignored if we account only for the CAH value.

Table 2.3: Two theoretical superhydrophobic surfaces, showing the potential mis-alignment of CAH and θ_{rec}.

Sample	Contact Angle (°)	θ_{adv} (°)	θ_{rec} (°)	Hysteresis (°)
1	165	170	155	15
2	152	155	147	8

With this said, it is not in fact true that any surface which is superhydrophobic will also be icephobic. This is clearly visible in Figure 2.19, where many superhydrophobic samples show an ice adhesion higher than 100 kPa, even while exhibiting Cassie-Baxter wetting (middle column of the superhydrophobic group). Nosonovsky and Hejazi [24] gave a reason for this, stating that the removal of ice from a Cassie-Baxter surface depended not only on the receding contact angle, but also on the sizes of the voids at the ice-surface interface. They derived a relation between the critical shear stress required for mode II ice fracture which is given by:

$$\tau_{yy} = \sqrt{\frac{E\gamma_{IA}(1 + cos\theta_{rec})}{\pi a}} \tag{2.9}$$

where E is the Young's modulus of ice, γ_{IA} is the ice-air interfacial energy, θ_{rec} is the receding contact angle, and a is the crack length, which in this case is the ice-air portion of the composite interface. This means that the air pockets provided by the Cassie-Baxter wetting can themselves be taken as micro-cracks in the ice, and their size will be directly related to the shear stress required for ice removal. Thus, even a surface with a high receding contact angle can have a high ice adhesion strength if the micro-cracks at the surface are too small. For this reason, it is not enough to develop a superhydrophobic coating and to claim that it will now be icephobic, ice adhesion tests must be performed as well.

The last group of materials seen in Figure 2.19 are "Lubricant Infused". While these are highly interesting surfaces capable of giving very low ice adhesion, they will not be discussed in detail here. This is both to limit the length of what is already a quite long literature review, and because these coatings depend on a free-oil layer at the surface which, in the context of aerospace, can be very easily removed [19]. If the reader has an interest in these types of coatings, they are encouraged to read Wilson *et al.*'s 2013 paper "Inhibition of ice nucleation by slippery liquid-infused porous surfaces (SLIPS)" [73], as well as Irajizad *et al.*'s "Magnetic slippery extremely icephobic surfaces" [25].

2.2.2 Ice accretion

Ice accretion tests, whether by measuring a quantity of ice formed or by showing that ice is incapable of forming, are the second way in which icephobicity can be demonstrated. The

fundamental concept is borrowed directly from the superhydrophobicity phenomenon of bouncing droplets, with the hope being that surfaces are repellant enough to have droplets bounce off before they freeze, even in sub-zero conditions. This type of test has been mainly used in the case of superhydrophobic surfaces. In fact, it has been shown that for flat surfaces, there is no link between surface wettability and ice accretion at temperatures below -2 °C [74].

Mishchenko *et al.*[16] captured high-speed images of 15 µl droplets dropped from a height of 10 cm onto sub-zero surfaces with varying wettability (Figure 2.24). When droplets impacted hydrophilic surfaces, they would immediately spread to a maximum radius and remain there until freezing. Droplets impacting hydrophobic surfaces would spread to a maximum radius, retract to a

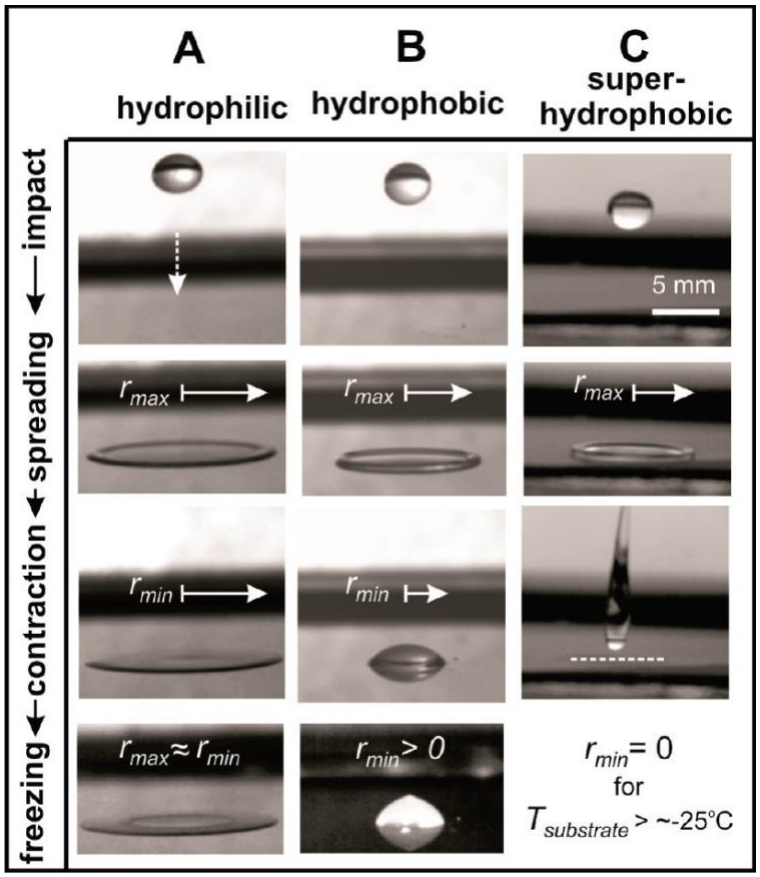

Figure 2.24: High-speed images of droplet impact at freezing temperatures for a) hydrophilic, b) hydrophobic, and c) superhydrophobic surfaces. Taken from [16].

minimum radius, and then freeze in place. For each of these, droplets froze in a matter of seconds for substrate temperatures below -10 °C. In the case of superhydrophobic surfaces, droplets would

impact, spread to a maximum radius, and then bounce off before freezing. Droplet bouncing was seen for temperatures down to -25 °C, at which point droplets froze on the SHS as well.

Testing the same principle, Sarshar *et al.* [75] tested a number of superhydrophobic and near-superhydrophobic surfaces in an icing wind tunnel, exposing them to SWD. Tests were performed at a temperature of -7 °C, an airspeed of 12 m/s, and with a MVD of 60 µm. Results for each surface can be seen in Figure 2.25, where a clear increase in the time required to form a uniform layer of ice is seen with decreases in CAH. Also pictured is their most performant sample along with a bare substrate after 90 seconds of icing. The bare substrate is completely covered with rime ice, whereas the SHS shows minimal icing except around the edges. As icing in aerospace is due to flying through clouds of SWD, it is possible that a SHS could completely prevent a uniform layer of ice from forming if the time spent in the icing cloud is minimized.

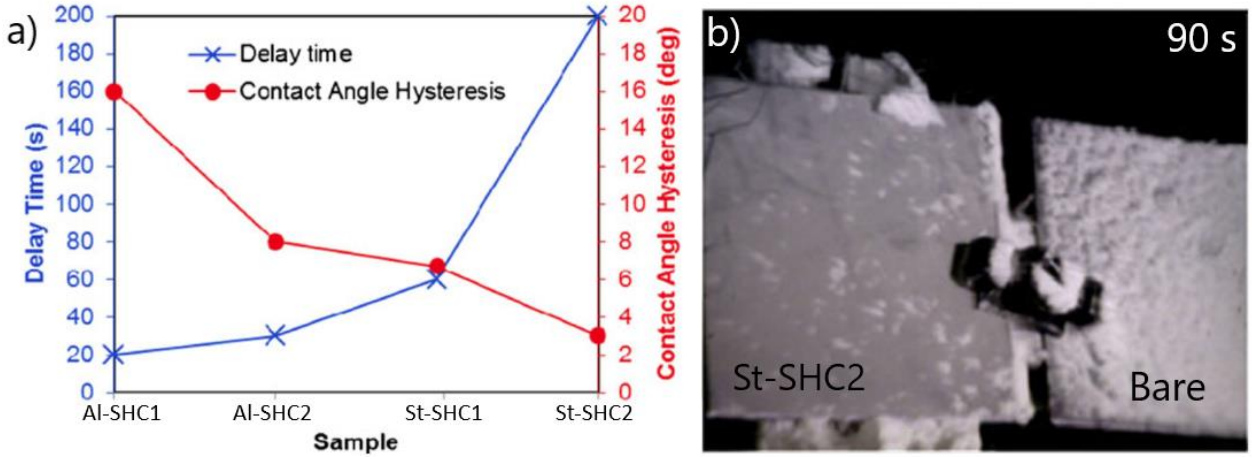

Figure 2.25: a) Time required for four superhydrophobic or near-superhydrophobic surfaces to form a uniform layer of ice. B) Sample St-SHC after 90 seconds of icing, compared to uncoated sample. Adapted from [75].

2.2.3 Freezing delay

A third method of measuring icephobicity is by measuring the time required for a droplet placed on the surface to freeze in sub-zero conditions [47][76]. This is related to ice accretion tests and is the easiest type of test to perform, as all it requires is a cold chamber and a camera (or simply a stopwatch if the researcher is patient). The goal of this test is to see whether or not a surface is able to delay nucleation of ice and while it is interesting, there are two main problems with trying to relate it to application. The first is that in the case of aerospace, supercooled water droplets will

freeze near instantly. So even if a coating is able to delay the time required to form ice from 20 seconds on a bare substrate to 15 minutes on a coated surface, these values are not similar to the timescales which are important in this case. The second issue is that these tests assume laboratory conditions, and assume that the surface will be responsible for initiating heterogeneous nucleation. In application environments, any number of external factors such as dust in the air or a slight contamination of the surface could begin ice nucleation, and thus these tests are not always a good indicator of real-world performance [18].

Regardless, it is interesting to see how results align with other icephobicity tests. Nguyen *et al.*[47], whose nanopillars have been discussed in previous sections, performed freezing delay tests for 5 µl droplets on -20 °C surfaces. The results of these can be seen in Figure 2.26. It is apparent that freezing time increases as the areal fraction decreases, with a near-linear increase from the bare substrate to the 50 nm pillars, and a large increase for the smallest 30 nm pillar.

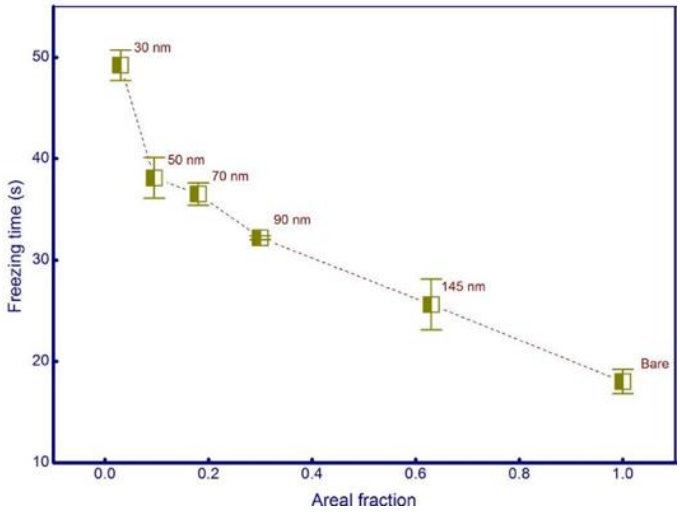

Figure 2.26: Time required for a 5 µl droplet to freeze on nanopillars at -20 °C. Adapted from [47].

A wider range of samples were tested by Guo *et al.*[76] in a similar manner. Figure 2.27 shows the time to freeze for surfaces with hierarchical micro/nano surface features, nano-only features, micro-only features, and a smooth surface. All were coated with heptadecafluorodecyltripropoxysilane (FAS-17) to render them hydrophobic. Droplet size is 7 µl, tests were performed at -10 °C, and light shining through the droplets allows easy identification of when ice has nucleated. The time-to-freeze for the hierarchical surface is shown to be 4 times larger than that of the smooth surfaces. It may seem surprising that the micro-only surface freezes before the smooth surface, however, this

is because the micro-only surface puts the droplet in a Wenzel state, and thus the contact area is even greater than for the flat surface.

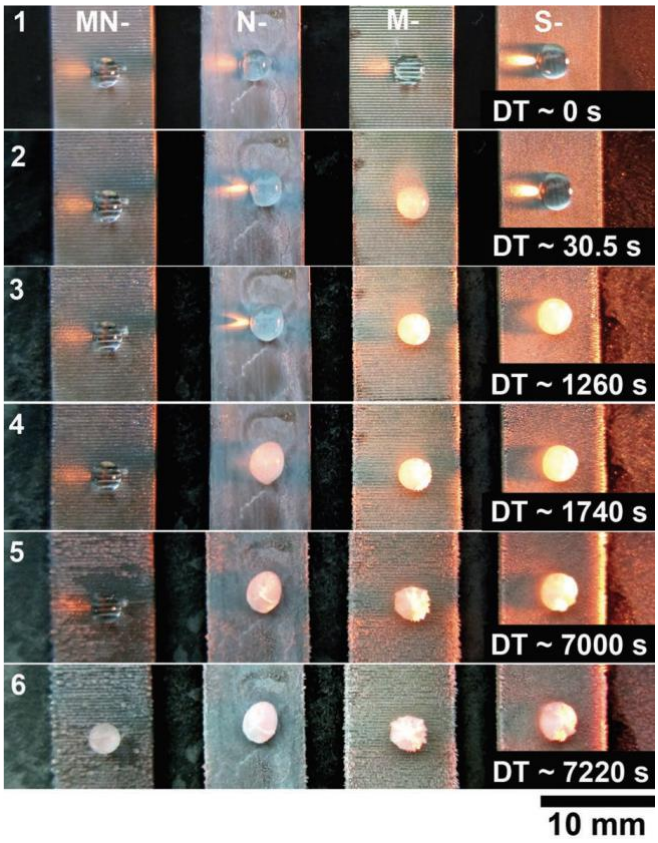

Figure 2.27: Time to freeze a 7 µl water droplet on a -10 °C surface with micro- and nano-scale features (MN-), a surface with only nano-scale features (N-), only micro-scale features (M-), and a smooth surface (S). Taken from [76].

2.2.4 Durability of icephobic surfaces

While superhydrophobic surfaces show promising results in every type of icephobicity test, their biggest barrier to usage is their durability. Their dependence on maintaining a nano-scale roughness, as well as the common reliance on a soft hydrophobic topcoat means that they can be damaged easily. For this reason, results for damaged SHS surfaces are also shown in Figure 2.19, which show a marked increase in ice adhesion.

The durability of icephobic surfaces is often tested by repeated icing/deicing cycles, where deicing consists either of the removal of ice through ice adhesion tests [77], or melting [78]. Degradation is reported either in terms of an increase of ice adhesion with progressive cycling [19], a decrease in wettability performance (that is, decrease in contact angle and increase in contact angle hysteresis) [77], or both [79].

An example of degradation measured by an increase in ice adhesion can be seen in Figure 2.28. Mobarakeh *et al.* [80] created a superhydrophobic surface by depositing plasma-polymerized hexamethyldisiloxane (HMDSO) on anodized aluminium. Ice was formed on the surface in an icing wind tunnel and removed by the centrifuge ice adhesion measurement technique. The increases in ice adhesion are clear over 15 cycles but remain lower than that of untreated aluminium. SEM images in Figure 2.29 show the surface before and after cycling, and the change in morphology is clear. X-ray photoelectron spectroscopy (XPS) analysis measurements taken before and after cycling did not show any meaningful change in the surface chemistry.

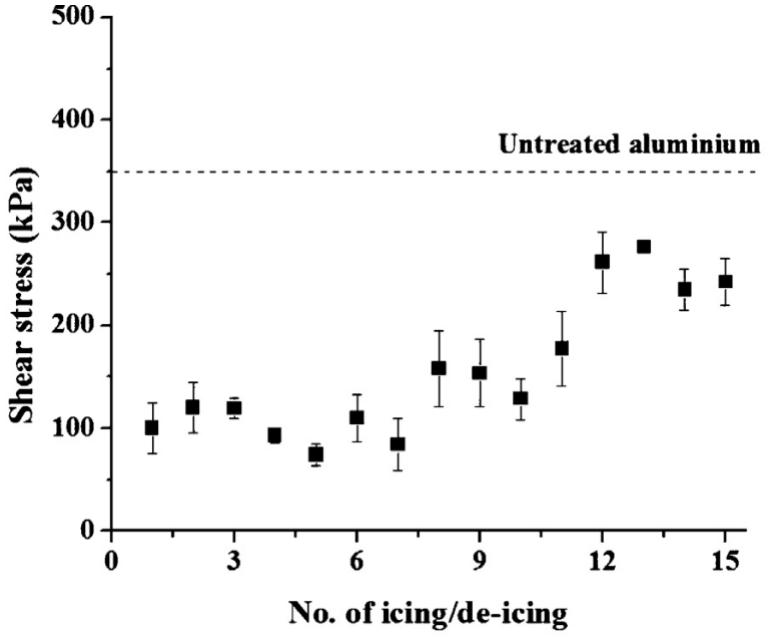

Figure 2.28: Ice adhesion on anodized aluminium with HMDSO coating, over 15 icing/deicing cycles. Taken from [80].

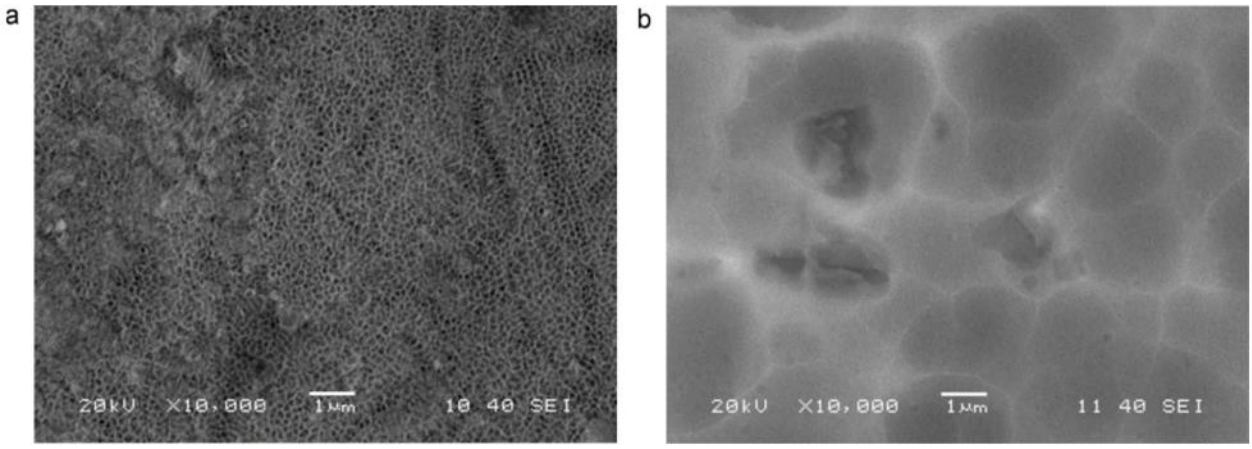

Figure 2.29: Anodized aluminium with HMDSO coating a) before and b) after 15 icing/deicing cycles. Taken from [80].

A similar set of experiments was performed by Wang *et al.* [78], this time with chemically etched aluminium rendered superhydrophobic by deposition of polyfluorodecyltriethoxysilane (PTES). Ice was formed on the surface via water in molds, and ice adhesion measurements were taken with a force transducer. In this case, degradation was tested for both deicing by ice removal and deicing by melting. It was shown that the ice removal method was much more damaging to the surface than melting, with ice adhesion increasing from 220 kPa on the first test to 340 kPa after 20 ice removal cycles, compared to a final adhesion strength of only 272 kPa after 40 ice melting cycles. These results can be seen in Figure 2.30.

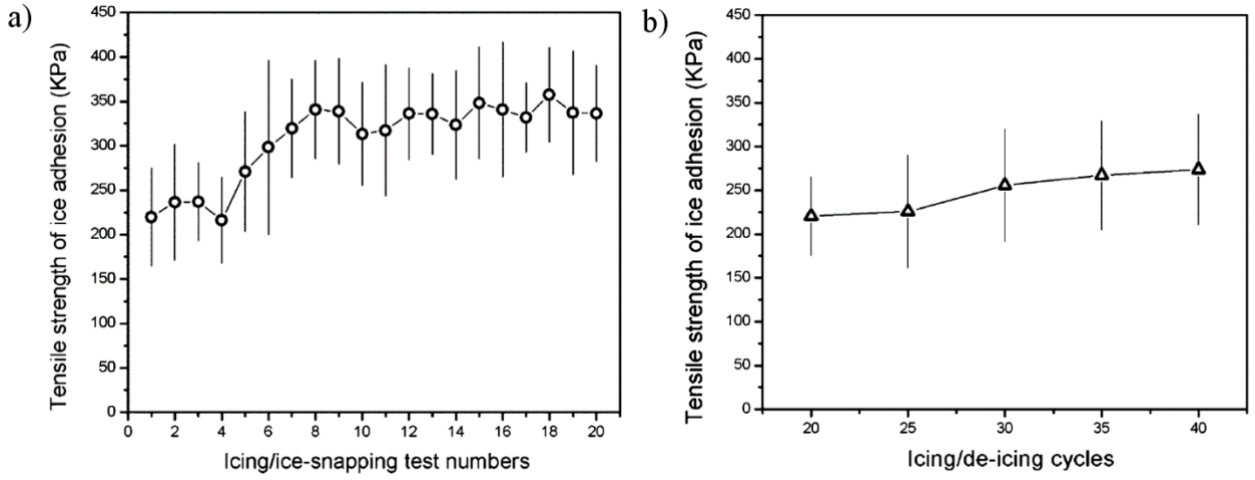

Figure 2.30: Comparison of changes in ice adhesion over a) 20 cycles deicing by forced ice removal b) 40 cycles deicing by melting. Adapted from [78].

Also measured in this case was the effect of cycling on wettability and surface roughness properties, which can be seen in Table 2.4. The surface is clearly superhydrophobic before cycling, with a CA above 160 ° and RoA below 1 °. After cycling, whether by forced ice removal or by melting, contact angles are still above 150 °. Roll-off angles, however, have increased dramatically. Also notable is a decrease in both average surface feature height, *h*, and average roughness R_a. This indicates a smoothing of the surface resulting from the icing/deicing cycles, the mechanism for which is schematically shown in Figure 2.31

Table 2.4: Changes to CA, sliding angle, average height (*h*), average roughness (R_a) before and after multiple icing/deicing cycles. Adapted from [78].

Sample	Contact Angle (°)	Roll-off Angle (°)	h (µm)	R_a (µm)
0 cycles	164.4 ± 0.9	0.84 ± 0.19	4.575	1.250
20 cycles forced removal	150.6 ± 0.3	51.4 ± 3.9	4.046	0.986
40 cycles ice-melting	154.1 ± 0.4	44.3 ± 3.2	3.479	0.727

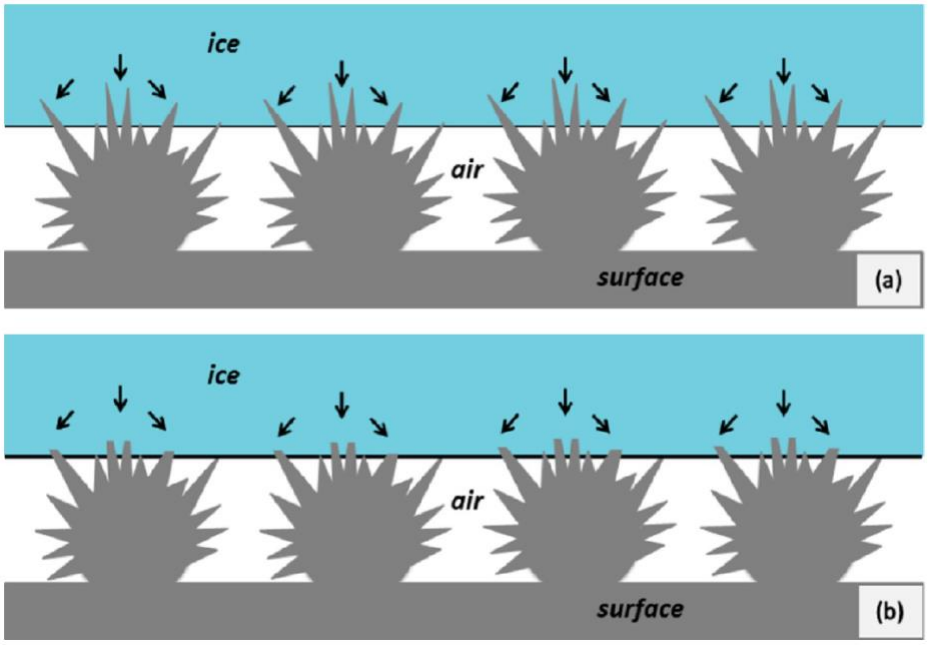

Figure 2.31: Degradation mechanism of the etched aluminium surface. Nano-scale asperities are broken during icing/deicing cycling. Taken from [78].

Chen *et al.* [81] looked at the effect of microstructure on degradation of superhydrophobic surfaces during cycling. The surface of an aluminum alloy was patterned by photolithography and etching steps to create micro-scale roughness, and then dip-coated in a FAS-13/deionized water solution which also contained TiO_2 nanoparticles, creating a hierarchically rough superhydrophobic surface. Cycling was performed by placing a 5 µl droplet on the surface and then cooling to -10 °C. When the droplet was frozen, it was removed by force. The difference in degradation between micro-posts (height of 6 – 15 µm, spacing of 23 – 30 µm) and closed-cell honeycomb structures (side-lengths 20 – 30 µm) can be seen in Figure 2.32.

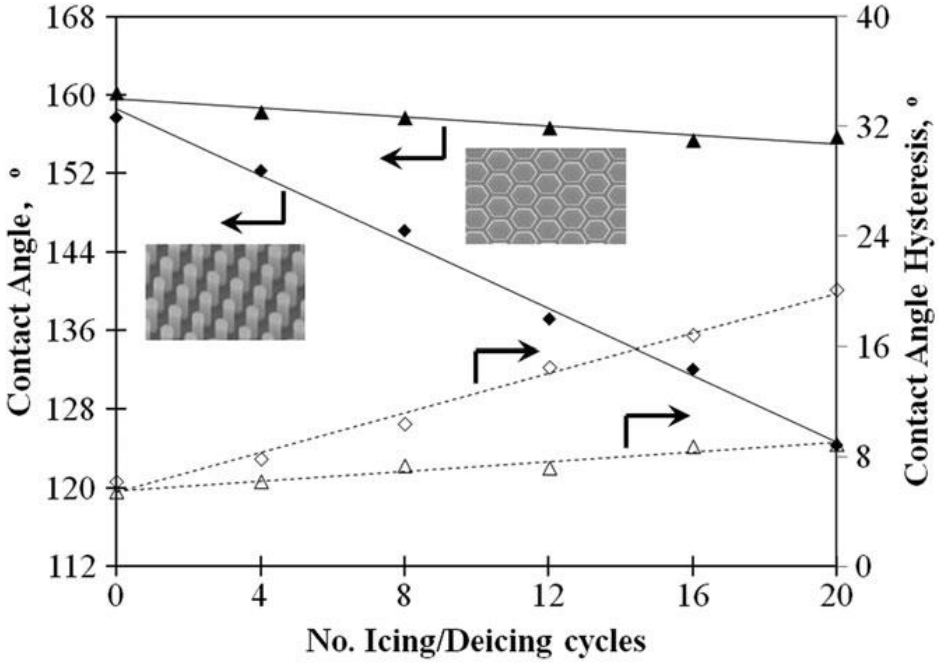

Figure 2.32: Contact angle and contact angle hysteresis over 20 icing/deicing cycles for micropillars (diamonds) and honeycomb cells (triangles).Taken from [81].

Clear degradation was seen for the micro-pillars, including a loss of their superhydrophobicity within 5 cycles, while the honeycomb structures remained superhydrophobic after 20 cycles. The reason given for this difference was that that the ice-removing force was transferred through the ice and applied directly to each individual pillar; because each pillar has no external support, they were easily destroyed. In the case of the closed-cell honeycomb structures, the force was spread across the entire network, decreasing the load on any given microstructure. Because of this the authors claim that the degradation is due to a change in morphology, though no chemical investigation into the removal of the hydrophobic coating is performed.

Finally, a second study on HMDSO-coated anodized aluminum was performed by Mobarakeh *et al.*[82], this time with the HMDSO deposition time increased from 15 to 25 minutes (no thickness is given in either case). The effect of cycling on both the ice adhesion and surface wettability can be seen in Figure 2.34. The durability of the samples is notably improved over what was seen in Figure 2.28.

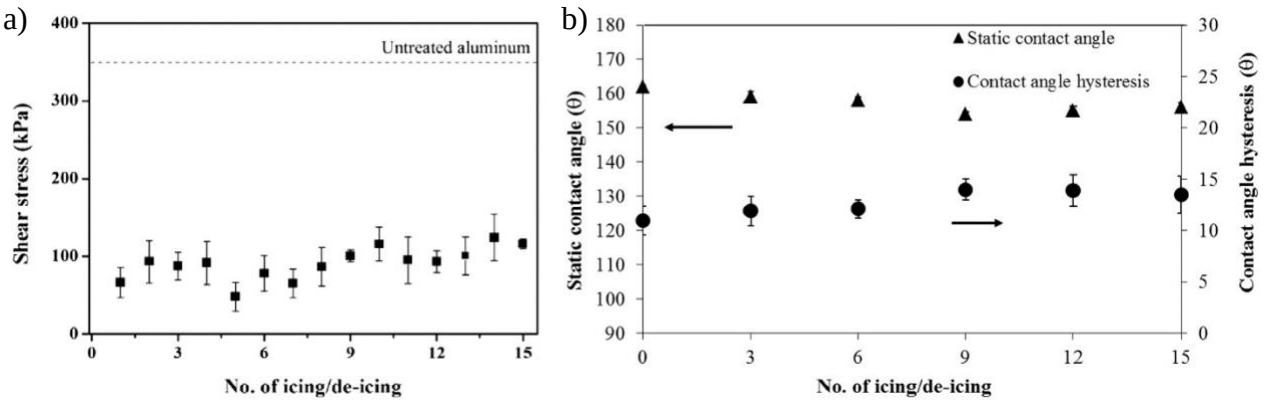

Figure 2.33: Degradation of surface via a) shear stress (ice adhesion) and b) contact angle and hysteresis measurements after 15 icing/deicing cycles. Adapted from [82].

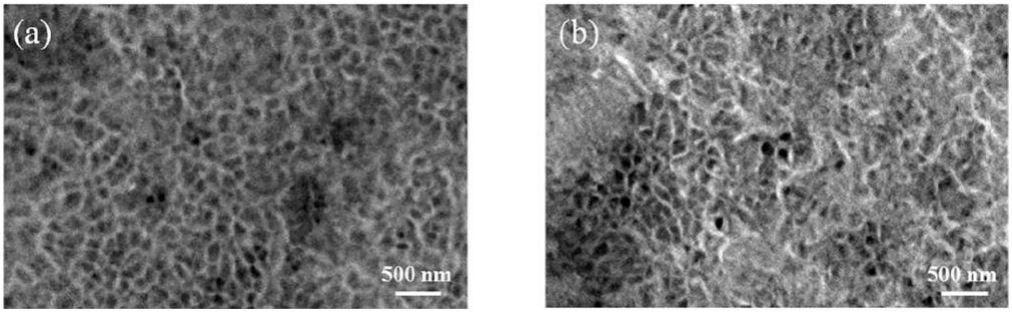

Figure 2.34: HMDSO-coated anodized aluminium a) before and b) after 15 icing/deicing cycles. Taken from [82].

SEM images before and after cycling can be seen in Figure 2.34. These results are very different from what had previously been seen, with a similar morphology present in both cases. The authors suggest that the thicker coating has protected the morphology, and any changes seen are expected to be chemical. This is supported by XPS measurements performed before and after cycling, which can be found in Table 2.5. It can be seen that carbon and silicon contents decrease, while oxygen and aluminum increase. The increase in aluminum indicates some removal of the coating, while

the decrease in carbon and increase in oxygen are most likely responsible for the changes in wettability. Specifically mentioned is a decrease in the methyl groups, with $(CH_3)_x$-Si-O content decreasing from 25 at. % before cycling to 12 at. % after.

Table 2.5: XPS measurements of elemental composition of the surface before and after cycling. Adapted from [82].

Sample	C	Si	O	Al
Before	42	20	34	4
After	26	11	43	20

2.3 HMDSO and DLC:SiO_x coatings

Hexamethyldisiloxane (HMDSO) is a liquid organosilicon compound. It is centered by an oxygen atom which is bonded to two silicon atoms, and these are in turn bonded to three methyl groups each. Its structure can be seen in Figure 2.35. It can be polymerized in plasma, and has been used in applications ranging from optics to food packaging [83]. Of specific interest in this work is the fact that its abundance of methyl groups mean that the polymerized films can be highly hydrophobic [84]. Plasma polymerization of HMDSO can be performed both at atmosphere [85], as well as in low-pressure vacuum systems [86][87].

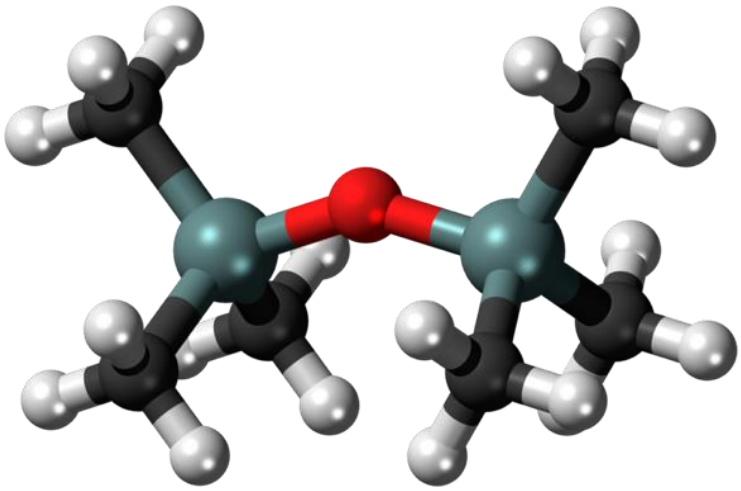

Figure 2.35 : Ball and stick model of hexamethyldisiloxane molecule. Taken from [88].

A particular area of interest is exactly how hydrophobic the deposited films can be, and how they perform when used as hydrophobic top layers for superhydrophobic and icephobic surfaces. Because the hydrophobicity of a plasma-polymerized HMDSO (PP-HMDSO) film is dependent on methyl groups forming at the surface [83], we can predict a maximum possible contact angle of 111°.

In work done by Zanini *et al.* [87], a maximum observed contact angle of 104 ° was seen for PP-HMDSO films. It was also shown that the contact angle of PP-HMDSO decreases along with the $SiCH_3/CH_x$ ratio in the films, and that this ratio decreases as power input is increased (Figure 2.36). Also visible in Figure 2.36 is a decrease in CA with increase in deposition time, however, this is due to a limitation of the experiment. HMDSO vapor was allowed to flow into the chamber via a micrometer valve until a pressure of 1 mbar was reached, at which point the valve was closed, and no further flow occurred. It has been shown in other works where this flow was not restricted that deposition time did not have a large influence on contact angle [83][84], and thus it is likely that the decrease seen in Figure 2.36 is due to effects other than the continued polymerization of the HMDSO vapor.

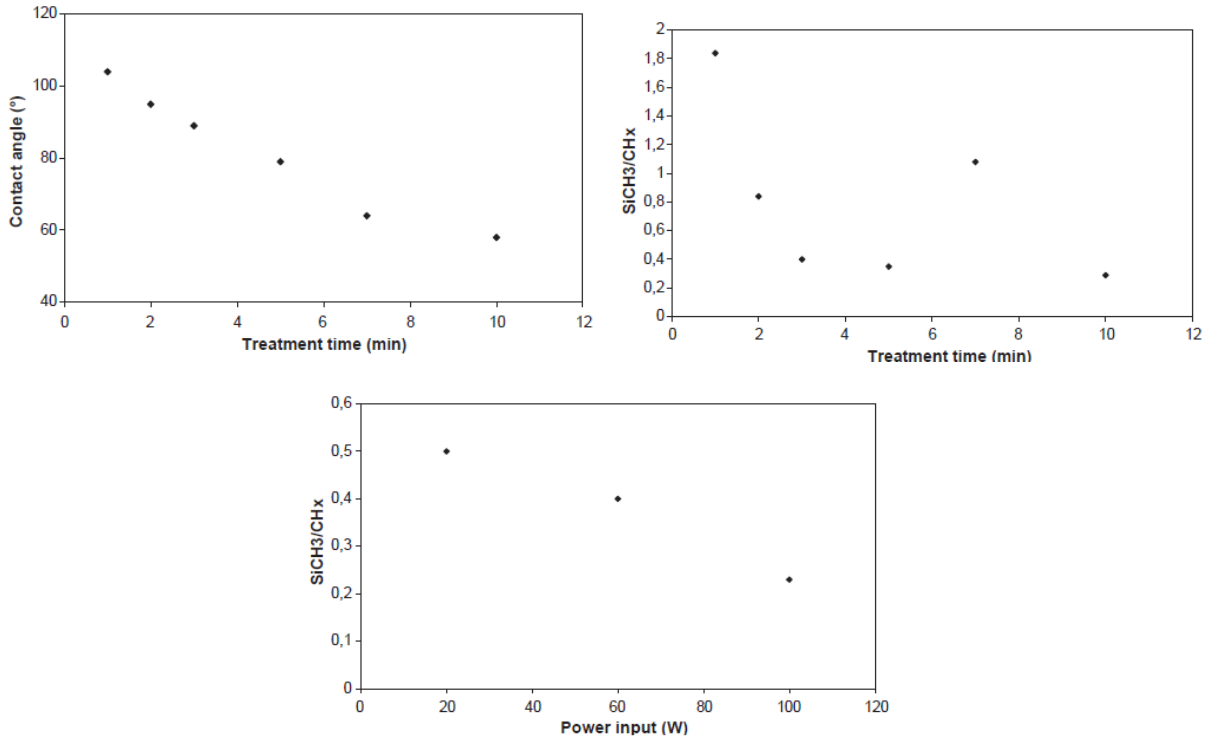

Figure 2.36: Contact angle and chemical ratios (via FT-IR) for plasma-polymerized HMDSO. Taken from [87].

Further work from the same group explored the growth mechanisms of PP-HMDSO on flat and etched silicon. Films were shown to grow via islands, and preferential nucleation around surface features was noted [83]. This can be seen in Figure 2.37, where we can also observe the formation of "globs" along surface features when coated, which has the effect of exaggerating their size and decreasing any sharpness. An increase in power was again linked to a decrease in methyl groups and thus, hydrophobicity; this same effect also occurred when adding oxygen to the flow.

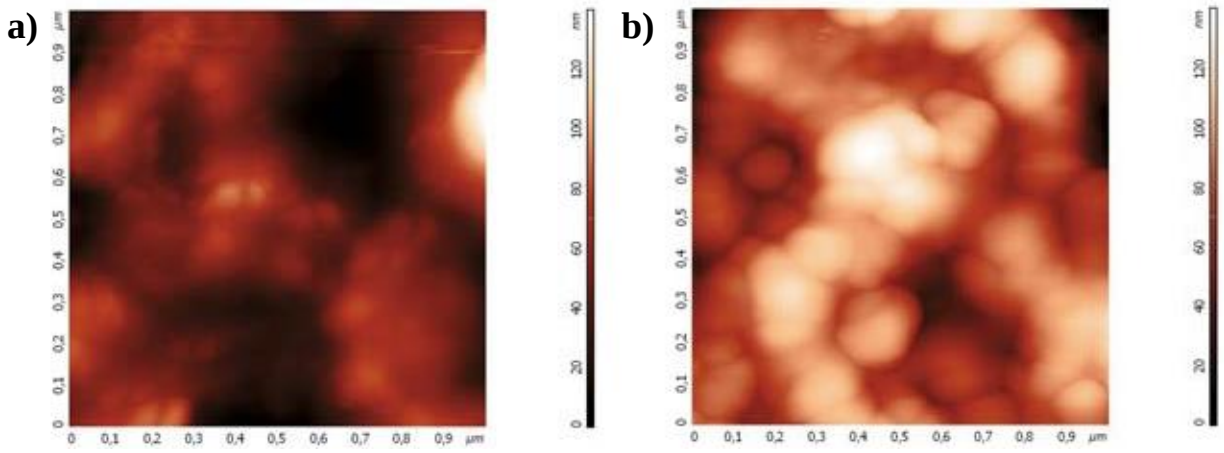

Figure 2.37: AFM images of etched silicon a) before and b) after 50nm coating with PP-HMDSO. Preferential nucleation at the sites of surface features creates "globs" which smooth the surface. Taken from [83].

With the hydrophobic potential of PP-HMDSO established, it is not a stretch to imagine its application being pushed to superhydrophobic and even icephobic surfaces, which is exactly what has been done by researchers at Université de Québec à Chicoutimi over the last number of years. Focusing on anodized aluminum substrates, they were able to first confirm contact angles above 150 ° when coating with HMDSO, though the minimum contact angle hysteresis achieved was 40 ° [86]. It was again shown that an increase in power resulted in a decrease of the $SiCH_3/CH_x$ ratio, which in turn reduced the hydrophobicity of films. Offered as an explanation for this was the fact that increased power also lead to a greater breakdown of the HMDSO molecules, potentially causing dissociation of the methyl groups.

Optimization of both the anodization and film deposition conditions allowed for the obtention of truly superhydrophobic surfaces, with CA up to 158° and a roll-off angle of 8°. These samples were then tested for icephobicity, and were shown to reduce the ice adhesion of aluminum from

350 ± 25 kPa to 100 ± 9 kPa [80]. By increasing the deposition time from 15 to 25 minutes (no corresponding thicknesses are given), Mobarakeh *et al.* obtained an increase in CA to 162 ± 3°, with a corresponding decrease in sliding angle and ice adhesion to 3 ° and 83 ± 5 kPa, respectively [82]. The results of icing/deicing cycles for these samples has already been presented in section 2.2.4, however these final samples also showed promising results in resistance to UV degradation, lengthy water submersion, and corrosion.

While HMDSO allows for the deposition of highly hydrophobic films, and a clear improvement in these films has been made over time, its soft polymeric nature means that durability is always a concern. Indeed, hardness values are not even considered, let alone reported, in the literature for HMDSO-only films. In order to improve the mechanical properties of hydrophobic coatings, we can look at a mechanically robust coating which is easily deposited by PECVD: diamond-like carbon (DLC).

Diamond-like carbon is an amorphous carbon material which exhibits some properties similar to diamond – it has a high hardness, high elastic modulus, and is chemically inert – while having no grain boundaries and being cheaper to produce [89]. Because of this it is widely used in industry, from automotive components to biomedical applications [90]. DLC is often deposited from methane [91] or acetylene [92] sources, with acetylene giving a higher deposition rate due to its equal number of carbon and hydrogen atoms.

Different types of amorphous carbon can be developed based on their percentage of sp^2 and sp^3 carbon bonds, as well as their hydrogen content. The relationships between these can be seen in Figure 2.38. When hydrogen is present, it is not chemically bonded to the carbon atoms, but rather trapped inside of the network [90]. Mentions of DLC in this work will be in reference to hydrogenated amorphous carbon (a-C:H), which is comprised of 40-60% sp^3 bonds, 30-50 % hydrogen [89], and has a hardness in the range of 15 – 40 GPa [90]. A comparison of the hardness to other commonly deposited materials can be found in Figure 2.39.

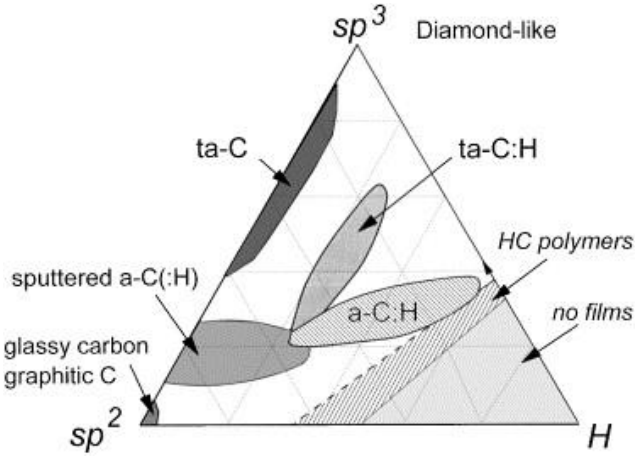

Figure 2.38: The types of DLC which can be deposited depending on the content of sp^2 carbon bonds, sp^3 carbon bonds, and hydrogen. Taken from [89].

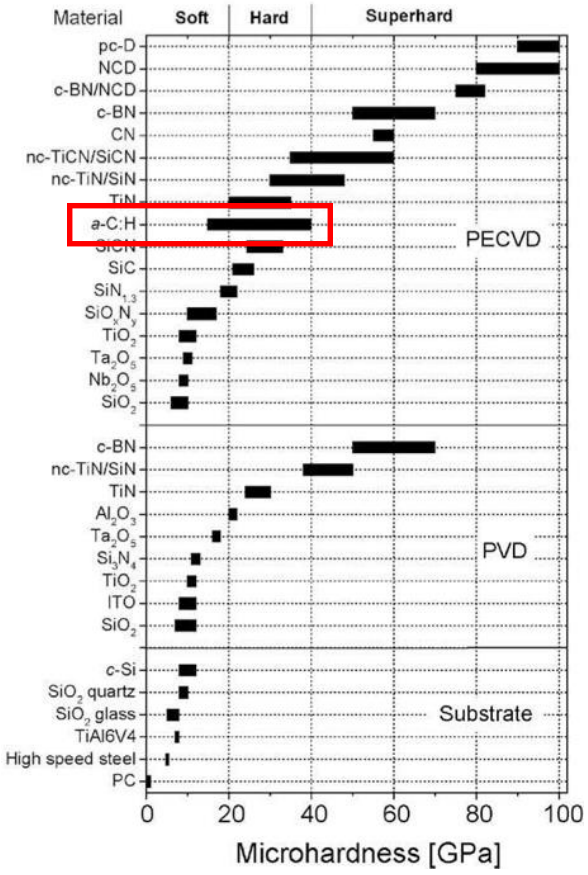

Figure 2.39: Microhardness for commonly deposited materials, with a-C:H highlighted. Depending on deposition conditions, a-C:H may be soft or hard, but will not be superhard. Taken from [90].

DLC on its own is hydrophilic with a contact angle of ~60° [91], and contact angle decreases further with increase in electrode bias voltage [27][93]. Increasing bias has been shown to reduce both the sp^2/sp^3 bond ratio, and the hydrogen content of films [94]. It has been shown that a decrease in hydrogen increases the film hardness but decreases the contact angle [91], and that the ratio of sp^2/sp^3 bonds is directly related to contact angle as well [95]. In the latter case, the most extreme example of this is the ~35° contact angle for diamond, which is 100% sp^3 bonds, vs the ~77° contact angle for graphite, which is entirely sp^2 bonds. Finally, when considering DLC as a coating for any feature-rich surface, it should be noted that it has a smoothing effect due to its amorphous nature [96].

In an effort to develop hydrophobic coatings which exhibited many of the most desirable properties of DLC, researchers began doping DLC with HMDSO, or other similar compounds which incorporated silicon and oxygen into the DLC network while maintaining methyl groups which provide hydrophobicity. This became popular in the late 90's as an alternative to fluorine-containing DLCs, offering greater chemical stability as well as reducing dependence on environmentally harmful fluorocarbons [97]. The incorporation of SiO_x into DLC also has the advantage of reducing film stress [98].

One of the biggest challenges is that like both DLC and HMDSO on their own, the contact angle of DLC:SiO_x films decrease with bias [99], whereas hardness increases with bias [100]. Given that the addition of silicon and oxygen leads to a decrease in film hardness compared to "pure" DLC [98], this inverse proportionality means that there is a very real limit to how hard coatings can be if hydrophobicity is desired. In general, hydrophobic DLC:SiO_x coatings can be expected to have a hardness of 7 – 10 GPa, with a maximum contact angle of 100° [97]. If the need for hydrophobicity is removed, then DLC:SiO_x coatings have been developed with hardness up to 23 GPa [101].

Many authors speculate as to what effect the silicon and oxygen content in DLC:SiO_x films has on wettability, however, there is no true consensus on this matter [102]. This can be clearly seen in Figure 2.40, which shows that deposition techniques seem to play a larger role in the contact angles of the deposited films than the content of either element. That being said, when restricted to a given deposition technique, certain trends do emerge. In the case of capacitively coupled PECVD (black-filled shapes in Figure 2.40), the contact angle is 90° at a 0.0 O/Si ratio, appears to hit a maximum

of 100° at a ~0.8 O/Si ratio, and then drops steadily with an increase in oxygen. In the case of ion beam depositions (unfilled shapes in Figure 2.40), we see an opposite effect, with contact angles increasing with oxygen levels, though this could just be noise given the small range of both the concentration ratio and contact angle values. For high-frequency PECVD (grey-filled shapes in Figure 2.40), we have a single value of a 74° CA at a 0.5 O/Si ratio, which does not correspond with the other measurements in any way. Also notable is the fact that these last two techniques never achieve hydrophobic surfaces, and even for capacitively coupled PECVD, there appears to be only a small window of O/Si ratios where hydrophobicity will be achieved.

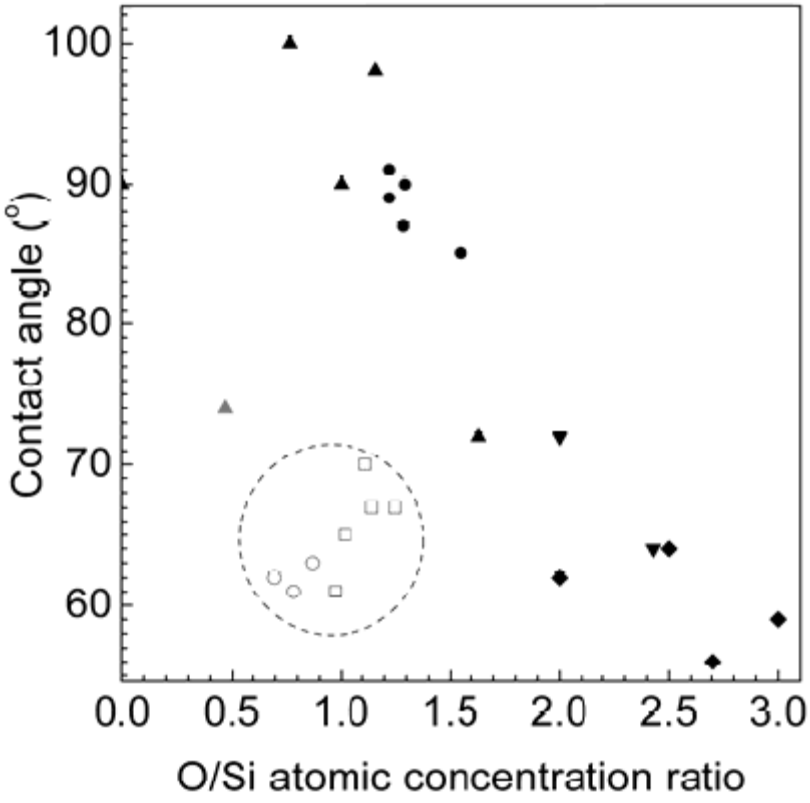

Figure 2.40: Contact angle as a function of O/Si atomic concentration ratio. Black-filled shapes are deposited by capacitively coupled PECVD, grey-filled shapes by high-frequency PECVD, and unfilled shapes by closed drift ion beam. Different shapes indicate that the data comes from different sources. Adapted from [102].

It has been shown then that DLC:SiO_x films, especially when deposited by capacitively coupled PECVD, can be highly hydrophobic and also exhibit a relatively high hardness. While HMDSO has been used for icephobic coatings and DLC:SiO_x has been shown to give superhydrophobic

surfaces when coating hierarchical patterns [99], there have been no reports in the literature on the usage of DLC:SiO_x for icephobic coatings. This leaves an opening for interesting work in testing the durability of DLC:SiO_x-based coatings when used for icephobic applications.

2.4 Fabrication methods

The final section of this literature review will give a brief introduction into the fabrication methods used to develop the thin-on-thick coating system presented in this thesis. The thin layer is deposited by plasma-enhanced chemical vapor deposition (PECVD), while the thick layer is deposited by thermal spraying, specifically suspension plasma spray. In each case, the basic physical principles of the technique will be presented. In the case of thermal spraying, recent applications of the technology in the context of superhydrophobicity and icephobicity will be reviewed. This will be omitted for PECVD, as its use in the deposition of HMDSO and DLC:SiO_x coatings for icephobic and other applications have been discussed at length in the previous section.

2.4.1 Plasma-enhanced chemical vapor deposition

PECVD is a deposition technique similar to traditional chemical vapor deposition (CVD), which differentiates itself by using plasma rather than thermal energy to activate reactant gases and deposit a film [103]. This allows films to be deposited at much lower temperatures, which in turn allows deposition on a wider range of substrates. It is sometimes called plasma assisted chemical vapor deposition, or simply plasma chemical vapor deposition.

A basic PECVD deposition takes place as follows: substrates are placed in a vacuum chamber, which is pumped down to high vacuum (~10^{-6} Torr). Reactant gases are then introduced into the vacuum chamber at controlled flow rates, and with a controlled total chamber pressure. An RF generator is connected to an electrode inside of the chamber, and a negative bias voltage, V_B, is applied at 13.56 MHz. This is the biased electrode; a grounded electrode may also be present, or the vacuum chamber itself may function as the grounded electrode for capacitive coupling. The effect of applying the bias is two-fold: the electrode becomes negatively charged, and the negative pulses knock electrons off the atoms or molecules, causing them to become ionized and creating the plasma. These ionized molecules bond with the substrate; depending on the molecule/substrate combination, the molecule may decompose leaving one species on the surface while another is extracted from the chamber by the vacuum system [89]. This process is shown in Figure 2.41.

Growth rate and film density can be improved by having the biased electrode function as the sample holder, which causes the ionized molecules to be attracted to the samples themselves in the case of electrically conductive substrates.

PECVD can be used to deposit organic (diamond-like carbon, diamond, plasma polymers) and inorganic (oxides, nitrides, carbides) films, and can be used to coat complex shapes [90]. Because of its versatility, it has been used in a wide range of applications, from protective coatings to transistors to optical filters.

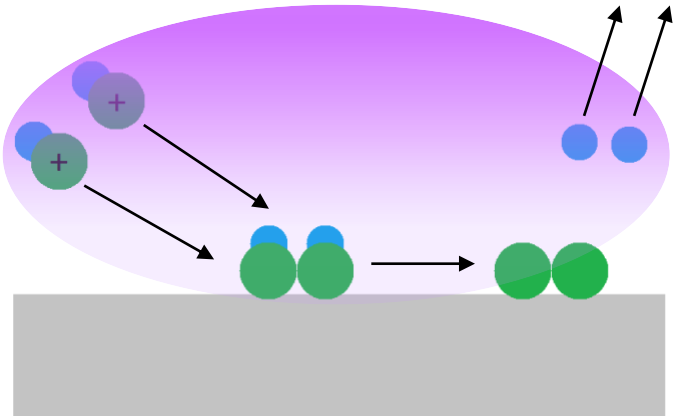

Figure 2.41: Schematic of a simple PECVD deposition. Positively charged particles are present in the plasma. These particles then adsorb to the surface, desorption of some species may occur, and gaseous by-products are extracted by the vacuum system.

2.4.2 Thermal Spray

The term “Thermal Spray” covers a wide range of spray deposition techniques in which particles are accelerated towards a surface, and splat on the surface upon meeting it, with successive layers of splats creating a coating. The principle steps of thermal spray deposition can be seen in Figure 2.42, and will be explained using the specific case of plasma spraying. The substrate surface is first prepared, often by sandblasting, to improve film adhesion. Deposition begins with the generation of a plasma from a plasma torch. Feedstock is then introduced into the plasma. The feedstock is the material which will be used as the coating, unless it is to be changed in some way through interaction with the plasma, in which case the resultant material will be deposited. The plasma interacts with the feedstock particles, heating and accelerating them. Finally, the particles splat on

the surface and solidify, creating the coating [103]. Depending on the feedstock and the energetic gas flow, other interactions aside from heating may occur.

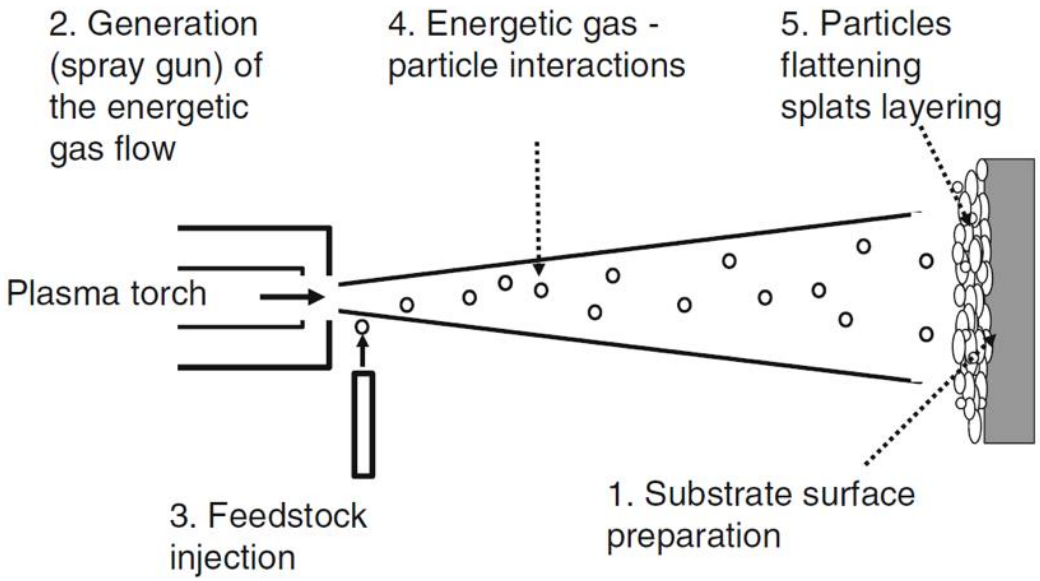

Figure 2.42: The steps of thermal spray deposition. Taken From [103].

While thermal spraying has long been used in applications such as thermal barrier and wear-resistant coatings [45], There have recently been a number of publications showcasing its use in the development of superhydrophobic and icephobic surfaces. Sharifi *et al.* [56] showed that hierarchically rough TiO_2 surfaces could be deposited through suspension plasma spray, a type of thermal spray in which the material to be deposited is dispersed in a liquid suspension, and this suspension is fed into a plasma jet for deposition. When coated with hydrophobic stearic acid, these were shown to be superhydrophobic.

Similarly, Liu *et al.* [44] deposited MCrAlY (M = Ni, Co) by thermal spray on aluminum alloy substrates. These surfaces showed hierarchical roughness and became superhydrophobic when coated with a low surface energy material. An SEM image of this surface Figure 2.43. Ice adhesion tests of these samples consistently gave results below 100 kPa.

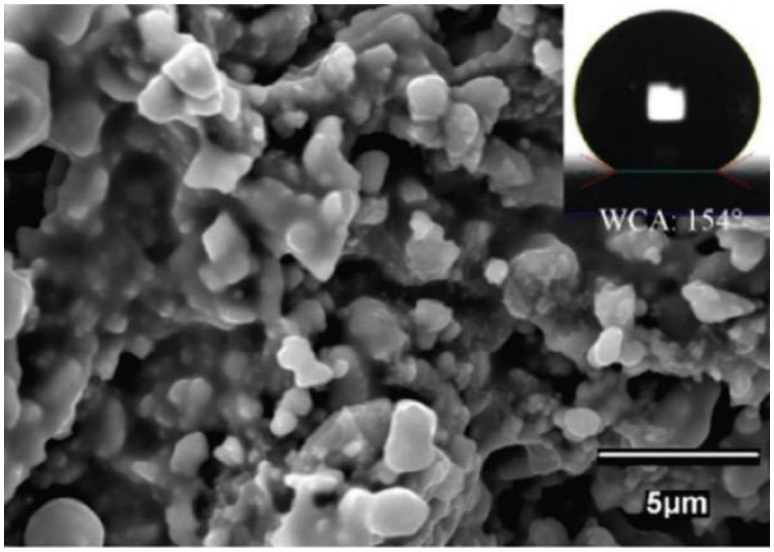

Figure 2.43: SEM image of thermal sprayed MCrAlY, coated with a low surface energy material. Inset shows the contact angle of this surface. Taken from [44].

Lastly, icephobic coatings have also been sprayed from polymers, with Koivuluoto *et al.* [63] spraying polyethylene coatings onto stainless steel. As opposed to the others mentioned, these are flat coatings which were further polished to reduce surface roughness. Ice adhesion for these coatings was shown to be below 60 kPa, however, the ice detachment mechanism was not discussed by the authors.

CHAPTER 3 METHODOLOGY

This chapter will present the methodologies used throughout this thesis, beginning with coating deposition, followed by physical characterization of the deposited coatings, and ending with durability tests performed on the full thin-on-thick coating system. In the case of sample characterization equipment, a brief explanation of the system's functionality will be provided, along with the specifics of the system itself, and the parameters used.

3.1 Coating deposition

3.1.1 Plasma-enhanced chemical vapor deposition

The films developed in this work were deposited in an RF plasma using a system schematically shown in Figure 3.1. It consisted of a stainless steel vacuum chamber, 30 cm in diameter, a pumping system with turbomolecular (Varian V 300 ICE) and mechanical (Varian CP 451) pumps equipped for corrosive gases, a gas distribution system, and an RF power supply unit. The chamber pressure was measured by an MKS capacitance gauge and the pumping speed was regulated by a throttling valve (Vacuum General MDV 040). The flow of gases, namely SiH4, N_2, C_2H_2, and Ar was controlled by an MKS mass flow controller in each line, and gas flows were monitored by computer using LabVIEW software. The flow of HMDSO vapor was controlled by a micrometer valve placed in line between the chamber and a glass beaker containing liquid HMDSO. RF power was supplied from an Advanced Energy RFX II 3000 (13.56 MHz) generator through a matching unit (Advanced Energy, ATX 800) that was connected to a substrate holder-electrode 15 cm in diameter. A second, grounded electrode 10 cm in diameter was mounted in parallel above the biased electrode. Applying RF power to the substrate holder in a capacitively coupled discharge leads to the formation of a self-induced DC negative bias voltage, V_B. The value of V_B allows one to control the energy of the bombarding ions, as this is proportional to the difference between the plasma potential and V_B. Measurement of V_B was performed by a voltmeter incorporated in the controller of the matching unit. PECVD in glow discharges is usually performed at low pressures, in the range from 10^{-4} Torr to several Torr (1.33×10^{-3} to about 500 Pa). Under these conditions, the density of electrons (or ions, plasma density, n_e) is typically between 1×10^9 and 1×10^{11} cm^{-3}.

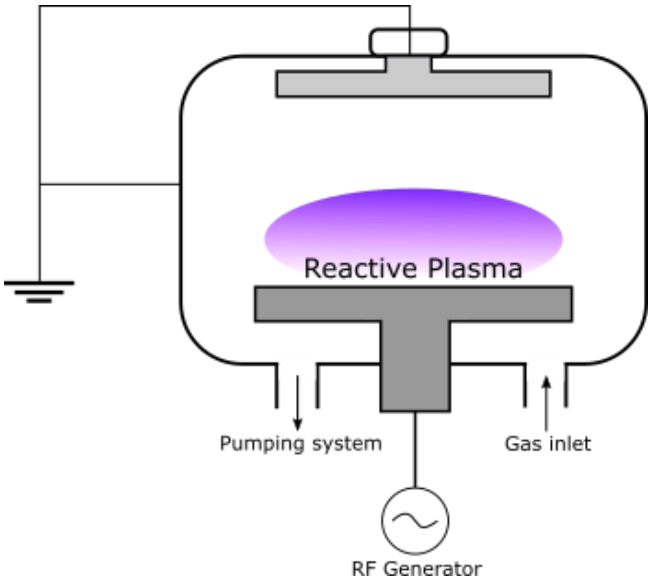

Figure 3.1: Schematic of the PECVD deposition system.

Three different types of films were deposited by PECVD: SiN_x, plasma-polymerized hexamethyldisiloxane (pp-HMDSO), and silicon-and-oxygen-containing diamond-like carbon (DLC:SiO_x). SiN_x was deposited using 20 sccm Ar, 25 sccm N_2, and 10 sccm SiH_4, at a working pressure of 50 mTorr and with a V_B of -400 V. Deposition of pp-HMDSO films was performed with V_B ranging from -25 V to -250 V, working pressures from 100 to 200 mTorr, and HMDSO partial pressures from 0.5 to 2.5 mTorr. The HMDSO flow in this work is reported as a partial pressure only, as no mass flow controller was connected to its line. This partial pressure is measured by the same MKS capacitance gauge which measures the chamber pressure. Depositions were performed on both the ground and biased electrodes, which can be seen in Figure 3.2. DLC:SiO_x films were deposited using 0 to 50 sccm Ar, HMDSO partial pressures of 0.8 to 3.7 mTorr, V_B values of -100 to -1000 V, and working pressures of 25 to 100 mTorr. The 3.7mTorr HMDSO partial pressure corresponds to the micrometer valve being fully opened and is the highest value obtainable in our system.

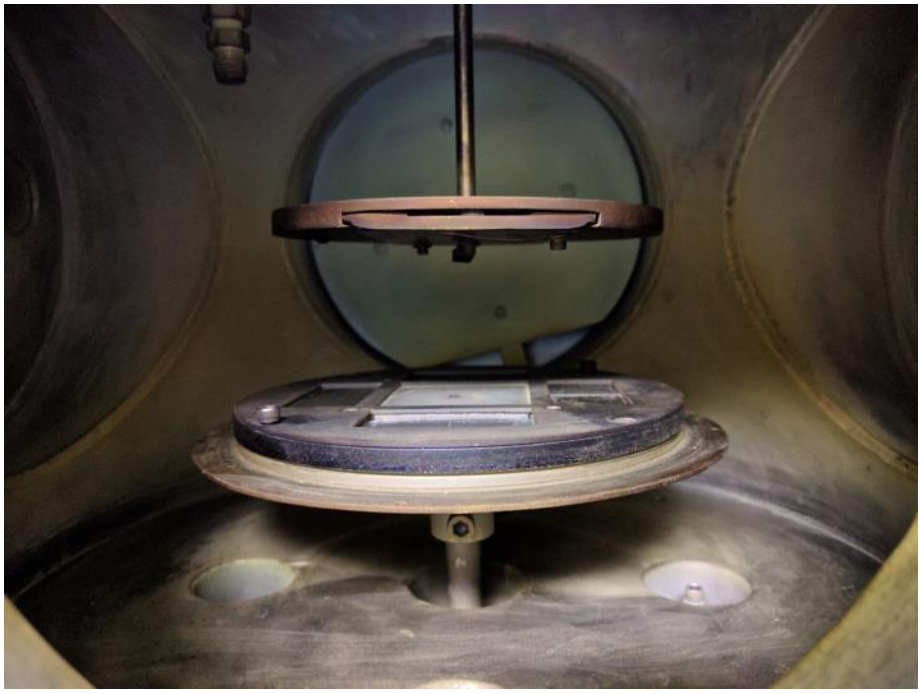

Figure 3.2: PECVD chamber, showing both the biased (bottom) and grounded (top) electrodes.

3.1.2 Suspension-plasma-spray

The "thick" coatings used in this work are suspension plasma spray (SPS) TiO_2 coatings developed by Navid Sharifi, Cristian Moreau, Ali Dolatabadi, and Martin Pugh of Concordia University, and were provided to us as part of the Phobic2Ice research project. What follows is a brief description of coating fabrication; the full details on the initial development [56] and optimization [45] of these coatings can be found in the literature.

TiO_2 coatings are deposited by SPS, using a sub-micron titanium dioxide powder mixed at 10 wt.% in an ethanol-based suspension. The substrate is first grit blasted with 180 grit alumina particles to increase its roughness and to create growth sites for larger surface features during the TiO2 deposition. The plasma power during deposition is 36 kW. The selection of plasma power, suspension composition, suspension solid content, and plasma gas velocity have been shown to be critical in obtaining the desired morphology, while the roughness after grit-blasting plays a lesser role [45].

3.1.3 Other depositions

The HMDSO and DLC:SiO_x coatings developed in this work were compared to other films deposited by thermal evaporation and dip-coating. The thermally evaporated coating was a commercially available fluoropolymer, Optron OF110. Deposition was performed in a BOXER vacuum coating system from Leybold optics. One "capsule" of Optron OF 110 consists of metal fibers coated with the fluoropolymer in a copper crucible. The capsule is placed on a heating element, which has a 3.0 A current run through it. This causes the fluoropolymer to evaporate, and it is deposited on whatever surface it encounters. Thickness is measured by a quartz crystal microbalance, and each capsule produces a coating ~7 nm thick.

Dip-coating was used to coat samples with stearic acid. A stearic acid solution was prepared by mixing 0.5 wt.% stearic acid into 1-propanol. Samples were then dipped into the solution and left at room temperature to dry.

3.2 Physical Characterization

3.2.1 Optical interferometry and roughness calculations

Optical interferometry is a method used to quickly obtain the profile of a surface. A schematic of an optical interferometer can be found in Figure 3.3. The functionality of the system begins with a light source, and from here a beam splitter is used to direct the light toward an objective lens. A lower beam splitter is present in the lens of the objective, and this directs the light towards the sample surface as well as a reference mirror. Upon reflecting from the surface and the reference mirror, the beams of light recombine and are sent to a digital image sensor. When the distance between the reference mirror and the surface is nearly identical, interference is observed due to a change in intensity of the recombined light[104].

The objective performs a sweep in the z-direction, and at every height, interference is seen or not seen for each pixel of the digital image sensor. The highest point at which interference is observed for a given pixel is recorded in software, and the map of these points gives the profile of the surface [105].

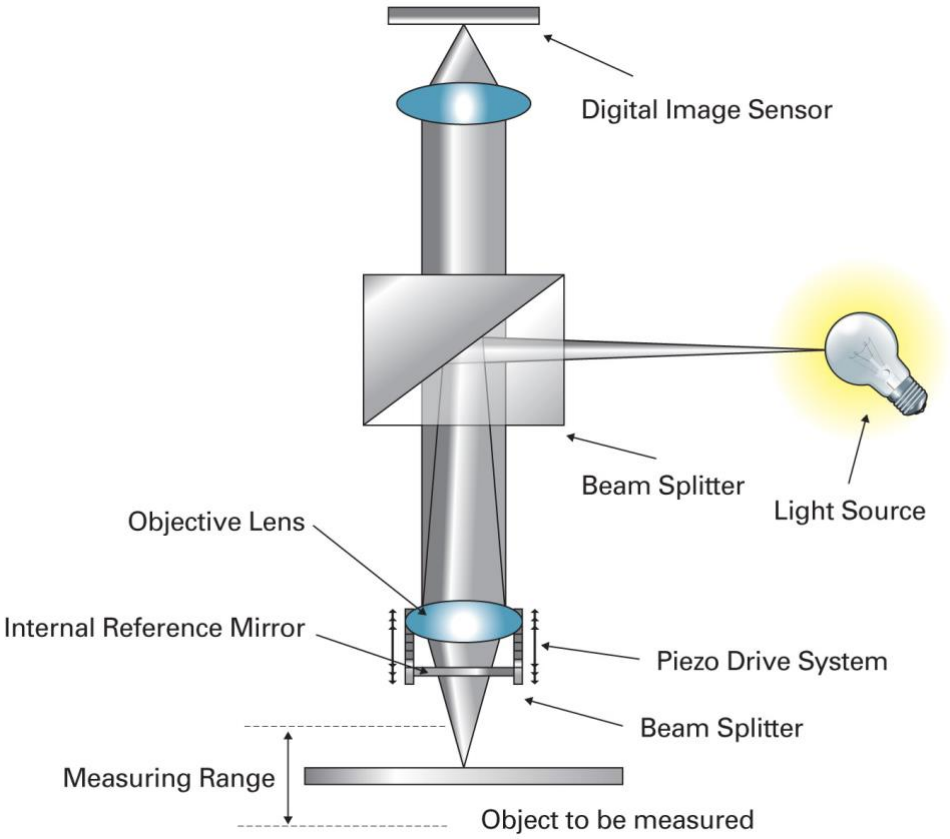

Figure 3.3: Schematic of an optical interferometer. Taken from [105].

Measurements in this work were performed using a Bruker ContourGT-K optical interferometer, at magnifications of 5x and 20x, and at least 4 measurements were taken for all samples. Surface profiles were analyzed in the Bruker's Vision64 software, as well as using the open-source software Gwyddion [106], in order to measure the heights of surface features as well as to determine the roughness properties of the surfaces.

Roughness parameters are defined in relation to a mean height line (or plane in two dimensions) which intersects the surface profile at the mean height. This line is taken to have a value of $z = 0$, while points below it have negative values, and points above it have positive values. To distinguish the average roughness of a scanned three-dimensional surface from that granted by a single line-scan, we use the parameter label S_a rather than the more traditional R_a [107]. S_a is calculated from the following equation:

$$S_a = \frac{1}{A}\iint_A |z(x,y)|\,dxdy \tag{3.1}$$

where *A* is the sample area. Similarly, the root mean square (RMS) height of a surface can be calculated by:

$$S_q = \sqrt{\frac{1}{A}\iint_A z^2\,(x,y)dxdy} \tag{3.2}$$

The limitation of average feature height measurements is that they are based entirely differences between asperity heights and the mean height line, but they do not give us any information about the shapes of the asperities. To address this, we can look at the skewness and kurtosis of a sample.

The skewness of a sample is a measure of symmetry with respect to the mean height line, and it is obtained by dividing the mean of the cube of the height values by the RMS Roughness cubed:

$$S_{sk} = \frac{1}{{S_q}^3}\frac{1}{A}\iint_A z^3(x,y)\,dxdy \tag{3.3}$$

A skewness value of $S_{sk} = 0$ corresponds to a surface with a Gaussian height distribution, while a positive value corresponds to a majority of the material being below the mean line (resulting in large peaks), and a negative skew corresponds to most of the material being above the mean line (resulting in large valleys) [108]. This difference is illustrated in Figure 3.4.

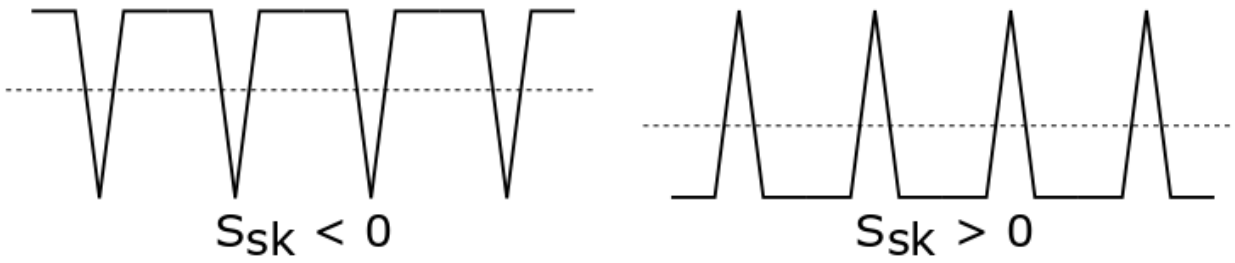

Figure 3.4: Profiles associated with negative and positive skewness.

The kurtosis of a sample represents the sharpness of the surface features and their distribution. It is obtained by dividing the mean of the fourth power of the height values by the RMS Roughness set to the fourth power:

$$S_{ku} = \frac{1}{{S_q}^4}\frac{1}{A}\iint_A z^4(x,y)\,dxdy \tag{3.4}$$

A kurtosis value of 3 corresponds to a Gaussian height distribution along the surface, while a value $S_{ku} > 3$ indicates a spiky surface and a value $0 < S_{ku} < 3$ indicates a flatter surface. Examples of these are indicated in Figure 3.5

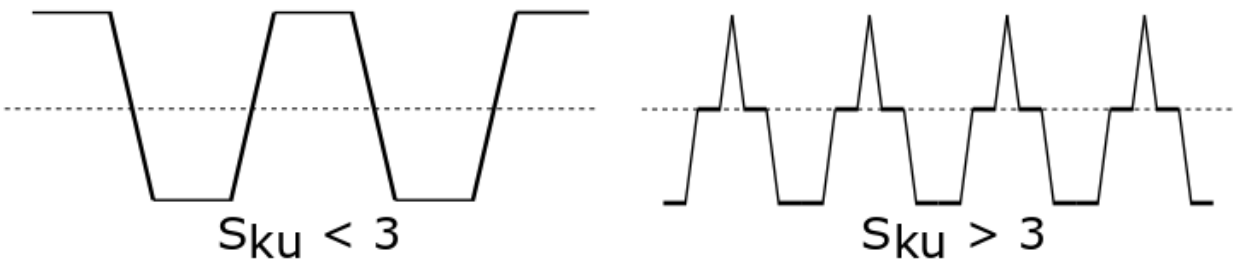

Figure 3.5: Profiles associated with kurtosis values less than and greater than 3.

3.2.2 Mechanical profilometry

Mechanical profilometry is performed by dragging a stylus across a surface and measuring the changes in height as it traverses the surface features. The stylus approaches the surface, and is placed upon it with a set force, which is too low to damage the sample, but high enough to ensure that constant contact between the stylus and the surface is maintained. The sample is moved by a stage, while the stylus is kept fixed in the x- and y-planes.

In this work mechanical profilometry was used to determine film thickness. A step was first created on the surface by placing Kapton tape on the substrate before film deposition, and removing it after the film was deposited. This was performed for both single films as well as multi-film stacks. The step height was then measured using a Bruker DektakXT mechanical profilometer, with a stylus force of 5 mg and a typical scanning speed of 200 µm/second.

3.2.3 Scanning electron microscopy

Scanning electron microscopy is a microscopy technique which allows for high-magnification imaging of a variety of conductive materials. Measurements are performed in a vacuum chamber, where a focused electron beam scans the surface in a raster pattern. Inelastic collisions with the

electron beam cause the excitation of electrons at or a few nanometers below the surface, and these secondary electrons are emitted. The secondary electrons are detected upon leaving the surface, with the detected values corresponding to a beam location during the scan. From this information, topographical imaging of the surface can be performed. This allows for much higher resolution imaging than optical microscopy, which is limited by diffraction.

The SEM used in this word was a JEOL JSM-7600F, using a voltage of 5.0 kV and a working distance of approximately 12 mm. In these conditions, a magnification of 5000x is easily reached, at which point sub-micron surface features can be clearly discerned.

3.2.4 Water contact angle measurements

The contact angle measurements presented in this study were performed on two different systems. The first was an Attension Theta optical tensiometer from Biolin scientific, located at Université de Montréal. This system features an automated droplet dispensing system allowing the user to define droplet volume, as well as a tilting cradle. It features a built-in camera, and the Attension software calculated the contact angle using the Young-Laplace method, which improves accuracy by accounting for the drop's distorted shape due the weight of the liquid [86]. Static contact angle measurements were performed using a 5 µl droplet of distilled water. Contact angle hysteresis measurements were performed using the tilting method described in Chapter 2, with a 10 µl droplet.

The second system used was a home-made system at Concordia University. Here droplet size was controlled by a Ramé-Hart Auto Dispensing System 100-22 set to produce 10 µl droplets, and images were captured using a Nikon D90 camera with a macro lens. Contact angle hysteresis measurements were performed using the droplet inflating/deflating method, inflating a droplet from 0 µl to 10 µl, and then deflating back to 0 µl. In each case, images were analyzed using the Dropsnake plugin for ImageJ [109].

The two systems were tested for consistency, and measurements were found to be within uncertainty of each other. A minimum of three measurements were performed for all tests.

3.2.5 Nanoindentation

To characterize the mechanical properties of the studied coatings, a nanoindentation system (Hysitron TriboIndenter) was used. To perform indentation tests, a load is placed on a diamond

Berkovich indentation tip, which indents the sample being tested. Displacement of the tip is recorded as the load progressively increases to a pre-defined maximum. The load is then removed, with tip displacement continuing to be recorded. From this data, a load-displacement curve is obtained (Figure 3.6). Analysis of the load-displacements curves using the methodology laid out by Oliver & Pharr [110] allows for the determination of hardness (H) and Young's Modulus (E) of the tested coating. 50 indentations were performed for each sample, with loads ranging from 0.1 to 9.0 mN. To avoid influence of the substrate, a minimum film thickness of 200 nm was used for films tested by nanoindentation.

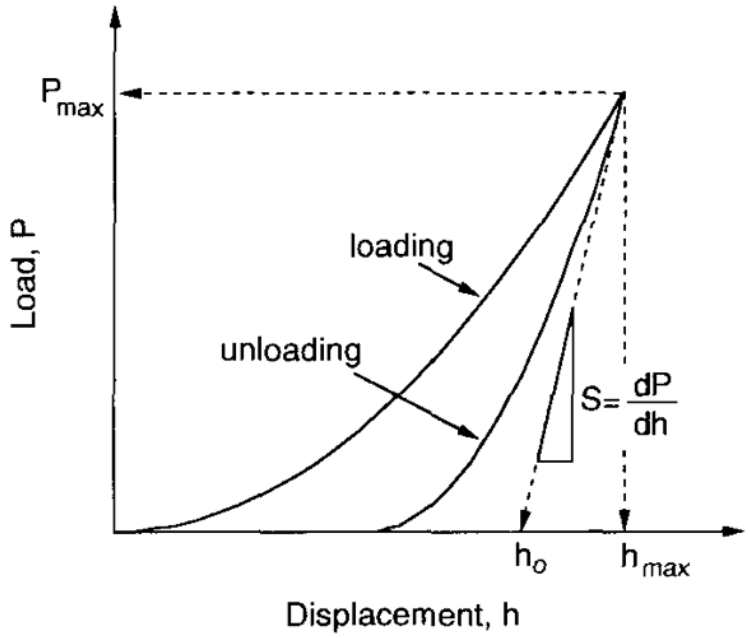

Figure 3.6 Load-displacement curve. Taken from [110].

3.2.6 X-ray photoelectron spectroscopy

X-ray photoelectron spectroscopy (XPS) measurements were used to determine the chemical composition of our samples before and after cycling in an icing wind tunnel. XPS measurements are performed in ultra-high vacuum (~10^{-9} Torr), where a sample is irradiated with X-rays. Photoelectrons are emitted from the surface with a kinetic energy related to the type of X-ray used and the binding energy (BE) of the electron prior to irradiation. Photoelectrons are captured, and the number of electrons detected are determined for each BE value. From this, the concentration of different elements can be determined. Using a high-resolution scan, individual compounds can

be identified. The system used was a VG Scientific ESCALAB 3 MKII, and both survey and high-resolution scans were performed. The measurement depth is <10 nm from the sample surface.

3.3 Icephobicity & Durability tests

3.3.1 Icing/Deicing cycles

Icing/deicing durability tests were performed in a small-scale icing wind tunnel at Concordia University's Multiphase Flow Laboratory, shown in Figure 3.7. An icing wind tunnel is a wind tunnel which has been equipped with a cooling section, as well as an atomizing nozzle that allows a spray of microscale water droplets to be sent towards a test section. This effectively creates an icing cloud inside of the wind tunnel and is highly advantageous compared to other icing techniques seen in the literature, as it allows for the recreation of the icing mechanism seen in real flights. The median volume diameter (MVD) is determined by the nozzle itself, and the liquid water content can be controlled by changing the water and air flow into the nozzle. Temperature is measured by thermocouples in the test section, as well as downwind from it.

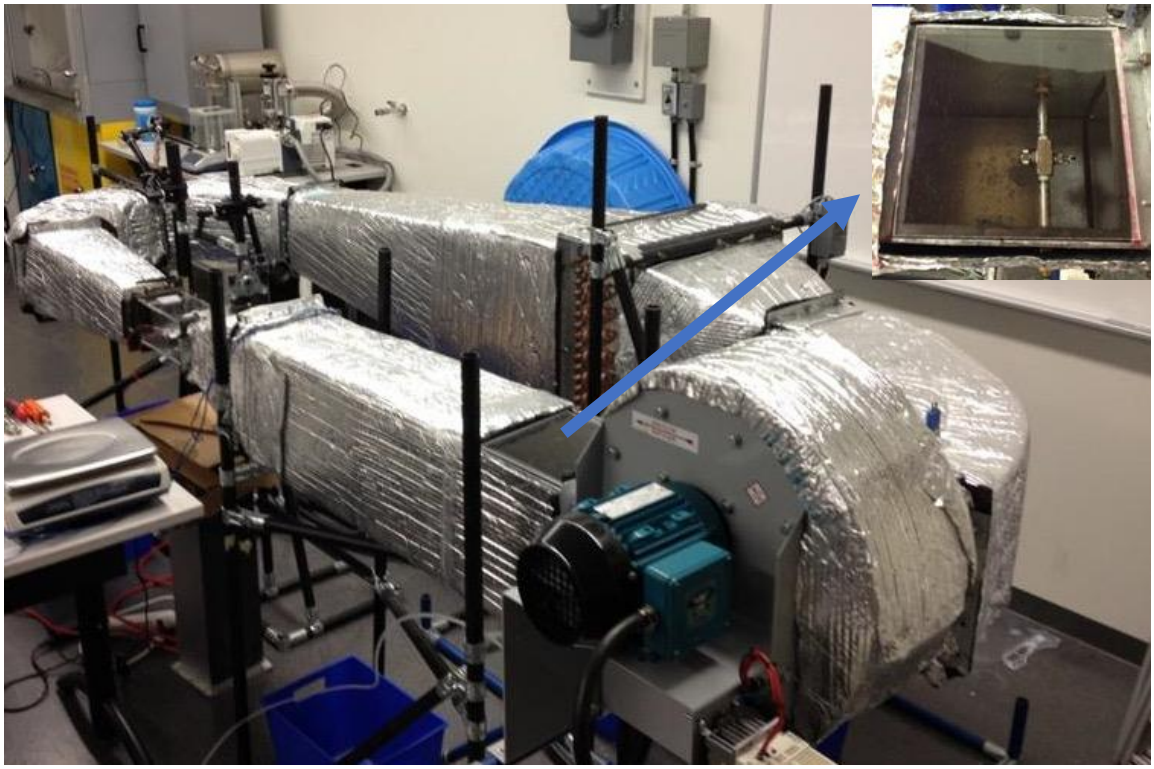

Figure 3.7: The icing wind tunnel at Concordia University. Inlay shows the nozzle. Adapted from [111].

Durability testing was performed over several icing/deicing cycles. The icing conditions can be seen in Table 3.1 and one cycle was defined follows:

1. Sample is iced for 1 minute.
2. Sample is removed from the icing wind tunnel.
3. Ice is melted with a heat gun.
4. Sample is dried under a flow of compressed air.
5. Repeat.

Samples were tested three at a time, and their positions on the sample holder were rotated to account for non-uniformity of the flow in the test section. Contact angle and contact angle hysteresis were measured every 20 cycles, or every 5 cycles for low-durability surfaces. When a single droplet remained pinned to the surface after a hysteresis measurement, this was defined as a partial coating failure, and when all droplets were pinned, this constituted a complete coating failure. Hysteresis measurements were stopped if all droplets were pinned to the surface.

Table 3.1: Icing conditions for icing/deicing cycling.

Ice type	Temperature (°C)	Airspeed (m/s)	LWC (g/m^3)	MVD (μm)
Glaze	-10	43	0.5	30

3.3.2 Ice adhesion

Ice adhesion tests were performed in a small-scale wind tunnel at Airbus Defence & Space. Samples were prepared for ice adhesion tests by depositing the desired coating on a 125 mm × 13 mm × 1.6 mm stainless steel cantilever. A sample first has a strain gauge mounted to its rear side, and then is then in placed inside the IWT test section with the coated surface perpendicular to the oncoming flow. The sample holder is outside the test section and mounted to an electromagnetic shaker mechanically fixed to the outside of the test section.

Ice is then accreted on the sample surface, until reaching a thickness of ~10 mm, after which the IWT's cooling system and fan are shut down. The electromagnetic shaker then begins its linear

motion at 40 Hz, which moves the fixed end of the cantilever. Acceleration of the shaker is increased until a target value is reached, at which point the frequency of vibration is swept from 40 to 90 Hz. As the system approaches its first natural frequency, the maximum displacement of the free end of the beam increases. Once the beam deflection is large enough, a crack forms at the surface-ice interface, near the fixed end of the cantilever. This crack propagates along the interface with every oscillation until full or partial ice detachment is seen.

The moment of the first interfacial crack appears in the strain gauge data as a noticeable jump in both positive and negative strain values, and the average of 5 strain local maxima and minima is used as the strain at failure. That strain value is then used as an input into a model based on the Euler-Bernoulli beam theory, and results in a value for interfacial shear stress. This test was performed with rime, mixed/rime, mixed/glaze, and glaze ice.

3.3.3 Rain erosion

Rain erosion tests were performed by using a pulsating jet erosion test (PJET) rig at Airbus Defence & Space. The principle of a PJET system can be seen in Figure 3.8. A focused water jet is shot out of a nozzle until it reaches a rotating disk with two sections cut out of it. This has the effect of cutting the water jet into smaller segments, which then impact the sample being tested. An increasing number of impacts is performed to see how the sample degrades.

Tests were performed at water jet segment velocities of 165 – 225 m/s, and 20 - 6000 impacts were performed at each velocity. The test pattern used for the droplet impacts can be seen in Figure 3.8. After the rain erosion tests were performed, samples were suspended from a support, and a beaker of deionized water was raised to the sample until it was submerged. The beaker was then removed from the sample, and a picture was taken. For each velocity, the number of impacts at which any amount of water stuck to the surfaces was recorded, and this value was taken as the number of impacts required for a change in surface wettability.

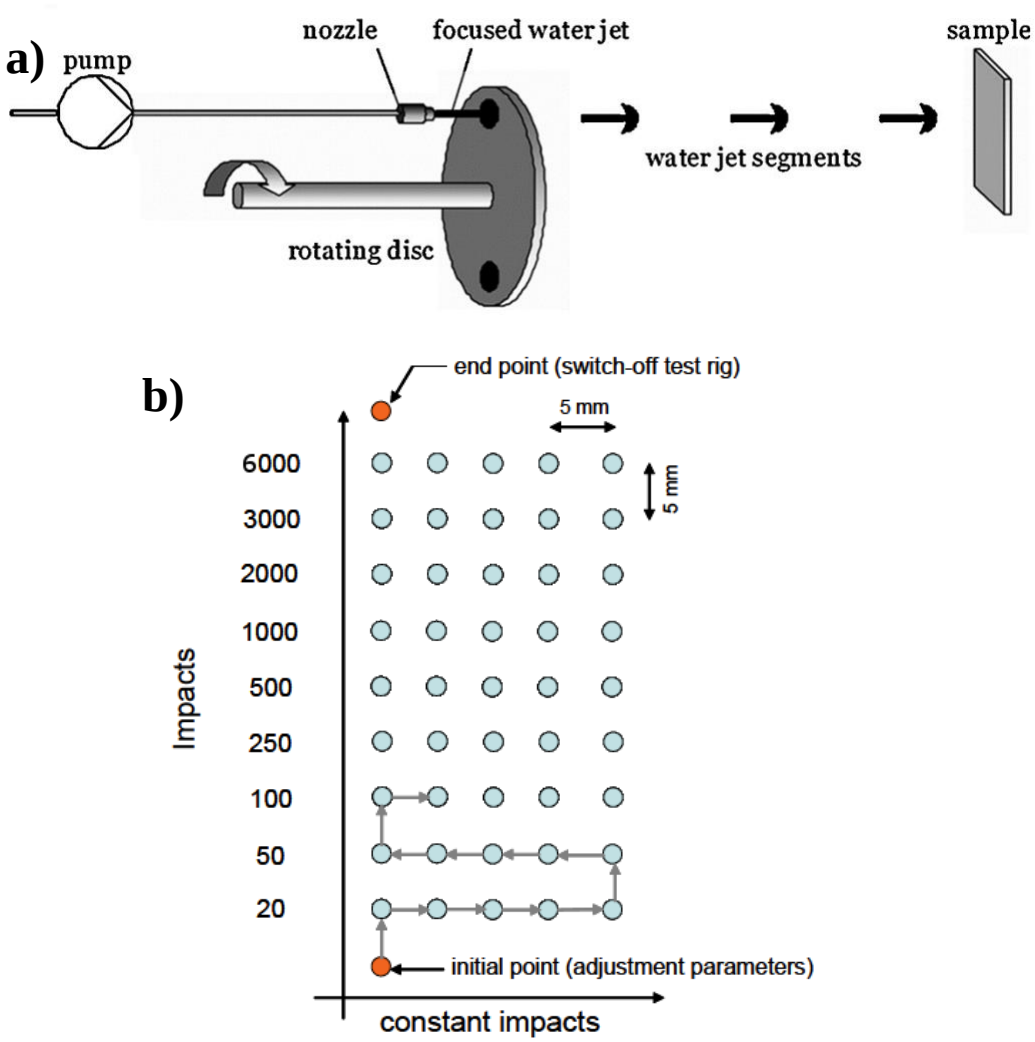

Figure 3.8: a) Focused water jet cut into segments by rotating disk. b) pattern used for number of impacts. Adapted from [112].

CHAPTER 4 DEVELOPMENT AND TESTING OF DURABLE ICEPHOBIC COATINGS

This chapter presents the thin-on-thick coating systems developed, and the results of their testing for icephobicity and durability. It begins with a discussion of plasma-polymerized HMDSO, deposited on flat surfaces with the goal of obtaining the highest contact angles possible. It then moves into the combination of HMDSO with DLC films, in order to obtain hard and hydrophobic DLC:SiO_x films. The challenges of optimizing these films as well as their down-selection for application will be discussed. We then look at the development of a thin-on-thick coating system by depositing the DLC:SiO_x films on hierarchically rough SPS TiO_2 coatings provided by researchers at Concordia University, and the optimizations which took place to achieve robust superhydrophobic surfaces. Finally, the results of ice adhesion tests to confirm the icephobicity of the samples, as well as durability tests via rain erosion and repeated icing/deicing cycles, are presented and discussed.

4.1 Plasma-polymerized HMDSO

We began our development of icephobic coatings by looking at plasma-polymerized hexamethyldisiloxane (PP-HMDSO). Films were deposited on glass microscope slides, on both a biased and grounded electrode in a PECVD system. During the depositions, chamber pressure, substrate bias, and HMDSO flow were modified in order to see their effect on the contact angle, deposition rate, and hardness of the films. Of these, the contact angle was deemed to be the most important parameter. Before film deposition, samples were pre-cleaned with an argon plasma for 10 minutes at -600 V and a pressure of 50 mTorr.

4.1.1 Effect of bias

Initial experiments were performed to test the effect of bias on the wettability of the PP-HMDSO films, and to see the maximum contact angle which could be obtained. Concerning the conditions used, the reader is reminded that the flow rate values for HMDSO will be presented in mTorr, indicating the partial pressure of the HMDSO vapor in the chamber. These tests were performed using 0.8 mTorr of HMDSO, and a working pressure of 150 mTorr. Bias was varied from -250 V to -25 V, however films quickly delaminated at voltages greater than -175V. The lower limit

of -25 V corresponds to the lowest power input which would give a stable bias. The contact angles for these coatings as a function of bias can be seen Figure 4.1.

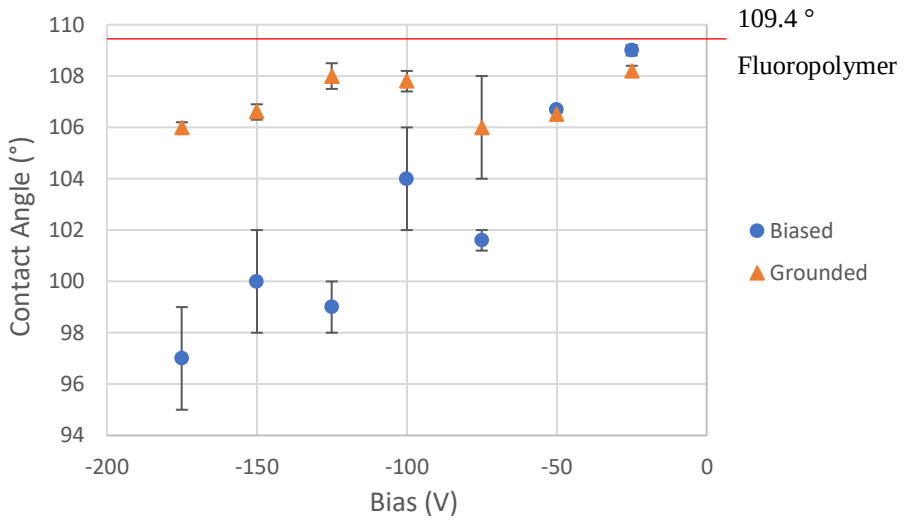

Figure 4.1: Contact angle of grounded and biased samples as a function of electrode bias. The red line indicates the 109.4° value obtained for a fluoropolymer coating.

Looking at the contact angles of the surfaces, we see that samples on the grounded electrode show a value of ~107, regardless of the bias used. Samples on the biased electrode, however, show a clear decrease in contact angle with increasing bias. The most hydrophobic samples obtained were those on the biased electrode at -25 V, which had a contact angle of 109.0 ± 0.2 °, within uncertainty of that seen for OF 110 fluoropolymers deposited by thermal evaporation (109.4 ± 0.4 °).

Changes in bias also caused a change to the deposition rate of the films, as seen in Figure 4.2.

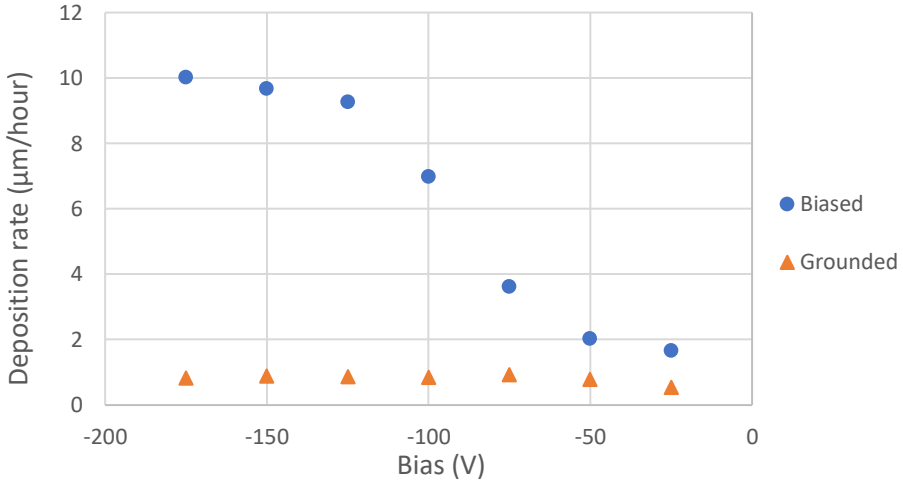

Figure 4.2: Deposition rate of grounded and biased samples as a function of electrode bias.

While the grounded samples are quite consistent around 0.8 µm/hour (with a drop to 0.5 µm/hour at -25 V), the deposition rate of the biased samples shows a slight decrease when dropping from -175 V to -125 V, a large decrease from -125 V to -50 V, and another small decrease from -50 V to -25V. Even at -25 V, however, the deposition rate of 1.65 µm/hour is two times greater than the deposition rates seen for the grounded samples. While it's not surprising to see that changes is bias result in large changes to both the contact angle and deposition rate for samples on the biased electrode, it is interesting to see that the added energy in the chamber has almost no effect on either CA or deposition rate for the grounded samples.

4.1.2 Effects of pressure and HMDSO flow

Having achieved the desired contact angle for our pp-HMDSO coatings, we began to optimize by looking at the effects of pressure and HMDSO flow on the coatings. Beginning with the HMDSO flow, the chamber pressure was set to 150 mTorr and the bias to -25 V, while the HMDSO partial pressure was varied from 0.5 to 2.5 mTorr. Figure 4.3 shows the effect of these changes. Changes to the contact angle are not extreme in any case, though it is worth noting that the grounded results always fall below the biased (though in some cases the difference is negligible), and the highest CA is still that for 0.8 mTorr. In the case of deposition rate, we see that this is relatively low for both biased and grounded samples at 0.5 mTorr HMDSO. These diverge quickly at 0.8 mTorr however, after which they both flatten out. It is likely that at 0.5 mTorr, the rate of film deposition is being limited by the available HMDSO vapor, while somewhere around 0.8 mTorr, the -25 V

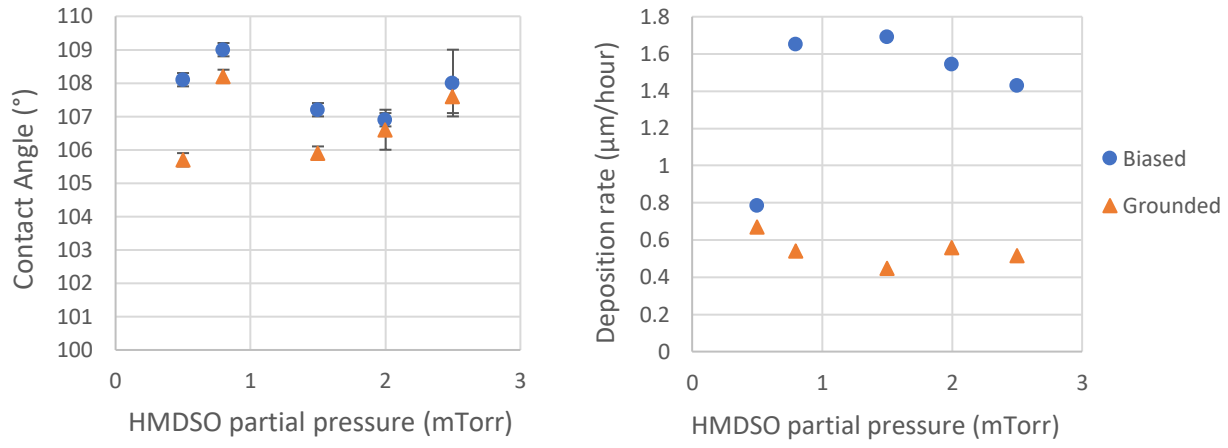

Figure 4.3: Contact angle and deposition rate for biased and grounded samples as a function of HMDSO partial pressure.

becomes the limiting factor.

Tests were next performed to determine the effect of working pressure, holding HMDSO flow constant at 0.8 mTorr and varying bias from -100 to -25 V. Pressures of 100, 150, and 200 mTorr were used, however, high stress in the films deposited at 100 mTorr caused delamination from the surface. As such, it is only the results for 150 mTorr and 200 mTorr which can be seen in Figure 4.4. Here we see that at 200 mTorr, contact angles are slightly higher than at 150 mTorr (though they are within uncertainty) until reaching -25 V, where the 109° result for 150 mTorr is again the highest. Looking at the deposition rate, we see that this is much larger for 150 mTorr at -100 V, through this advantage is drastically reduced by the time -25 V is reached. It is not surprising that the lower working pressure should give a higher deposition rate, as the lower pressure means that there are fewer molecules in the chamber, increasing the mean free path and allowing easier access to the substrate for the precursor ions.

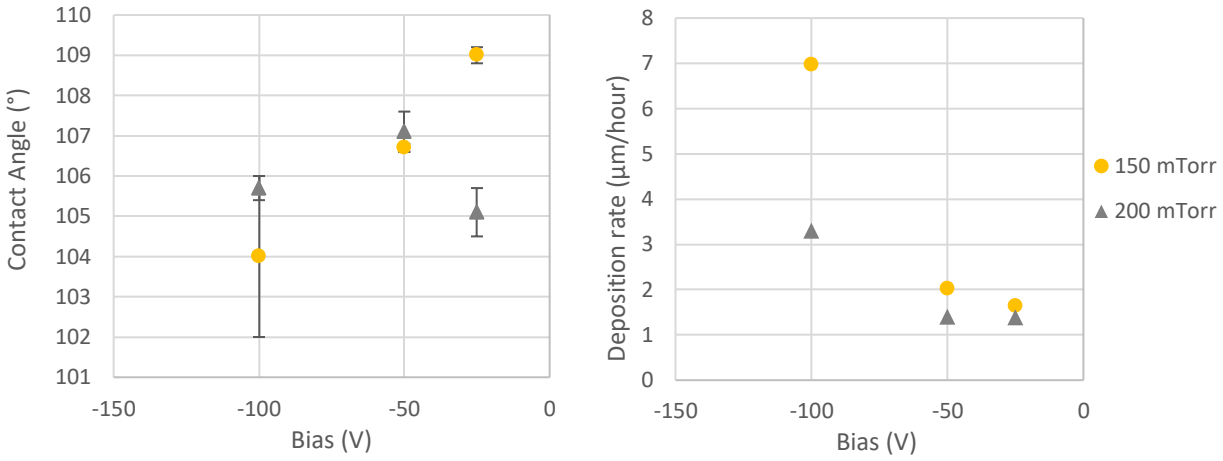

Figure 4.4: Contact angle and deposition rate for 150 and 200 mTorr working pressures as a function of bias.

4.1.3 HMDSO coating summary

After all tests were performed, the highest contact angle was seen for samples deposited at 150 mTorr, with a bias of -25 V, with a HMDSO partial pressure of 0.8 mTorr; this gave a CA value of 109.0 ± 0.2°. While the grounded samples all achieved a similar contact angle to the -25 V biased sample, its superior deposition rate meant that it was selected as the most promising coating. The 109.0 ± 0.2° value is within uncertainty of the results seen for the OF 110 fluoropolymer when

deposited on glass, and very near the limit of 111° achievable for CH_3-based flat surfaces. Following contact angle and deposition rate tests, several coatings were tested by nanoindentation; the hardness values ranged from 0.2 – 0.5 GPa, indicating extremely soft coatings. This low hardness was not entirely unexpected, as we are creating a polymer and the bias used was quite low, however, it did show the need to investigate more robust coatings. For this reason, we began to work on the doping of DLC coatings with HMDSO, to create DLC:SiO_x coatings.

4.2 Development of DLC:SiO_x coatings

Coating development for DLC:SiO_x began with efforts to combine our findings in the coating of PP-HMDSO films with an existing DLC recipe developed for our system. The conditions for this undoped DLC can be found in Table 4.1. These films were again deposited on glass slides placed on biased and grounded electrodes. The biased sample had a hardness on 18 ± 2 GPa and a contact angle of 57.2 ± 0.4°, while the grounded sample had a hardness of 5 ± 0.5 GPa and a contact angle of 73.3 ± 0.4°. Given these results, we would expect that any doped coatings would have a hardness lower than 18 GPa. Additionally, due to the relatively low hardness of even the pure DLC deposited on the grounded electrode, we stopped investigating this technique and began using the biased electrode exclusively. The following sections will explore the effects of different deposition conditions on DLC:SiO_x coatings. These are again deposited on glass slides with the goal of identifying the most promising coatings in terms of wettability and hardness, and those most promising coatings were selected to be deposited on hierarchically rough TiO_2. As before, samples were pre-cleaned with an argon plasma for 10 minutes prior to film deposition, with a bias of - 600 V and at a pressure of 50 mTorr.

Table 4.1: Conditions used for DLC deposition.

Parameter	Value
Precursors	Ar/ C_2H_2
Flow rate	50/5 sccm
Pressure	50 mTorr
Bias	-400 V
Power	33-40 W

4.2.1 Hydrophobic DLC:SiO_x coatings

Similarly to what was done for HMDSO coatings, development of DLC:SiO_x coatings began by looking at the effect of bias on wettability. Depositions were performed with the same conditions listed in Table 4.1, but with the addition of 0.8 mTorr of HMDSO, and varying the bias from -400 V to -140 V (the lowest bias which gave a stable plasma). The results, as well as images of each of these samples can be seen in Figure 4.5. While the sample deposited at -400 V has hardness in the desired 7 – 10 GPa range, all of the samples are hydrophilic, with contact angles below 90 °. This issue is further complicated by the fact that hardness and contact angle are inversely proportional with variation of bias. Looking at the samples themselves, we see that the -400 V sample is a lightly transparent burnt orange. As bias decreases, the samples become more transparent and the orange colour is less pronounced. As was the case with the HMDSO coatings, deposition rates decreased with bias, ranging from 1.59 – 3.51 µm/hour.

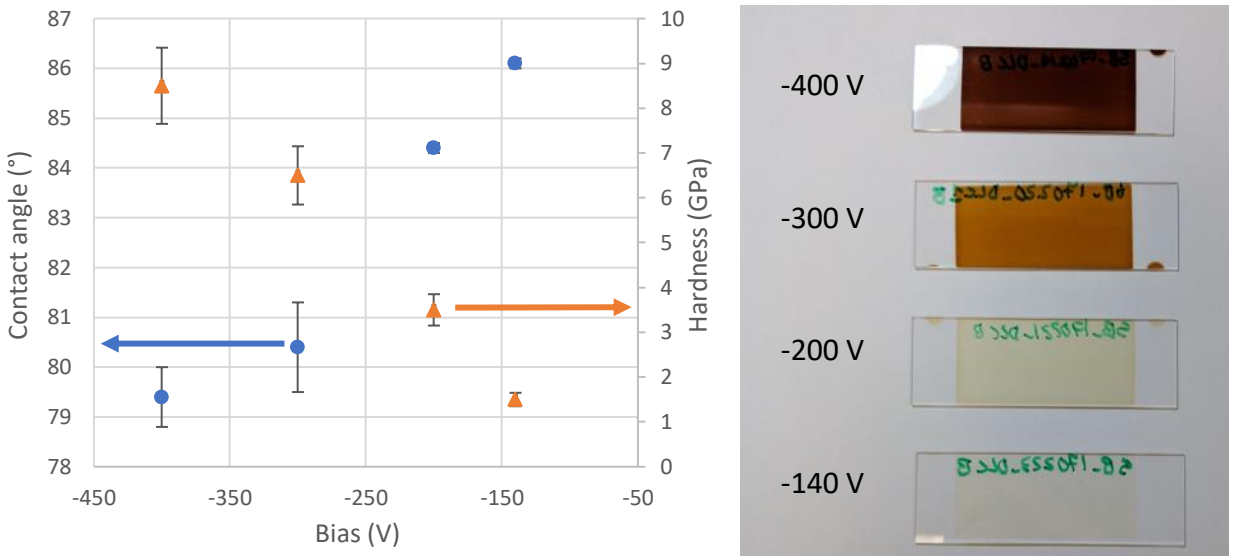

Figure 4.5: Bias vs. contact angle and hardness for DLC:SiO_x samples. Also shown are the deposited films on glass slides.

With the goal of depositing DLC:SiO_x films which were at least hydrophobic, the effects of varying pressure and HMDSO flow were explored. The chamber pressure was increased to 100 mTorr, and the precursors used were 50 sccm Ar, 5 sccm C_2H_2, 0.8 mTorr HMDSO in all cases. Increasing the pressure allowed the minimum bias to be decrease to -100 V, as opposed to the -140 V minimum at 50 mTorr. These results, as well as those for a varying HMDSO flow at 50 mTorr and

-400 V bias are presented in Figure 4.6. While the contact angles for samples deposited at 100 mTorr are lower at comparable bias, the reduction of the minimum bias leads to achieving a DLC:SiO_x film with a contact angle above 90 °. In the HMDSO flow tests, the contact angle increases steadily with increases in HMDSO at -400 V, indicating that we have not hit a saturation point, and further increases to the HMDSO flow may yield even more hydrophobic coatings.

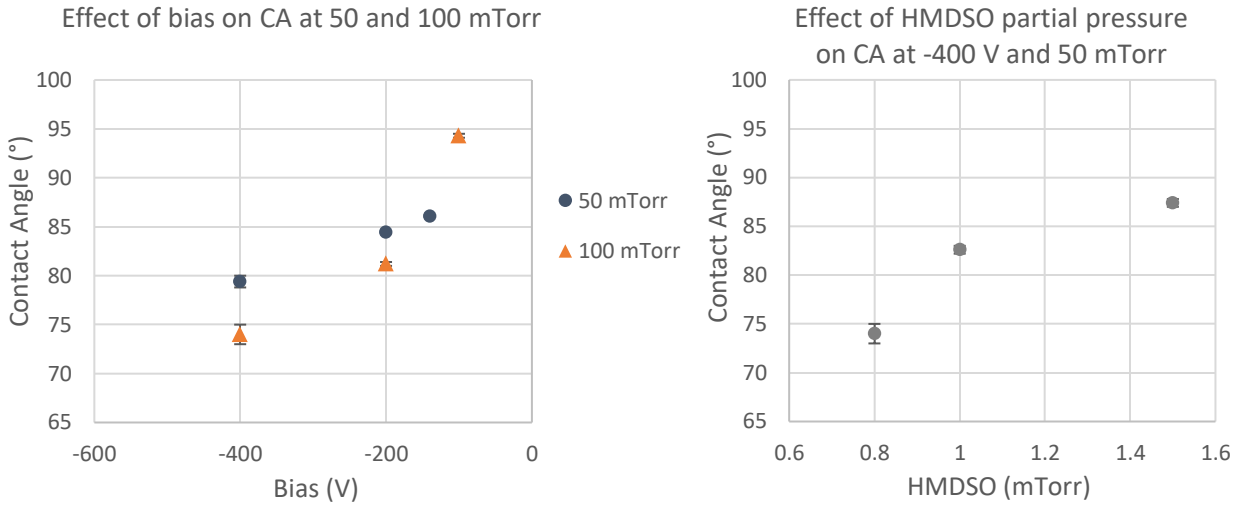

Figure 4.6: Contact angle as a function of bias and HMDSO partial pressure. At working pressure of 50 mTorr was used for the measurements where the HMDSO partial pressure is varied.

Despite obtaining a hydrophobic film using the 100 mTorr/-100 V conditions, the solution of increasing the contact angle via a decrease in bias is not a viable one due to the corresponding decrease in hardness which will occur. From the HMDSO flow tests, however, it has been shown that contact angles can be increased at relatively high bias by increasing the amount of HMDSO in the system. Because of this, we turned our attention to higher bias and higher HMDSO flow for further coating development.

With this idea in mind, new coatings were deposited using biases from -400 to -1000 V, with HMDSO partial pressures 2.0 mTorr to 3.7 mTorr (the highest possible for our system). Argon and C_2H_2 flows were held constant at 50 sccm and 5 sccm respectively for these depositions, whose results at 50 and 100 mTorr can be seen in Figure 4.7

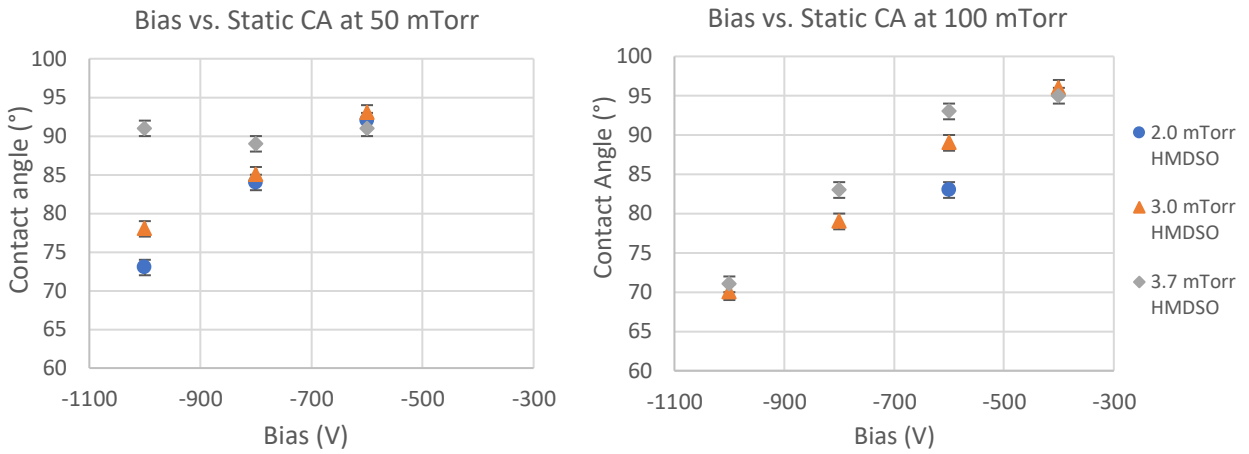

Figure 4.7: Contact angle dependence on bias and HMDSO flow at 50 and 100 mTorr.

At 50 mTorr chamber pressure, we see that the contact angle for samples deposited with a 3.7 mTorr partial pressure sits near 90 ° regardless of bias. At -1000 V, the 3.0 mTorr HMDSO coatings have a greater contact angle than the 2.0 mTorr coating, however, this advantage erodes as the bias moves down to -800 V and -600 V. Notably, all 50 mTorr samples are hydrophobic when deposited at -600V. This is a great improvement over the -100 V bias which was required to deposit a hydrophobic coating with the 0.8 mTorr HMDSO partial pressure. At 100 mTorr chamber pressure, contact angles of the deposited coatings begin at ~70 ° for a bias of -1000 regardless of HMDSO partial pressure, and increase steadily as the bias is decreased. The first hydrophobic coating is seen for 3.7 mTorr HMDSO at -600 V, and moving to -400 V, both the 3.7 and 3.0 mTorr HMDSO coatings have contact angles greater than 95 °. One deposition was performed for 2.0 mTorr HMDSO at 100 mTorr chamber pressure and -600 V bias, however this was not explored further as it gave a contact angle well below the 3.0 and 3.7 mTorr HMDSO coatings, and the general effect of the pressure increase to 100 mTorr was to decrease contact angle at the same bias compared to the 50 mTorr coatings. The combination of these effects meant that the 2.0 mTorr HMDSO coatings would likely not be performant compared to those for higher HMDSO flows.

Finally, inspired by Grischke *et al.* [97], we also wanted to test coatings deposited at lower pressures without argon gas. These coatings were performed at a chamber pressure of 25 mTorr, with a C_2H_2 flow of 5 sccm. HMDSO partial pressure was varied from 2.0 to 3.7 mTorr, and the biases used were -400 V and -600 V, as these are the values which had previously given hydrophobic films.

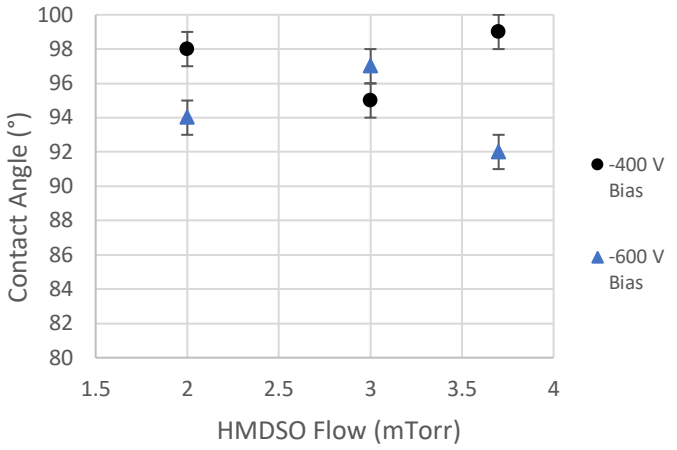

Figure 4.8: Contact angle dependence on bias and HMDSO flow with 5 sccm C_2H_2 at 25 mTorr chamber pressure.

Figure 4.8 shows the results for these 25 mTorr depositions. At a bias of -400 V, contact angles reach 98 ± 1 ° and 99 ± 1 ° for samples deposited at HMDSO partial pressures of 2.0 and 3.7 mTorr, respectively. These are the highest of any DLC:SiO_x films we deposited. All samples deposited at a bias of -600 V were hydrophobic as well, with the highest CA seen for the coating deposited with an HMDSO partial pressure of 3.0 mTorr. Having now developed multiple coatings with contact angles above 90 °, we set out to determine which of these will be used as a thin coating in the final thin-on-thick system.

4.2.2 Properties of final coatings and other remarks

Hardness measurements were performed on selected samples from the coating development section and these results, along with deposition rate, Young's modulus, and contact angle are presented in Table 4.2. Of these, two coatings were chosen for further tests. These are "SB_170508_DLC2" and "SB_170529_DLC1", highlighted in Table 4.2. For the remainder of this work, samples "SB_170508_DLC2" and "SB_170529_DLC1" will be referred to as our "hard" and "balanced" coatings, respectively.

Table 4.2: Properties of several DLC:SiO_x coatings. Samples "SB_170508_DLC2" and "SB_170529_DLC1" were determined to be the most promising.

Sample	Ar (sccm)	C2H2 (sccm)	HMDSO (mTorr)	Pressure (mTorr)	Bias (V)	Deposition Rate (µm/h)	Young's Modulus (GPa)	Hardness (GPa)	CA (°)
SB_170406_DLC	50	5	2	50	-600	7.48	63	**8.7**	**92 ± 1**
SB_170412_DLC3	50	5	3	50	-800	9.92	108	**14.6**	**85 ± 1**
SB_170413_DLC2	50	5	3	50	-1000	9.16	119	**16.1**	**78 ± 1**
SB_170508_DLC1	50	5	3.5	100	-800	13.98	107	**14.3**	**83 ± 1**
SB_170508_DLC2	50	5	3.6	100	-600	15.12	61	**8.5**	**93 ± 1**
SB_170508_DLC3	50	5	3.7	100	-400	13.5	35	**4.8**	**95 ± 1**
SB_170511_DLC1	50	5	3	100	-400	12.72	35	**4.3**	**96 ± 1**
SB_170523_DLC1	30	0	3.4	25	-550	8.46	50	**5.5**	**95 ± 1**
SB_170526_DLC1	0	5	2	25	-400	10.02	28	**3.3**	**98 ± 1**
SB_170529_DLC1	0	5	3	25	-600	14.76	43	**5.4**	**97 ± 1**

Early in the project, we intended to perform depositions directly onto patterned Ti-6Al-4V substrates. Film adhesion of our balanced coating on these substrates, however, was very poor, and the stress induced by a single droplet being placed on the surface for contact angle measurements was enough to cause the coating to delaminate. Because of this, we began to use a SiN_x interlayer with our DLC:SiO_x coatings. This improved the adhesion greatly, as can be seen in Figure 4.9, where the coating delamination can easily be seen for the sample without interlayer. The sample with the interlayer was difficult to photograph due to its dark colour and lack of reflectivity. In

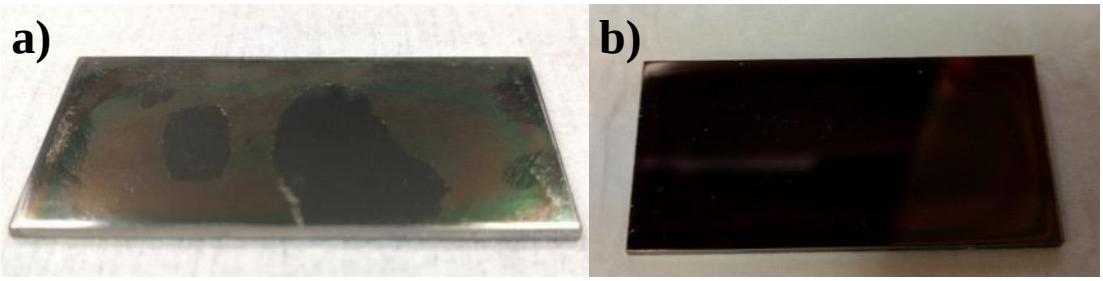

Figure 4.9: DLC:SiO_x coating on Ti-6Al-4V after contact angle measurements. a) Without interlayer, film delaminates easily, b) with interlayer, coating adheres well to the surface.

addition to this improvement in adhesion, the samples deposited with the interlayer showed a marked increase in mechanical properties, with the "balanced" sample's hardness improving from 5.4 ± 0.5 GPa to 8.7 ± 0.8 GPa, and the "hard" from 8.5 ± 0.8 to 11 ± 1 GPa. There was however, also a small corresponding decrease in wettability, changing these to 95 ± 1° and 92 ± 1° for the balanced and hard samples, respectively. Because of the increase in mechanical properties, the SiN_x layer was used with these coatings for all subsequent depositions.

4.3 Deposition on Suspension Plasma Spray TiO_2

The title of this thesis is "DEVELOPMENT OF A DURABLE THIN-ON-THICK ICEPHOBIC COATING SYSTEM FOR AEROSPACE APPLICATIONS" and as such, it is now time to discuss the "thick" portion of this coating system. These are ~50 µm TiO_2 coatings deposited by suspension plasma spray and provided to us by researchers at Concordia University as part of the Phobic2Ice project. Surfaces with hierarchical roughness are obtained by depositing from sub-micron sized TiO_2 powder in an ethanol suspension. The TiO_2 surfaces are extremely hydrophilic on their own, but become superhydrophobic when coated with a hydrophobic topcoat (Figure 4.10).

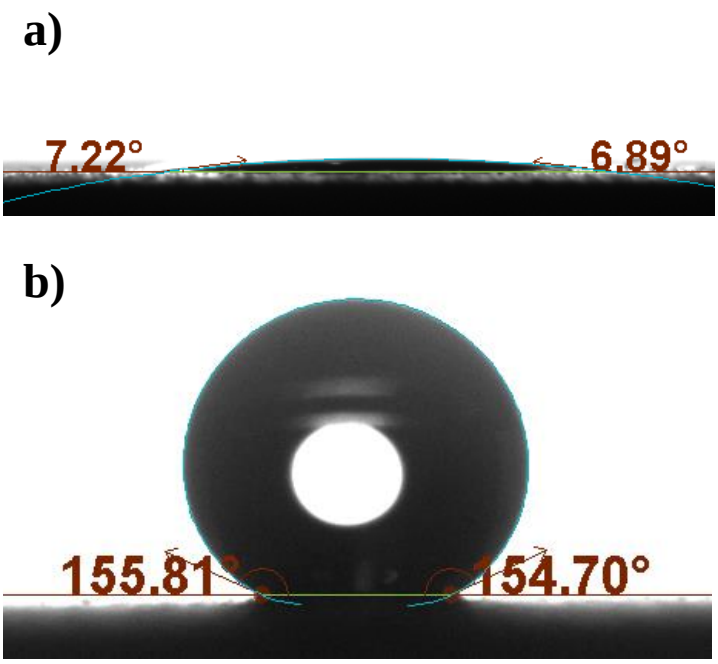

Figure 4.10: SPS TiO_2 a) without and b) with a hydrophobic coating

The roughness properties for a typical SPS TiO_2 surface can be seen in Table 4.3, while a surface profile scan for this sample can be seen in Figure 4.11. The coatings are grown on grit-blasted surfaces to obtain the micro-scale surface features, which causes the patterning to be random, however, the surface roughness shown in Table 4.3 is typical of what was seen. It was communicated to us by researchers at Airbus that any coating to be applied to aircraft components should have an average roughness (S_a) lower than 10 ± 2 µm, as well as a maximum surface feature height (S_z) below 100 ± 10 µm. It can be seen that while the TiO_2 coatings are on the upper end of the acceptable roughness, they do satisfy these requirements.

Table 4.3: Roughness parameters for a SPS TiO_2 surface.

Sample	**S_a**	**S_z**	**S_{sk}**	**S_{ku}**
TiO_2 – no coating	10.5 ± 0.3	81 ± 6	0.48 ± 0.5	2.6 ± 0.1

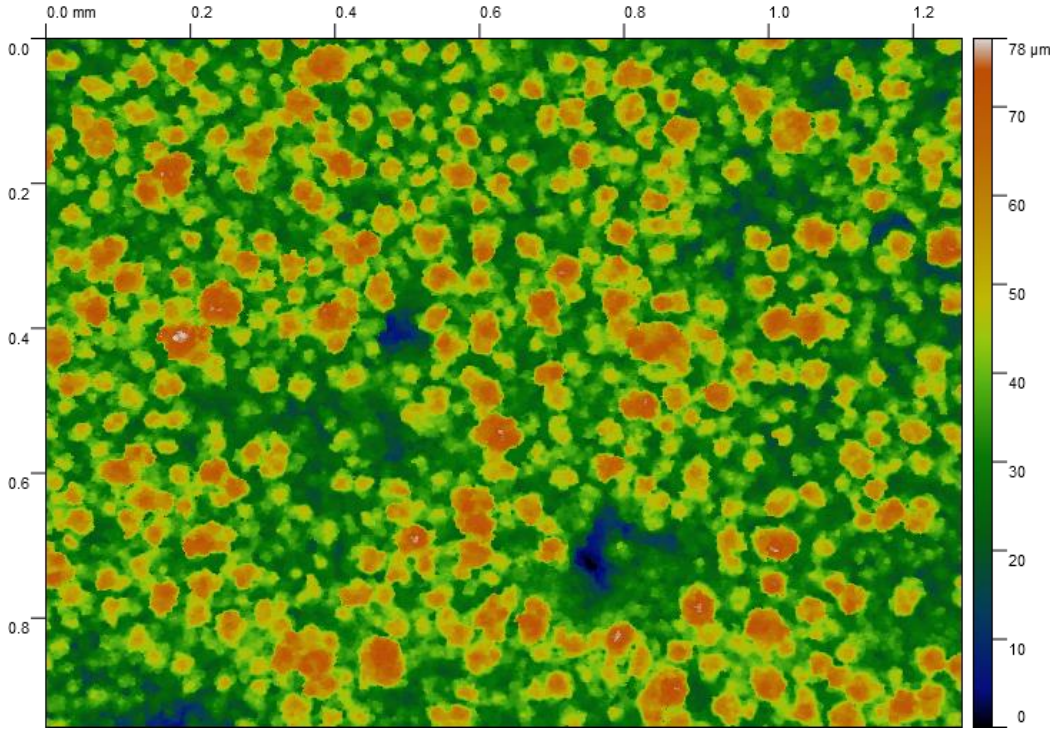

Figure 4.11: Surface profile scan of a non-coated TiO_2 surface at 5x.

The hierarchical roughness of the SPS TiO_2 coatings has been verified by SEM. Figure 4.12 shows a large ~40 µm pillar, which itself shows nanoscale features along its surface. These features must be maintained after coating, and it is for this reason that we next explored the effect of DLC:SiOx coating thickness on surface wettability.

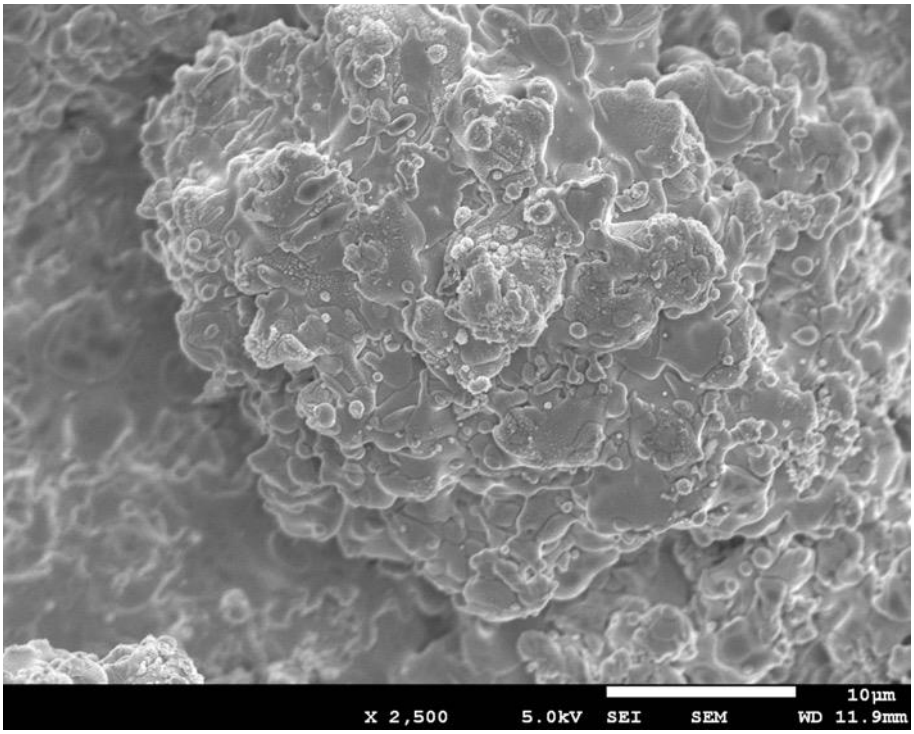

Figure 4.12: Suspension plasma sprayed TiO2 surface, without any topcoat.

4.3.1 Maximum coating thickness

Similar to the earlier case of hardness and contact angle, a compromise must be made when determining an appropriate coating thickness for the "thin" portion of our coating system. For maximum durability, we want to have the thickest coating possible, however, due to the smoothing tendency of the amorphous DLC and SiN_x coatings [96], we must be careful to not go so thick as to lose the nano-scale surface features. Table 4.4 shows the effects of coating thickness on the wettability of the samples. While a total coating thickness of 500 nm gives a superhydrophobic surface, a clear decrease in CA and increase in CAH is seen as we move to thicker coatings. An SEM investigation into the effect of coating thickness on nano-scale surface features, seen in Figure 4.13, confirmed that these were being removed by the thicker coatings. For this reason, all future samples were coated with a maximum thickness of 500 nm.

Table 4.4 : Effect of coating thickness on samples wettability.

Sample	Thickness SiN_x (µm)	Thickness DLC:SiO_x (µm)	Total Thickness (µm)	Contact Angle (°)	Hysteresis (°)	Roll-off Angle (°)
1	0.25	0.25	0.5	168 ± 3	10 ± 2	4.7 ± 0.5
2	0.5	0.5	1.0	160.1 ± 0.9	30 ± 5	9 ± 2
3	0.5	1.5	2.0	152 ± 2	46 ± 3	31 ± 2

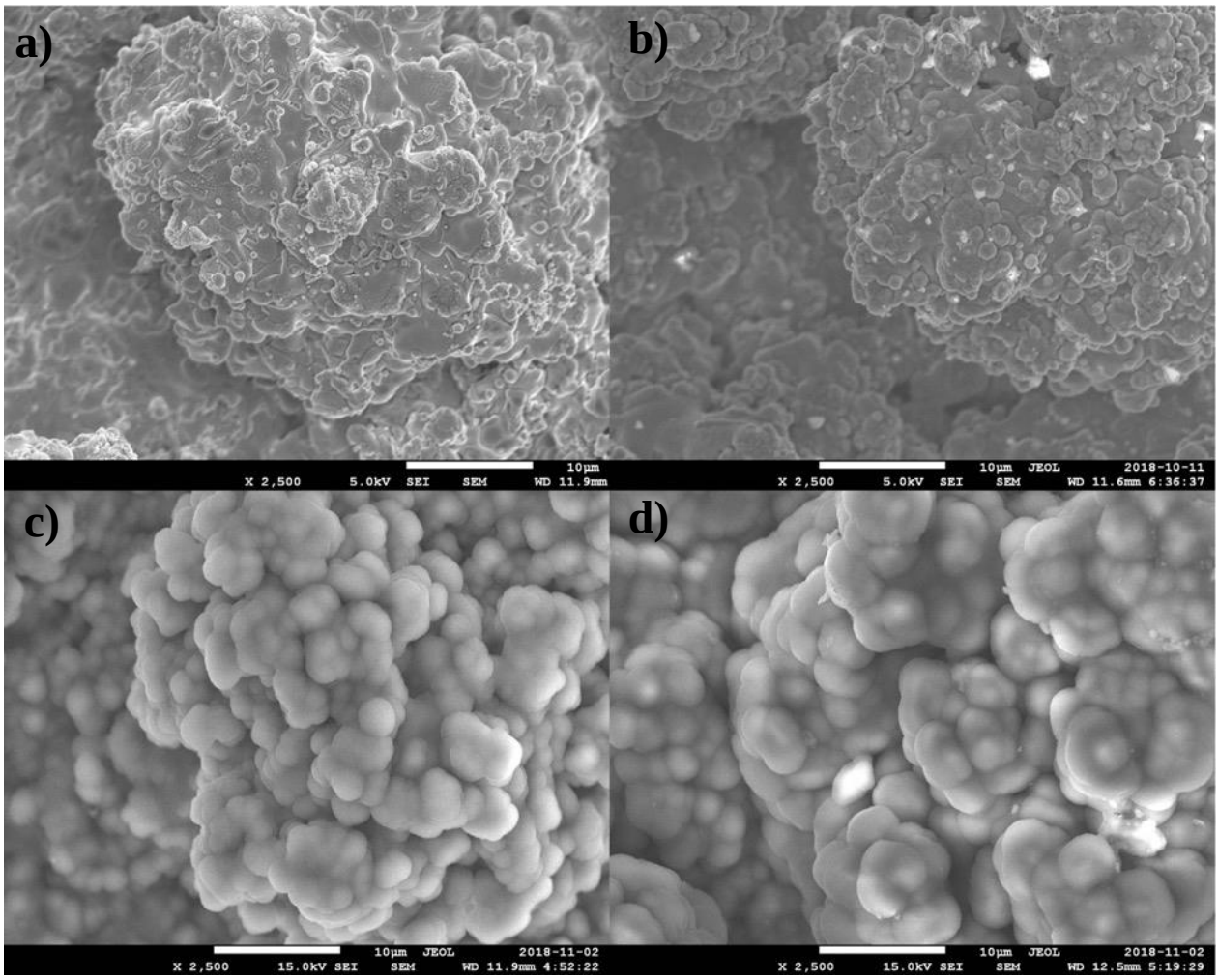

Figure 4.13: SPS TiO_2 a) without coating, b) with 0.5 µm coating, c) with 1 µm coating, and d) with 2 µm coating. The reduction of nanoscale roughness is clear as coatings become thicker.

4.3.2 Deposition of thin-on-thick coating system

The final coating systems selected for use in icephobicity and durability testing consist of the following layers: ~50 µm TiO_2, 150 nm SiN_x, 250 nm DLC:SiO_x, 100 nm HMDSO. Stainless steel 304 was used as the substrate, and a schematic of the layers can be seen in Figure 4.14. Samples were deposited with both our balanced and hard DLC:SiO_x coatings, and the SiN_x/DLC:SiO_x/HMDSO combination will henceforth be referred to as the "balanced stack" or "hard stack" depending on which DLC:SiO_x coating was used. While the coatings have been confirmed to be superhydrophobic without using an HMDSO topcoat, this was added to further improve the water-repellency of the surfaces. Table 4.5 shows contact angle and contact angle hysteresis for SPS TiO_2 coated with HMDSO only, our balanced and hard coatings, and our full SiN_x/DLC:SiO_x/HMDSO balanced and hard stacks. The decrease in contact angle from the results seen in Table 4.4 comes from a variation in the TiO_2 surfaces. Issues with the thermal spray system at Concordia University meant that they could not produce new coatings for several months. Upon repair of the system, samples giving a low CAH after being coated could still be obtained, however, there was a notable drop in the static contact angle measurements.

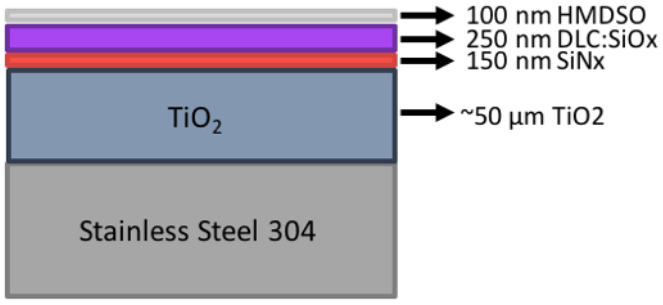

Figure 4.14: Schematic the coating system used for icephobicity and durability testing

Table 4.5: Wettability properties of SPS TiO_2 with different stacks.

Sample	CA (°)	CAH (°)
TiO_2/HMDSO	156.2 ± 0.8	3.3 ± 0.9
TiO_2/Balanced DLC:SiOx	154 ± 1	8 ± 2
TiO_2/Hard DLC:SiOx	153 ± 1	8 ± 2
TiO_2/Balanced stack	155.7 ± 0.6	3.8 ± 0.4
TiO_2/Hard stack	156.3 ± 0.4	6 ± 1

The effect of coatings on the roughness properties of the surfaces was also explored, with optical interferometry measurements performed before and after coating with our balanced stack. The changes due to coating are not statistically significant as can be seen in Table 4.6. While we have previously confirmed the smoothing effect of our coatings, the fact that the roughness from the microscale surface features is so much larger than the contributions from the nanoscale features means that these changes do not appear in the overall roughness measurements. Images of the surface profile before and after coating can be seen in Figure 4.15.

Table 4.6: Surface roughness properties before and after coating.

Sample	S_a	S_z	S_{sk}	S_{ku}
TiO_2 – no coating	10.5 ± 0.3	81 ± 6	0.48 ± 0.05	2.6 ± 0.1
TiO_2 – Balanced stack	10.2 ± 0.3	78 ± 6	0.43 ± 0.04	2.6 ± 0.1

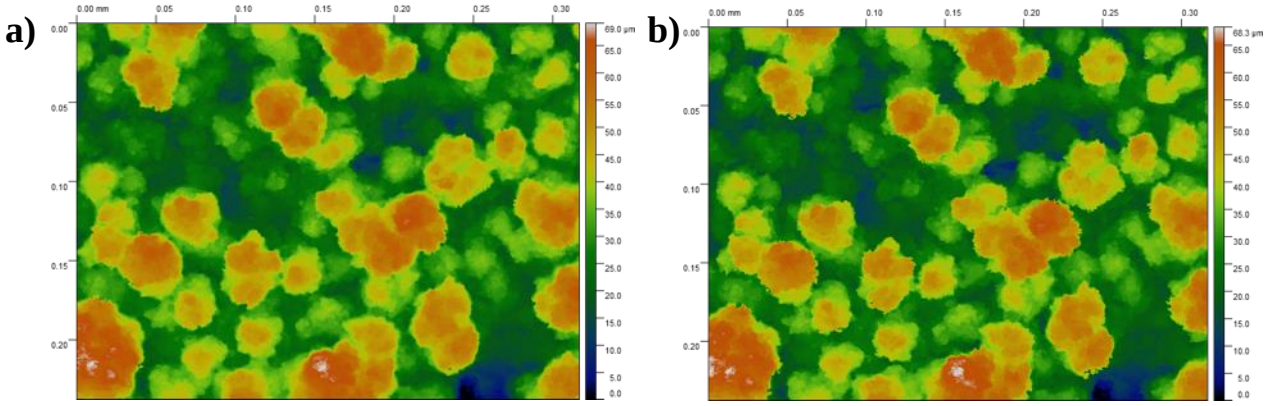

Figure 4.15: Surface profile of TiO_2 at 20x a) before and b) after coating with balanced stack.

4.4 Sample performance in durability and icephobicity testing

Having developed a superhydrophobic coating system, we now aim to show that they are also icephobic, and durable compared to other solutions. To confirm the icephobicity of a superhydrophobic surface, it is critical that ice adhesion tests be performed, as the surface may not be icephobic if the air-ice portion of the interface is too small. Given that the SPS TiO_2 surfaces

used are random, this test is especially important, as the area of this interface is not easily calculated.

This section will present the ice adhesion measurements which were performed, as well as two sets of durability tests: a rain erosion test, and repeated icing/deicing cycles in an icing wind tunnel. In the case of the ice adhesion and rain erosion tests, TiO_2 surfaces coated with our balanced and hard SiN_x/DLC:SiO_x/HMDSO stacks, as well as TiO_2 samples dip-coated in stearic acid, are tested. For the icing/deicing cycles, the samples tested are TiO_2 samples coated with our balanced stack, a SiN_x/HMDSO stack, and stearic acid. Here the hard stack is omitted, as it has been shown that coating hardness does not have a big effect on degradation during this type of cycling. Also tested was NeverWet™, a commercially available superhydrophobic spray coating from Rust-Oleum®.

4.4.1 Ice adhesion

Ice adhesion tests were performed by researchers at Airbus Defence & Space on SPS TiO_2 samples with our hard and balanced stacks, as well as on a SPS TiO_2 sample coated with stearic acid. Four types of ice were grown on the samples in an icing wind tunnel; the icing conditions for each ice type can be found in Table 4.7 and images of each ice type can be seen in Figure 4.16.

Table 4.7: Icing conditions for ice adhesion tests.

Ice type	Temperature (°C)	Airspeed (m/s)	LWC (g/m^3)	MVD (µm)
Rime	-20	50	0.3	20
Mixed / Rime	-20	50	0.8	20
Mixed / Glaze	-5	50	0.3	20
Glaze	-5	80	1.0	20

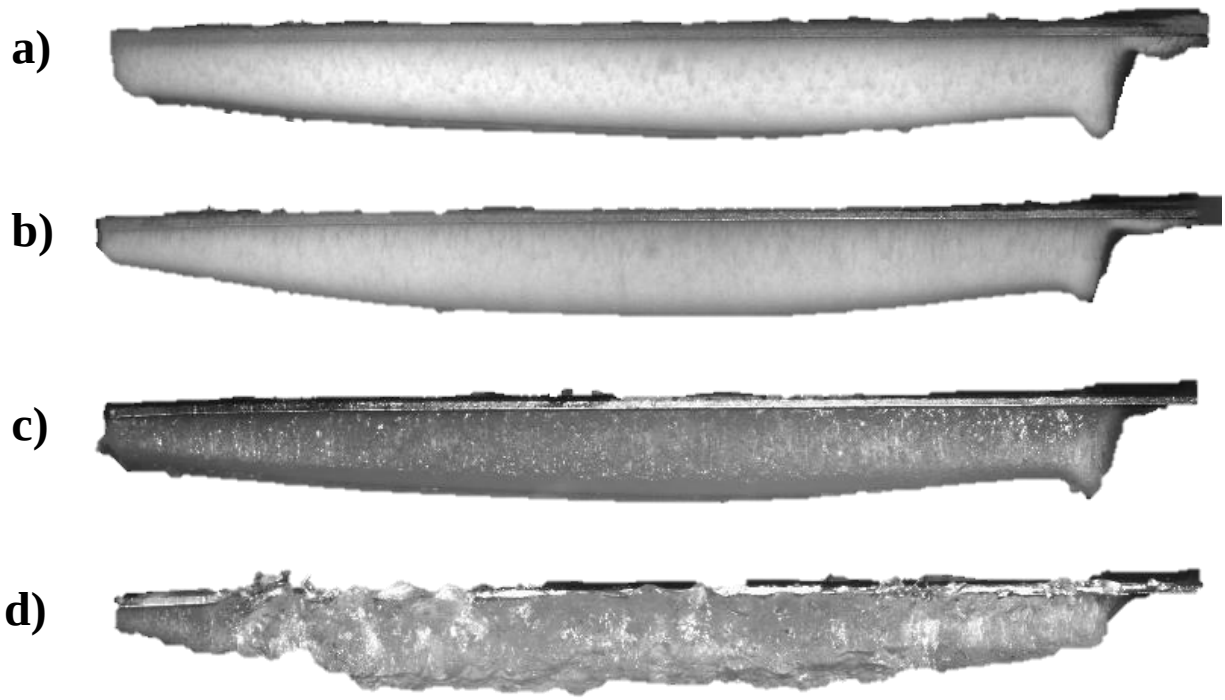

Figure 4.16: Iced surfaces showing a) rime b) mixed/rime c) mixed glaze and d) glaze ice obtained in the Airbus icing wind tunnel.

The results of the ice adhesion tests can be found in Table 4.8. It is shown that the balanced stack is icephobic for every type of ice and is especially performant for the Mixed/Glaze. The opposite is true for the hard stack; it outperforms the balanced stack in all conditions except the Mixed/Glaze ice, where an enormous increase in ice adhesion is seen. While it is not uncommon for ice adhesion to vary across ice types, the exact reason for this increase is unknown at this time. Finally, the stearic acid coating performed well, with ice adhesion strength steady around 80 kPa, except when testing glaze ice, where it performed very well, giving the best result of all coating/ice combinations at 58 ± 4 kPa. The similar values for the balanced stack and stearic acid should not be surprising, as they have very similar wetting properties and are deposited on the same TiO_2 coating.

Table 4.8: Ice adhesion for balanced, hard, and stearic acid coatings in 4 different icing conditions.

Sample	Condition	Ice adhesion value (kPa)	Average ice adhesion (kPa)
Balanced	Rime	83 ± 5	80 ± 7
Balanced	Mixed/Rime	84 ± 3	
Balanced	Mixed/Glaze	62 ± 27	
Balanced	Glaze	90 ± 3	
Hard	Rime	82 ± 2	114 ± 40
Hard	Mixed/Rime	71 ± 8	
Hard	Mixed/Glaze	229 ± 104	
Hard	Glaze	75 ± 13	
Stearic Acid	Rime	88 ± 5	76 ± 8
Stearic Acid	Mixed/Rime	74 ± 5	
Stearic Acid	Mixed/Glaze	82 ± 7	
Stearic Acid	Glaze	58 ± 4	

4.4.2 Rain erosion

Rain erosion tests were performed by researchers at Airbus Defence & Space on SPS TiO_2 samples with our hard and balanced coatings, as well as on a SPS TiO_2 sample coated with stearic acid. Tests were performed at droplet velocities of 165 m/s, 180 m/s, 200 m/s, and 225 m/s; at each velocity, 5 tests were performed for 20, 50, 100, 250, 500, 1000, 2000, 3000, and 6000 droplet impacts. Figure 4.17 shows the samples after testing, while Table 4.9 lists the number of impacts required for the coating failure of each sample at all four droplet velocities.

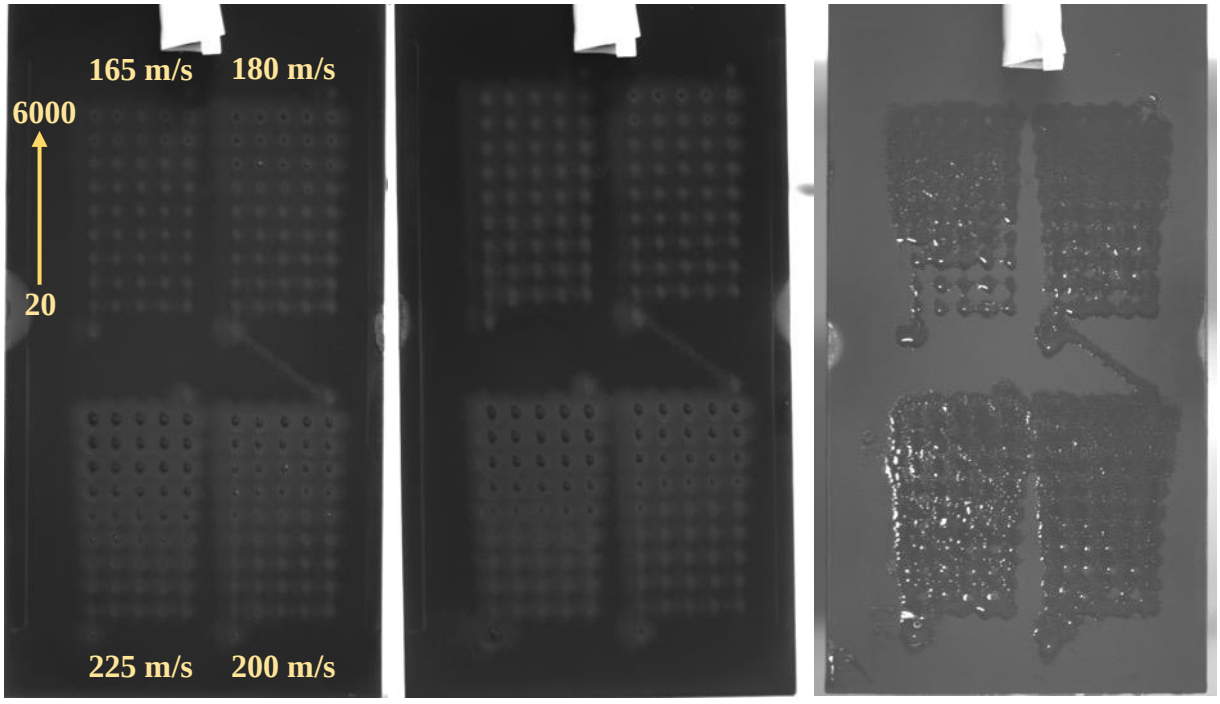

Figure 4.17: a) balanced stack b) hard stack and c) stearic acid samples after rain erosion tests and dipping samples into deionized water. Droplet velocities are 165, 180, 200, and 225 m/s, moving clockwise from the top left. Impacts are in rows of five, for 20, 50, 100, 250, 500, 1000, 2000, 3000, and 6000 impacts, from the bottom of each group.

Table 4.9: Number of droplet impacts required for water to adhere to surface for all samples and droplet velocities.

Sample	Droplet velocity (m/s)	Impacts to coating failure
Balanced	165	3000
Balanced	180	1000
Balanced	200	500
Balanced	225	100
Hard	165	>6000
Hard	180	2000
Hard	200	500
Hard	225	250
Stearic Acid	165	20
Stearic Acid	180	20
Stearic Acid	200	20
Stearic Acid	225	20

The superior durability of the balanced and hard stacks is clearly seen in this test; the stearic acid samples failed completely after only 20 droplet impacts for every droplet velocity. Also clear from these results is the measurable advantage of our hard stack over the balanced stack for such a durability test. With the exception of the 200 m/s test, where both failed after 500 impacts, the hard stack typically required twice as many impacts to reach a failure point. Even in the case of failure of our coatings, the damage is well-contained to the point of impact. The stearic acid samples, on the other hand, show a clear spreading of droplets across test sites after 100 impacts at 165 m/s, and the degradation only worsens as number of impacts and water speed increase.

4.4.3 Durability in icing/de-icing cycle tests

The final durability test consists of icing/deicing cycles in an icing wind tunnel. Samples were iced for one minute at the conditions listed in Table 4.10, which produced a layer of glaze ice on the surface. Samples were then removed, and ice was melted with a heat gun, after which samples were dried under a compressed air flow. Contact angle and contact angle hysteresis were measured every 20 cycles, or more often for less durable samples. SPS TiO_2 coated with our balanced stack, stearic acid, and a softer 500 nm SiN_x/HMDSO stack (150 nm SiN_x, 350 nm HMDSO) were tested, as well as NeverWet superhydrophobic coating sprayed on polished stainless steel.

Table 4.10: Icing Wind Tunnel conditions for icing/deicing cycles

Ice type	Temperature (°C)	Airspeed (m/s)	LWC (g/m^3)	MVD (µm)
Glaze	-10	43	0.5	30

The coated TiO_2 samples can be seen in Figure 4.18, and the samples mounted in the icing wind tunnel before and after icing can be seen in Figure 4.19. It is visible from the iced samples that the droplet flow in test section is not perfectly uniform, and sample position in the IWT was rotated with every cycle to counter this.

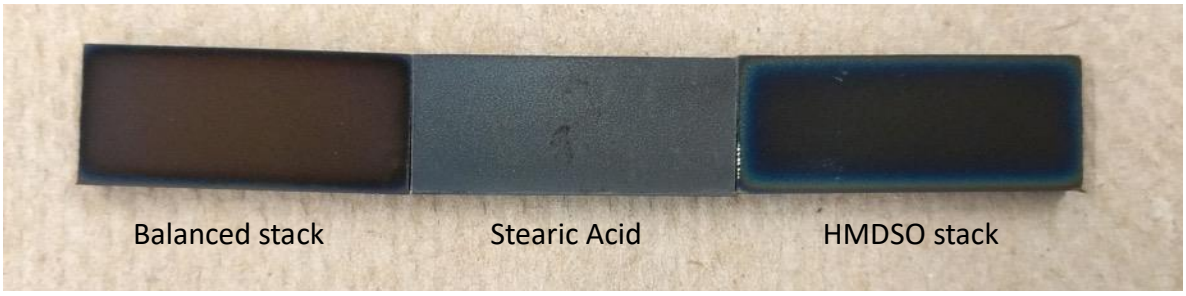

Figure 4.18: Balanced stack, stearic acid, and HMDSO stack TiO_2 samples used for icing/deicing cycling.

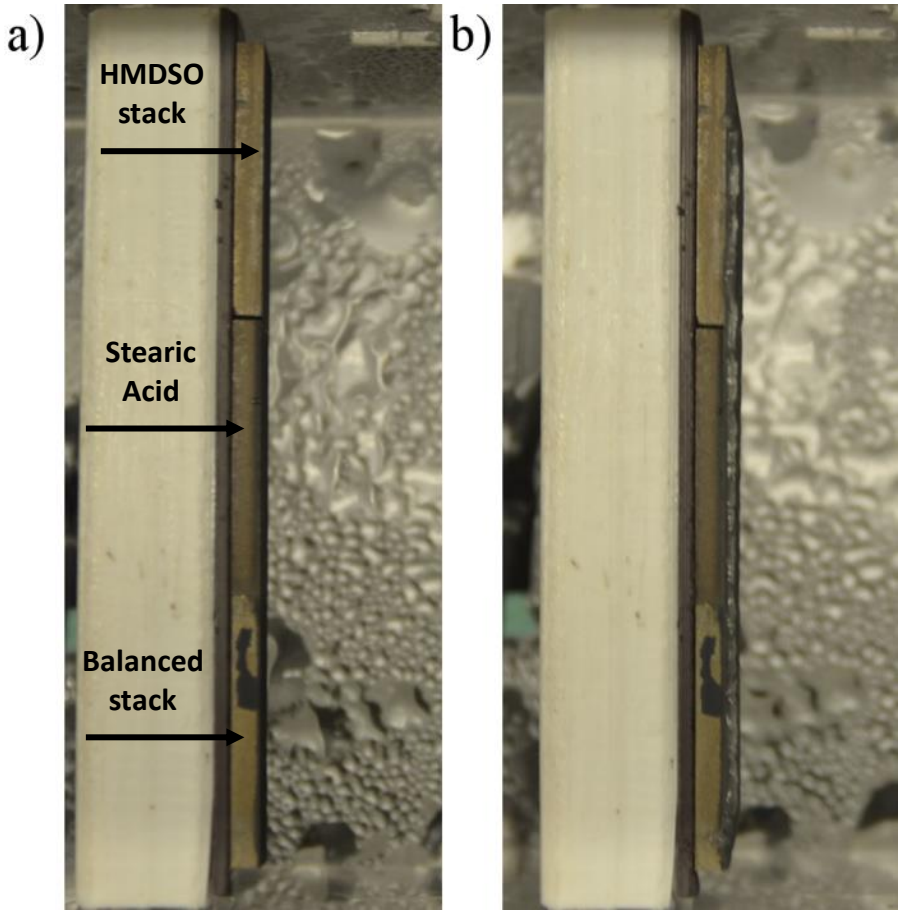

Figure 4.19: SPS TiO_2 samples installed in IWT a) before and b) after 1 minute of icing

Contact angle and contact angle hysteresis results over as many as 170 cycles can be seen in Figure 4.20. As hysteresis was being measured by the droplet inflation/deflation method, it was possible for droplets to stick to the surface during deflation, rather than being drawn back into the dispenser needle. The point at which one droplet first stuck to the surface during CAH measurements, indicating partial coating failure, or all droplets stuck to the surface, indicating complete coating failure, can be seen in Table 4.11.

Looking at the results, we see first the quick degradation of the NeverWet coating. Contact angle drops consistently as cycles are performed, while the CAH increases almost constantly, with the first droplet sticking to the surface after 15 cycles, and all droplets sticking after 20 cycles. At this point, the surface has failed completely and no further cycling was performed.

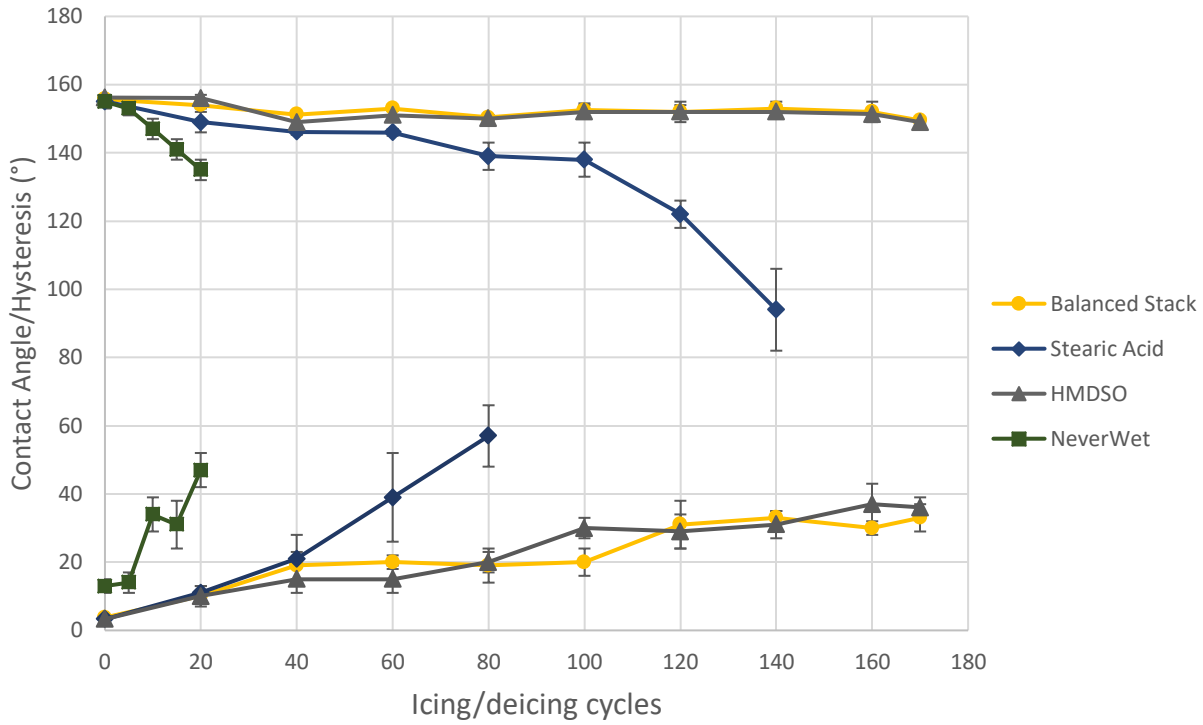

Figure 4.20: Contact angle (top) and contact angle hysteresis (bottom) for tested samples after up to 170 icing/deicing cycles.

Table 4.11: Cycles required for one or all droplets to stick to sample surface during contact angle hysteresis measurements.

Sample Type	Cycles total	Cycles until 1 drop sticks	Cycles until all drops stick
Neverwet	20	15	20
Stearic Acid	140	40	70
HMDSO	170	70	N/A
Balanced Stack	170	N/A	N/A

The stearic acid sample performs similarly to the balanced and HMDSO stacks up to 40 cycles, however, the larger uncertainty for the stearic acid coating at 40 cycles is worth noting. Generally, for CAH measurements during degradation, a large uncertainty corresponds with one CAH

measurement giving a much higher value than the others. This is indeed the case at 40 cycles; Table 4.11 shows this as the point at which a droplet first stuck to the surface during CAH measurements. After 40 cycles, the CAH values diverge from those seen for the balanced stack and HMDSO samples, with all droplets sticking to the surface after 70 measurements. CAH measurements were stopped for the stearic acid sample after 80 measurements as the surface was completely damaged by this point. Looking at the contact angle measurements for the stearic acid sample, we see that degradation is slow but steady up to 100 cycles, dropping from 155.1 ± 0.5 ° to 138 ± 5 °. After this the sample degrades more rapidly, reaching a value of 94 ± 12 at 140 cycles before measurements were stopped (samples were still cycled a full 170 cycles times).

The balanced and HMDSO stacks perform very similarly to one another, with the balanced stack finishing 170 cycles with a contact angle of 149.5 ± 0.9 ° and a hysteresis of 33 ± 4 °, and the HMDSO stack finishing with values of 149 ± 1 ° and a hysteresis of 36 ± 3 ° for the CA and CAH, respectively. Because of the similar values throughout cycling, it is likely that the HMDSO layer on the DLC:SiO_x sample has not been removed, and what we're seeing is the degradation of this layer while the DLC:SiO_x layer underneath remains untouched. One difference between the two stacks is that the HMDSO stack did have some water stick to the surface after 70 cycles. The behaviour seen here was distinct from that seen for the stearic acid sample, as can be seen in Figure 4.21. At 70 cycles, it is only a trace amount of water which remains, and even after 170 cycles the droplet which remains is much smaller than that seen for the stearic acid sample. Additionally, unlike the stearic acid sample, this was the only spot on the surface to be damaged during cycling; at no point did drops placed elsewhere stick.

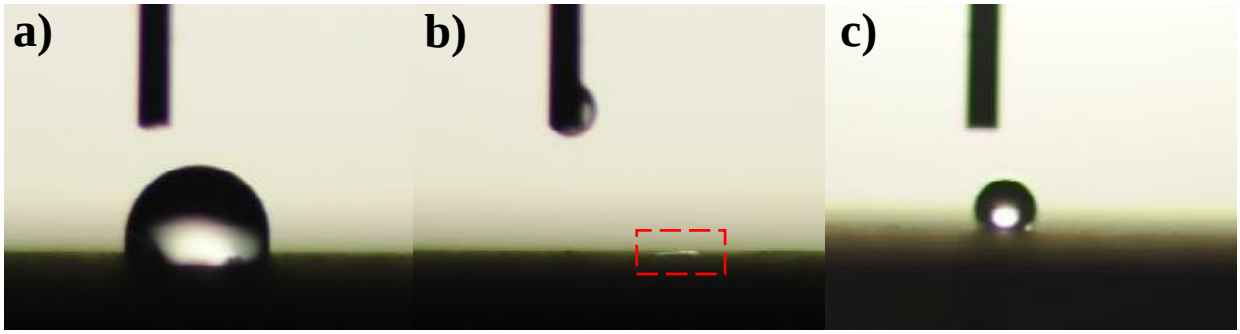

Figure 4.21: Water adhering to the surface after CAH measurement for a) stearic acid after 70 cycles, b) HMDSO coating after 70 cycles and c) HMDSO coating after 170 cycles.

Having observed a clear degradation of the balanced stack as a result of icing/deicing cycling, we will next explore the degradation mechanisms. Due to the nature of superhydrophobic surfaces, it must be that the degradation results from a change in the chemistry, the morphology, or both. Morphology was measured by interferometry and SEM, while chemical changes were observed by XPS. There were no changes to the surface visible by simply looking at the samples.

SEM images of the balanced stack before and after cycling can be seen in Figure 4.22. Some studies have suggested that the degradation of samples after icing is due to damage to the tips of asperities and a loss of their nano-scale surface features [113], however, this does not seem to be the principle mechanism of degradation for our samples. Looking at the samples after cycling, we see sub-

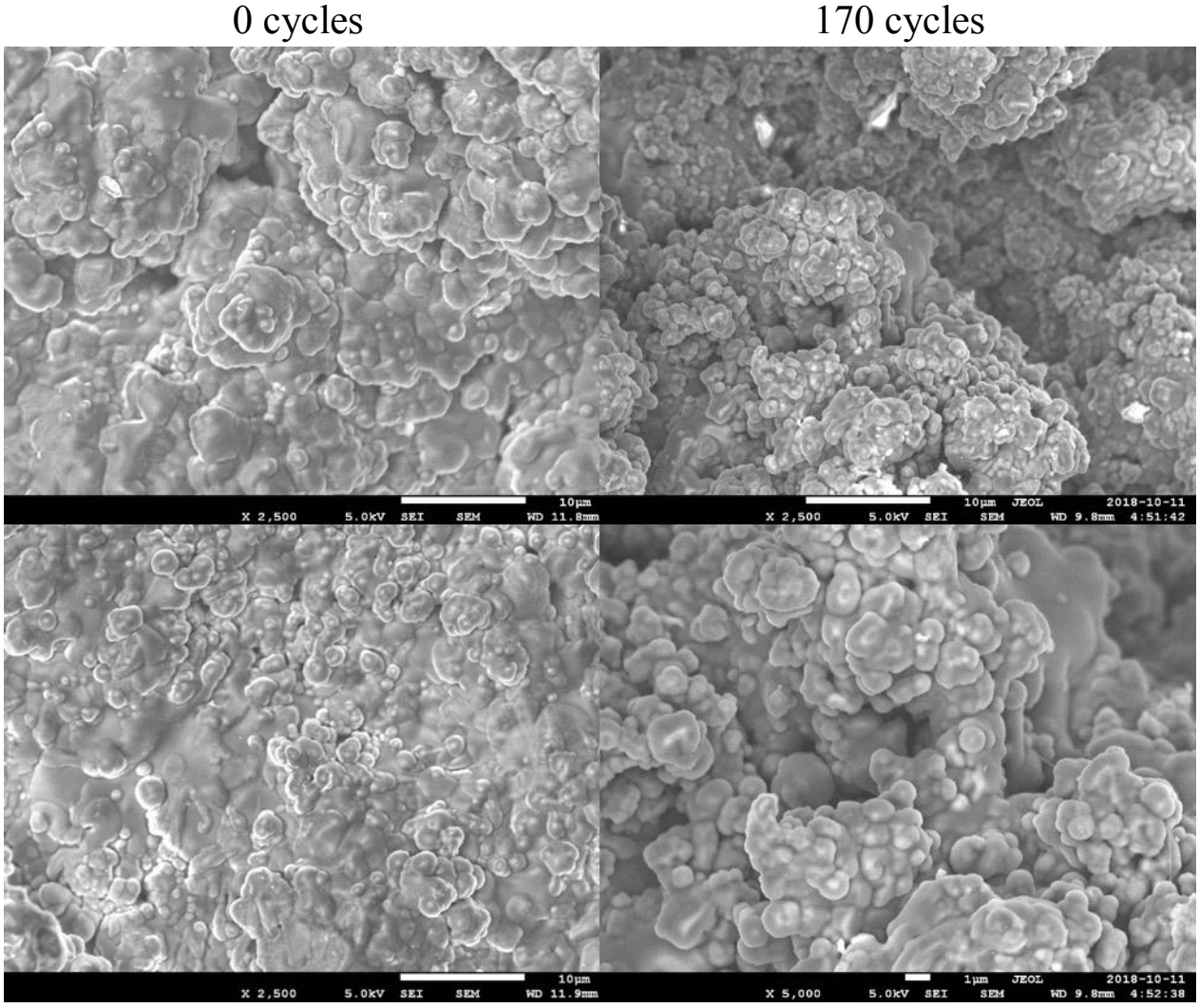

Figure 4.22: SEM images of the balanced stack sample before (left) and after (right) 170 icing/deicing cycles.

micron features still present at the top of the micro-features, and there is not a major decrease in the number of these features compared to what was seen before cycling. While we can see some differences in the images before and after cycling, it is not the extreme level of change which has been shown for some highly-damaged samples (e.g. Figure 2.29). Instead, the changes are similar to what has been shown by others when degradation is primarily chemical (e.g. Figure 2.34).

More definitive results were seen for the stearic acid coatings (Figure 4.23). Prior to cycling we see some dark areas along the surface, but after 170 cycles the surface is littered with dark spots. This corresponds with the degradation of the stearic acid coating and is likely due to its removal.

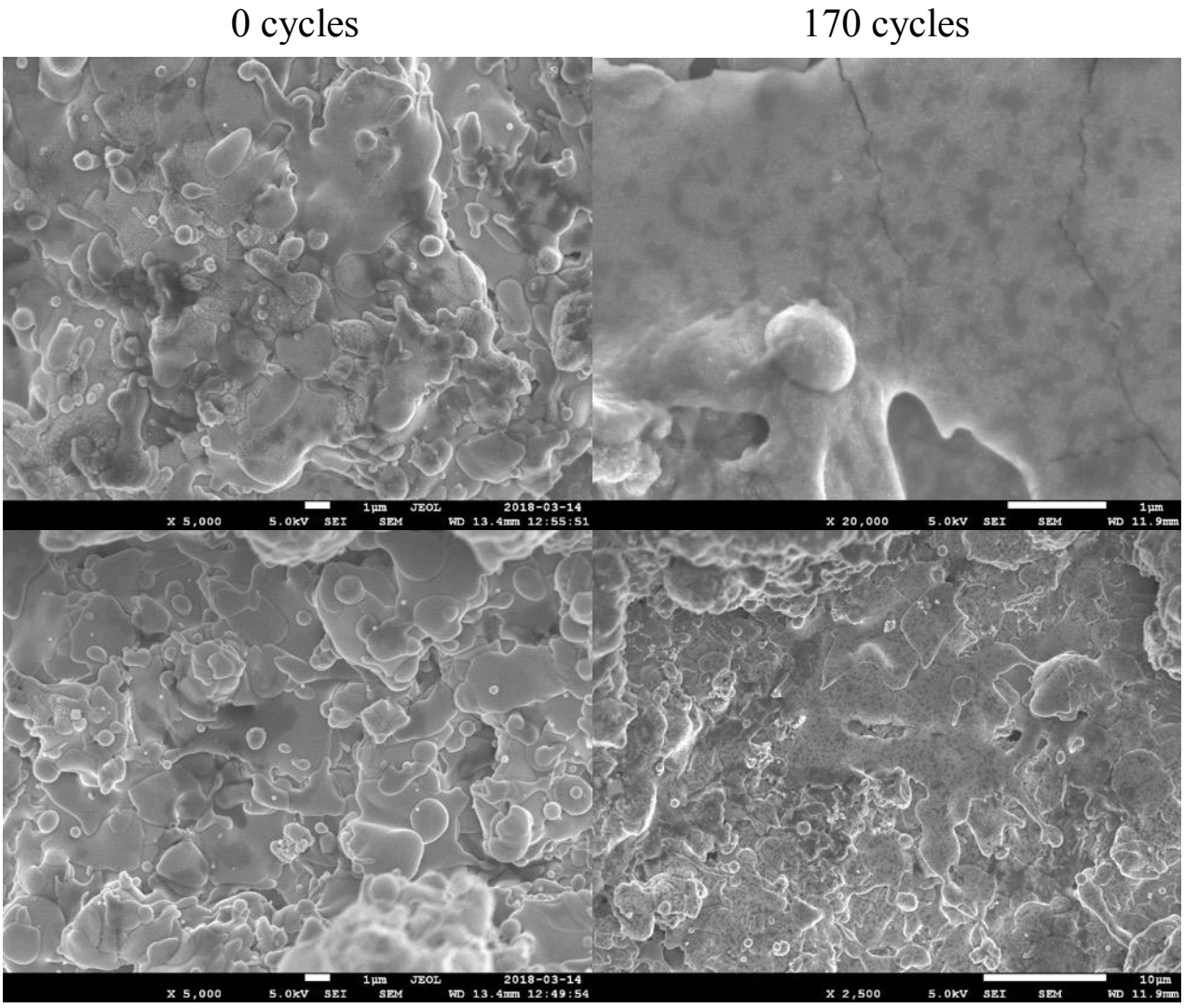

Figure 4.23: SEM images of the stearic acid sample before (left) and after (right) 170 icing/deicing cycles.

Looking at the roughness properties of our surface, presented in Table 4.12, there is no indication of a statistically significant change after cycling. It should be noted that this test would not be sensitive enough to measure damage to the coating, as it could not determine a meaningful difference between coated and non-coated samples, however, any change to the micro-scale features would manifest itself in these values.

Table 4.12: Roughness properties of the balanced stack before and after cycling.

Sample	**S_a**	**S_z**	**S_{sk}**	**S_{ku}**
Balanced stack - Before	10.3 ± 0.9	63 ± 6	0.59 ± 0.05	2.59 ± 0.08
Balanced Stack - After	11 ± 1	67 ± 5	0.53 ± 0.07	2.54 ± 0.07

Having not found the culprit for our sample's degradation by looking at its morphology, we move onto the chemistry. XPS was performed on balanced stack samples before coating, as well as after 100 and 170 cycles. Measurements were also taken for a TiO_2 sample coated with the DLC:SiO_x balanced coating, but without the HMDSO topcoat. The results from survey scans and high-resolution scans of these samples can be found in Table 4.13 and Table 4.14, respectively. It should be noted that for the balanced stack, the XPS measurements correspond to the 100nm HMDSO layer at the surface and not the balanced DLC:SiO_x layer below, since the penetration depth of the XPS measurements is below 10nm.

The survey scans show that the silicon content is greater than that of oxygen for both the balanced DLC:SiO_x and the full balanced stack with HMDSO topcoat. This corresponds with what has been shown in the literature, where it was said that a O:Si ratio below 1 is best for the hydrophobicity of this type of coating when deposited by PECVD [102]. As the balanced stack is cycled, however, an increase in carbon is seen at the expense of silicon, while oxygen content remains almost constant. This puts the O/Si ratio above 1, and is the first measurable sign of degradation for our surfaces. Also seen in the scans of the cycled samples is a small amount of calcium and fluorine contamination. Their provenance is uncertain.

Name	BE (eV)	At. %			
		DLC:SiO_x	**Balanced Stack**	**100 cycles**	**170 cycles**
Si2p	102.1	27.5	25.4	18.2	19.3
C1S	285.1	50.9	54.6	59.0	59.7
Ca2p	348.3	---	---	0.2	0.8
O1s	533.0	21.5	20.0	19.7	19.7
F1s	690.2	---	---	2.9	0.6

Table 4.13: Identification and quantification of elements from XPS survey scans

Table 4.14: Identification of chemical bonding from high resolution XPS scans

Name	BE (eV)	Identification	At. %			
			DLC:SiO_x	**Balanced Stack**	**100 cycles**	**170 cycles**
Si2p	100.7	$(CH_3)_6Si_2O$	---	5.2	3.4	3.9
	101.2	$(CH_3)_3SiOH$	6.1	---	---	---
	102.3	$(CH_3)_5Si_2O_2$	13.7	17.4	12.9	13.1
	103.1	SiO_2	4.9	---	---	---
C1s	284.6-284.9	C-Si	22.2	55.7	40.4	39.2
	285.4-285.8	C-C	28.4	---	20.0	20.9
	288.9	O-C=O	---	---	1.1	1.0
O1s	532.4-532.9	Si-O	24.8	21.6	22.2	21.9

The high resolution scans give further information on the degradation during cycling, as well as the difference between the DLC:SiO_x coating and the HMDSO layer. Perhaps most notable is the fact that the DLC:SiO_x coating has a measurable SiO_2 and $(CH_3)_3SiOH$ content which is not seen

in the other samples. This suggests that, as was suspected from the contact angle and hysteresis degradation, the HMDSO coating is not being removed or pierced; otherwise, we would see the SiO_2 and $(CH_3)_3SiOH$ from the DLC:SiO_x layer in the cycled samples. In terms of the degradation which is seen, the same drop in silicon which was seen in the survey scans is also seen here for the cycled samples, while oxygen content remains nearly constant. A decrease in the C-Si peak, the most likely indicator of the presence of methyl groups, is seen for the cycled samples, while the apparition of a C-C peak comes from exposure of the surface to air. No C-C peak is seen for the non-cycled balanced stack; this could due to its lower concentration compared to the C-Si groups. A C-C peak is also seen for the DLC:SiO_x surface, and in this case could indicate surface contamination or could be from the presence of amorphous carbon. Finally, an O-C=O peak is present for the cycled samples, which could be due to surface contamination or a modification of the surfaces due to cycling; in either case, the presence of this oxygen at the surface would correspond with the decrease in water repellency of the cycled samples.

4.5 General discussion

The coatings developed in this work have proven to be icephobic and have shown superior durability over simple TiO_2/stearic acid coatings. With that said, there are few points which merit further discussion.

Beginning with the ice adhesion results, it is quite curious to see the much larger value for the hard stack in the mixed/glaze icing condition, especially considering that the same 100 nm of HMDSO is used as top layer of all stacks. As a guess, this is likely due to some difference in the morphology of the TiO_2 coating compared to that of the balanced stack sample. This could be retested by depositing a new sample with the hard stack and remeasuring ice adhesion in the mixed/glaze condition. This is not a case of one errant measurement, as four measurements in this icing condition were quite evenly spread between 75 and 350 kPa. It is also likely not a case of this specific sample having been damaged or contaminated, as some other Phobic2Ice samples were also shown to struggle in this icing condition.

Looking at the rain erosion results, we see a clear improvement when comparing the hard stack to the balanced stack. Because of this, it may be interesting to perform rain erosion on stacks using some of the harder, lightly hydrophilic DLC:SiO_x coatings (e.g. the coating with a hardness of 14.6

GPa and CA of 85 ° seen in Table 4.2). Sharifi *et al.*[45] have shown that some degree of reentrant topography is present for the type of SPS TiO_2 coatings used in this work, and as such it is very possible that these surfaces would become superhydrophobic even when coated with lightly hydrophilic materials.

The biggest points of discussion concern the icing/deicing cycling. It should first be noted that the icing/deicing cycles which we performed consisted of deicing by melting (there is no ice adhesion rig at Concordia University where the IWT tests were performed). After applying heat to the iced samples, a liquid layer would form at the ice-substrate interface, and ice would slide off under its own weight. Removing ice by melting was shown in one work to be less damaging to the surface than removing it by a shearing force [78], however, ice formation in that case was performed by freezing water to the surface using a mold, and not by the high-velocity impact of supercooled water droplets. Because of this, it is difficult to compare the damage done to our samples to those seen in the literature. Golovin *et al.* [19] do offer degradation results for a surface treated with NeverWet which could potentially be used as a point of comparison, however, this degradation is reported only in terms of increasing ice adhesion, rather than wettability of the surface. In general, it is expected that our surfaces would degrade faster if ice was sheared from the samples rather than being removed by melting.

XPS measurements confirmed that the HMDSO layer on the balanced stack is not pierced or removed during cycling, and so it is curious to see that there was any droplet sticking at all for the SiN_x/HMDSO stack, since there was no sticking seen for the balanced stack, and the two should be chemically identical at the surface. It is very difficult to say what exactly the cause was, as these samples were cycled together, and no abnormalities were seen during their cycling. It is possible that a small bit of ice got caught in the airflow and impacted the sample, damaging the coating. Further testing could show whether or not such degradation is typical for this type of surface.

It can be said, however, that this damage did not have a large effect on the contact angle hysteresis results for this sample. This is because the damage was contained to a very small area, and in most cases when droplet sticking was seen, it was at a point of droplet retraction where the effects of the needle on the shape of the droplet already precluded these video frames from being used. This lack of effect can be seen when looking at the uncertainty values for the HMDSO stack in Figure 4.20, which are very similar to the balanced stack. In fact, there was only one set of measurements where

the damaged location gave the highest hysteresis value: after 160 cycles, when the location of droplet sticking gave a hysteresis value of 48 ° compared to values of 25 °, 34 °, and 40 ° measured elsewhere on the surface.

Speaking more generally about degradation, droplets tended to stick when CAH values were above ~45 °. With a CAH of 33 ± 4° after 170 cycles, droplets could still be easily removed from the balanced stack sample by tilting it; the same was true of the HMDSO-only stack for droplets which did not stick. A simple linear regression of the balanced stack CAH values suggests that average CAH would reach 45 ° after 235 icing/deicing cycles.

Finally, when discussing durability, it is important to note the context. Due to the requirement of hydrophobicity for the DLC:SiO_x films, a maximum hardness of 11 GPa was achieved. Additionally, the thickness of the thin coating stack was limited to 500 nm in order to maintain superhydrophobicity of the surface, and only 250 nm of this is DLC:SiO_x. While the developed coating system vastly outperformed a TiO_2/stearic acid system in rain erosion tests, both the hardness and thickness values fall well below the 20 GPa and 8 µm values generally recommended for coatings resistant to solid particle erosion [114]. Thus, the presented solution can be considered to be durable in the context of icephobic coatings, but not in the larger context of high-hardness and erosion-resistant coatings.

CHAPTER 5 CONCLUSIONS AND FURTHER SUGGESTIONS

A durable thin-on-thick icephobic coating system has been developed through suspension plasma spray deposition of ~50 µm of TiO_2, followed by plasma enhanced chemical vapor deposition of 150 nm of SiN_x, 250 nm of DLC:SiO_x, and 100 nm of PP-HMDSO; the coating system achieves icephobicity via superhydrophobicity. The hydrophobic "thin" coatings developed in this work had flat-surface contact angles up to 97 ± 1 ° and 109.0 ± 2 ° for the DLC:SiO_x and PP-HMDSO, respectively, and when deposited on hierarchically rough TiO2 surfaces, contact angles for the entire coating system were as high as 156.3 ± 0.4 °, with contact angles hysteresis values as low as 3.8 ± 0.4 °. The developed coating system was able to consistently satisfy the requirements for superhydrophobicity.

Balanced and hard configurations of the coating system were developed, differentiated by the hardness and wettability of the DLC:SiO_x layer. The icephobicity of this system has been confirmed through ice adhesion measurements, with values as low as 62 ± 27 kPa. In rain erosion tests, the best samples showed no change in wettability even after 6000 droplet impacts. Icing/deicing cycles showed that the coating system did degrade after repeated cycling, but had no droplets stick to the surface during contact angle and contact angle hysteresis measurements, even after 170 cycles. The degradation seen after cycling was shown to be predominantly chemical rather than morphological, and the HMDSO topcoat was neither removed nor pierced in these tests. Methods of "rejuvenating" the surface, such as spraying with stearic acid after multiple cycles, have been discussed and may be explored in the future.

As part of the Phobic2Ice project, the balanced and hard stacks have been selected to undergo a series of addition tests over the next six months. These include salt fog corrosion, UV light resistance, and thermal cycling. Both stacks will also be tested at the large-scaling icing wind tunnel operated by the National Research Council in Ottawa, Ontario. A unique rig built to assess the icing of rotating aircraft parts will be used, and ice adhesion and degradation of the samples will be tested using various icing conditions. Finally, the balanced stack has been selected for flight tests to be performed during the Winter/Spring icing season of 2019 in Madrid, Spain. These will provide a true measure of the icephobicity of our coatings in flight conditions and will confirm whether they are able to withstand the harsh conditions seen by aircraft flying through icing clouds.

Beyond this, there are additional characterization steps which would aid in fully understanding the developed coatings. The balanced stack should continue to be cycled until complete failure, as the data indicates that this may occur within the next 65 cycles. Also of interest is solid particle erosion of the hard and balanced DLC:SiO_x coatings. While the 250 nm films used in this work would be destroyed almost instantly, erosion rates could be determined for thicker films (~10 µm) deposited on flat substrates, allowing for a better understanding of the difference in durability between the hard and balanced coatings. Finally, it would be highly interesting to see the ice adhesion and durability of a surface where the patterns themselves are made from the DLC:SiO_x films developed in this work. This could be performed by depositing thick films and patterning them by etching, or by depositing through a mask to create DLC:SiO_x structures on a substrate surface. These of course will present their own difficulties, such as changes to the surface chemistry after etching, or how to obtain nano-scale features on the smooth DLC:SiO_x structures; these challenges will be left to another student.

BIBLIOGRAPHY

[1] F. G. Shaw, “Devices to keep railroad switches from becoming clogged with snow and ice,” *Eng. News*, 1906.

[2] W. J. B. Wilson, “Failure of steel ship-plates,” *Engineering*, vol. 98, pp. 714–715, 1914.

[3] W. Fawcett, “Winter obstacles to transportation,” *Sci. Am.*, 1903.

[4] C. G. Andrus, “The problem of combating ice accumulation,” *Aviation*, vol. 24, no. 16, p. 975103010321034-, 1928.

[5] F. R. Neely, “The serious menace known as ice on the plane,” *United States Air Serv. -- Publ.*, vol. 13, no. 5, pp. 31–32, 1928.

[6] T. Carroll and W. H. McAvoy, “The formation of ice upon exposed parts of an airplane in flight,” *United States Natl. Advis. Comm. Aeronaut. -- Tech. Memo. Notes*, p. 10-, 1928.

[7] B. Landsberg, “AOPA Safety Advisor: Aircraft Icing,” AOPA Air Safety Foundation, Frederick, MD, p. 2, 2008.

[8] Z. Wang, “Recent progress on ultrasonic de-icing technique used for wind power generation, high-voltage transmission line and aircraft,” *Energy Build.*, vol. 140, pp. 42–49, Apr. 2017.

[9] B. M. Pobanz, J. D. Marwitz, and M. K. Politovich, “Conditions associated with large-drop regions,” *J. Appl. Meteorol.*, vol. 33, no. 11, pp. 1366–1372, 1994.

[10] M. J. Kittler, “A non-icing fully maneuverable aircraft carburetor,” in *SAE Technical Papers*, 1939.

[11] R. W. Gent, N. P. Dart, and J. T. Cansdale, “Aircraft icing,” *Philos. Trans. R. Soc. London A Math. Phys. Eng. Sci.*, vol. 358, no. 1776, pp. 2873–2911, 2000.

[12] K. R. Petty and C. D. J. Floyd, “A Statistical Review of Aviation Airframe Icing Accidents in the US,” in *Proceedings of the 11th Conference on Aviation, Range, and Aerospace Hyannis*, 2004.

[13] L. Mazzola, “Aeronautical livery coating with icephobic property,” *Surf. Eng.*, vol. 32, no. 10, pp. 733–744, 2016.

[14] *Aviation Maintenance Technician Handbook- Airframe Handbook*, vol. 2. Oklahoma City,

OK: United States Department of Transportation, Federal Aviation Administration, 2018.

[15] Q. Su, S. Chang, Y. Zhao, H. Zheng, and C. Dang, "A review of loop heat pipes for aircraft anti-icing applications," *Appl. Therm. Eng.*, vol. 130, pp. 528–540, Feb. 2018.

[16] L. Mishchenko, B. Hatton, V. Bahadur, J. A. Taylor, T. Krupenkin, and J. Aizenberg, "Design of ice-free nanostructured surfaces based on repulsion of impacting water droplets," *ACS Nano*, vol. 4, no. 12, pp. 7699–7707, 2010.

[17] N. A. Goldberger., "Winter calls for de-icing," 2010. [Online]. Available: https://www.176wg.ang.af.mil/Media/Article-Display/Article/444167/winter-calls-for-de-icing/. [Accessed: 29-Oct-2018].

[18] M. J. Kreder, J. Alvarenga, P. Kim, and J. Aizenberg, "Design of anti-icing surfaces: smooth, textured or slippery?," *Nat. Rev. Mater.*, vol. 1, no. 1, p. 15003, 2016.

[19] K. Golovin, S. P. R. Kobaku, D. H. Lee, E. T. DiLoreto, J. M. Mabry, and A. Tuteja, "Designing Durable Icephobic Surfaces," *Sci. Adv.*, vol. 2, no. 3, pp. 1–12, 2016.

[20] Y. Cheng and D. E. Rodak, "Is the lotus leaf superhydrophobic ?," vol. 144101, no. May 2013, 2005.

[21] W. Barthlott and C. Neinhuis, "Purity of the sacred lotus, or escape from contamination in biological surfaces," *Planta*, vol. 202, no. 1, pp. 1–8, 1997.

[22] M. Mohammadi, D. De Pauw, M. Tembely, and A. Dolatabadi, "Droplet Impact and Solidification on Hydrophilic and Superhydrophobic Substrates in Icing Conditions," *43rd AIAA Fluid Dyn. Conf.*, p. 2486, 2013.

[23] S. A. Kulinich and M. Farzaneh, "How wetting hysteresis influences ice adhesion strength on superhydrophobic surfaces," *Langmuir*, vol. 25, no. 16, pp. 8854–8856, 2009.

[24] M. Nosonovsky and V. Hejazi, "Why superhydrophobic surfaces are not always icephobic," *ACS Nano*, vol. 6, no. 10, pp. 8488–8491, 2012.

[25] P. Irajizad, M. Hasnain, N. Farokhnia, S. M. Sajadi, and H. Ghasemi, "Magnetic slippery extreme icephobic surfaces," *Nat. Commun.*, vol. 7, no. May, pp. 1–7, 2016.

[26] T. Young, "An Essay on the Cohesion of Fluids," *Philos. Trans. R. Soc. London*, vol. 95, no. 0, pp. 65–87, 1805.

[27] R. Said *et al.*, “Effects of Bias Voltage on Diamond Like Carbon Coatings Deposited Using Titanium Isopropoxide (TIPOT) and Acetylene / Argon Mixtures onto Various Substrate Materials,” *J. Nanosci. Nanotechnol.*, vol. 10, no. 4, pp. 2552–7, 2010.

[28] ASTM-D7490, “Standard Test Method for Measurement of the Surface Tension of Solid Coatings, Substrates and Pigments using Contact Angle Measurements.” ASTM International, West Conshohocken, PA, 2013.

[29] A. Tuteja, W. Choi, G. H. McKinley, R. E. Cohen, and M. F. Rubner, “Design parameters for superhydrophobicity and superoleophobicity,” *MRS Bull.*, vol. 33, no. 8, pp. 752–758, 2008.

[30] E. G. Shafrin and W. A. Zisman, “Upper Limits to the Contact Angles of Liquids on Solids,” in *Contact Angle, Wettability, and Adhesion*, Washington, DC: AMERICAN CHEMICAL SOCIETY, 1964.

[31] F. Schulman and W. A. Zisman, “The spreading of liquids on low energy surfaces, V. Perfluorodecanoic Acid Monolayers,” *J. Colloid. Sci.*, vol. 5, no. 5, p. 465, Oct. 1952.

[32] R. N. Wenzel, “RESISTANCE OF SOLID SURFACES TO WETTING BY WATER,” *Ind. Eng. Chem.*, vol. 28, no. 8, pp. 988–994, 1936.

[33] B. Bhushan and E. K. Her, “Fabrication of superhydrophobic surfaces with high and low adhesion inspired from rose petal,” *Langmuir*, vol. 26, no. 11, pp. 8207–8217, 2010.

[34] A. B. D. Cassie and S. Baxter, “Wettability of Porous Surfaces,” *Trans. Faraday Soc.*, vol. 40, no. 0, pp. 546–551, 1944.

[35] B. Bhushan, Y. C. Jung, and K. Koch, “Micro-, nano- And hierarchical structures for superhydrophobicity, self-cleaning and low adhesion,” *Philos. Trans. R. Soc. A Math. Phys. Eng. Sci.*, vol. 367, no. 1894, pp. 1631–1672, 2009.

[36] M. Nosonovsky and B. Bhushan, “Biomimetic superhydrophobic surfaces: Multiscale approach,” *Nano Lett.*, vol. 7, no. 9, pp. 2633–2637, 2007.

[37] L. Gao and T. J. Mccarthy, “The ‘Lotus Effect’ Explained : Two Reasons Why Two Length Scales of Topography Are Important,” *Langmuir*, vol. 22, no. 7, pp. 2966–2967, 2006.

[38] A. Marmur, C. Della Volpe, S. Siboni, A. Amirfazli, and J. W. Drelich, “Contact angles and

wettability: towards common and accurate terminology," *Surf. Innov.*, vol. 5, no. 1, pp. 3–8, 2017.

[39] T. Huhtamäki, X. Tian, J. T. Korhonen, and R. H. A. Ras, "Surface-wetting characterization using contact-angle measurements," *Nat. Protoc.*, vol. 13, no. 7, pp. 1521–1538, 2018.

[40] B. Bhushan and M. Nosonovsky, "The rose petal effect and the modes of superhydrophobicity," *Philos. Trans. R. Soc. A Math. Phys. Eng. Sci.*, vol. 368, no. 1929, pp. 4713–4728, 2010.

[41] M. Cao and L. Jiang, "Superwettability integration: concepts, design and applications," *Surf. Innov.*, vol. 4, no. 4, pp. 180–194, 2016.

[42] L. B. Boinovich and A. M. Emelyanenko, "Anti-icing potential of superhydrophobic coatings," *Mendeleev Commun.*, vol. 23, no. 1, pp. 74–75, Jan. 2013.

[43] R. Zhang, P. Hao, X. Zhang, and F. He, "Supercooled water droplet impact on superhydrophobic surfaces with various roughness and temperature," *Int. J. Heat Mass Transf.*, vol. 122, pp. 395–402, 2018.

[44] J. Liu *et al.*, "Hydrophobic/icephobic coatings based on thermal sprayed metallic layers with subsequent surface functionalization," *Surf. Coatings Technol.*, vol. 357, no. October 2018, pp. 267–272, 2019.

[45] N. Sharifi, F. Ben Ettouil, C. Moreau, A. Dolatabadi, and M. Pugh, "Engineering surface texture and hierarchical morphology of suspension plasma sprayed TiO2coatings to control wetting behavior and superhydrophobic properties," *Surf. Coatings Technol.*, vol. 329, no. September, pp. 139–148, 2017.

[46] N. Xi *et al.*, "Steady anti-icing coatings on weathering steel fabricated by HVOF spraying," *Appl. Surf. Sci.*, vol. 444, pp. 757–762, 2018.

[47] T. B. Nguyen, S. Park, and H. Lim, "Effects of morphology parameters on anti-icing performance in superhydrophobic surfaces," *Appl. Surf. Sci.*, vol. 435, pp. 585–591, 2018.

[48] D. A. Del Cerro, G. R. B. E. Römer, A. J. Huis In't Veld, G. R. B. E. Römer, and A. J. Huis In't Veld, "Erosion resistant anti-ice surfaces generated by ultra short laser pulses," *Phys. Procedia*, vol. 5, no. PART 1, pp. 231–235, 2010.

[49] S.-C. Cha *et al.*, “Thermal stability of superhydrophobic, nanostructured surfaces,” *J. Colloid Interface Sci.*, vol. 391, pp. 152–157, Feb. 2013.

[50] B. Bhushan, M. Nosonovsky, and Y. C. Jung, “Lotus Effect: Roughness-Induced Superhydrophobic Surfaces,” in *Nanotribology and Nanomechanics: An Introduction*, Berlin, Heidelberg: Springer Berlin Heidelberg, 2008, pp. 995–1072.

[51] U. U. Ghosh, S. Nair, A. Das, R. Mukherjee, and S. DasGupta, “Replicating and resolving wetting and adhesion characteristics of a Rose petal,” *Colloids Surfaces A Physicochem. Eng. Asp.*, vol. 561, pp. 9–17, Jan. 2019.

[52] S. Baxter and A. B. D. Cassie, “THE WATER REPELLENCY OF FABRICS AND A NEW WATER REPELLENCY TEST,” *J. Text. Inst. Trans.*, vol. 36, no. 4, pp. T67–T90, 1945.

[53] G. D. Yarnold and B. J. Mason, “A Theory of the Angle of Contact,” *Proc. Phys. Soc. Sect. B*, vol. 62, no. 2, p. 121, 1949.

[54] L. Cao, H. A. Hu, and D. Gao, “Design and fabrication of micro-textures for inducing a superhydrophobic behavior on hydrophilic materials,” *Langmuir*, vol. 23, no. 8, pp. 4310–4314, 2007.

[55] K. Golovin, M. Boban, J. M. Mabry, and A. Tuteja, “Designing Self-Healing Superhydrophobic Surfaces with Exceptional Mechanical Durability,” *ACS Appl. Mater. Interfaces*, vol. 9, no. 12, pp. 11212–11223, 2017.

[56] N. Sharifi, M. Pugh, C. Moreau, and A. Dolatabadi, “Developing hydrophobic and superhydrophobic TiO2 coatings by plasma spraying,” *Surf. Coatings Technol.*, vol. 289, pp. 29–36, 2016.

[57] “Quatrième séance - Travaux de la Section de Thermométrie,” in *Comptes Rendus des séances de la dixième conference generale despoids et mesures*, 1954, vol. 10.

[58] E. B. Moore and V. Molinero, “Structural transformation in supercooled water controls the crystallization rate of ice,” *Nature*, vol. 479, p. 506, Nov. 2011.

[59] M. K. Politovich, “Response of a research aircraft to icing and evaluation of severity indices,” *J. Aircr.*, vol. 33, no. 2, pp. 291–297, Mar. 1996.

[60] G. Mingione, M. Barocco, E. Denti, and F. G. Bindi, “Flight in icing conditions,” 1997.

[61] Y. Hu *et al.*, "Occurrence, liquid water content, and fraction of supercooled water clouds from combined CALIOP/IIR/MODIS measurements," *J. Geophys. Res. Atmos.*, vol. 115, no. D4.

[62] "Gridded Population of the World (GPW), v4," *CIESIN at Columbia University*, 2015. [Online]. Available: http://sedac.ciesin.columbia.edu/data/collection/gpw-v4. [Accessed: 13-Nov-2018].

[63] H. Koivuluoto, C. Stenroos, M. Kylmälahti, M. Apostol, J. Kiilakoski, and P. Vuoristo, "Anti-icing Behavior of Thermally Sprayed Polymer Coatings," *J. Therm. Spray Technol.*, vol. 26, no. 1–2, pp. 150–160, 2017.

[64] J. R. Stallabrass and R. D. Price, "On the adhesion of ice to various materials," 1962.

[65] V. Hejazi, K. Sobolev, and M. Nosonovsky, "From superhydrophobicity to icephobicity: forces and interaction analysis," *Sci. Rep.*, vol. 3, p. 2194, Jul. 2013.

[66] R. R. Blackburn, C. G. Schmidt, M. Park, and B. J. Kinzig, "Ice-Pavement Bond Disbonding -- Fundamental Study," Washington, DC, 1993.

[67] L. Zhu, J. Xue, Y. Wang, Q. Chen, J. Ding, and Q. Wang, "Ice-phobic Coatings Based on Silicon-Oil-Infused Polydimethylsiloxane," *ACS Appl. Mater. Interfaces*, vol. 5, no. 10, pp. 4053–4062, May 2013.

[68] S. A. Kulinich and M. Farzaneh, "Ice adhesion on super-hydrophobic surfaces," *Appl. Surf. Sci.*, vol. 255, no. 18, pp. 8153–8157, Jun. 2009.

[69] Z. He, S. Xiao, H. Gao, J. He, and Z. Zhang, "Multiscale crack initiator promoted super-low ice adhesion surfaces," *Soft Matter*, vol. 13, no. 37, pp. 6562–6568, 2017.

[70] A. J. Meuler, J. D. Smith, K. K. Varanasi, J. M. Mabry, G. H. McKinley, and R. E. Cohen, "Relationships between water wettability and ice adhesion," *ACS Appl. Mater. Interfaces*, vol. 2, no. 11, pp. 3100–3110, 2010.

[71] M. Susoff, K. Siegmann, C. Pfaffenroth, and M. Hirayama, "Evaluation of icephobic coatings - Screening of different coatings and influence of roughness," *Appl. Surf. Sci.*, vol. 282, pp. 870–879, Oct. 2013.

[72] Y. Wang, J. Liu, M. Li, Q. Wang, and Q. Chen, "The icephobicity comparison of polysiloxane modified hydrophobic and superhydrophobic surfaces under condensing environments," *Appl. Surf. Sci.*, vol. 385, pp. 472–480, 2016.

[73] P. W. Wilson *et al.*, "Inhibition of ice nucleation by slippery liquid-infused porous surfaces (SLIPS)," *Phys. Chem. Chem. Phys.*, vol. 15, no. 2, pp. 581–585, 2013.

[74] S. Ozbay and H. Y. Erbil, "Ice accretion by spraying supercooled droplets is not dependent on wettability and surface free energy of substrates," *Colloids Surfaces A Physicochem. Eng. Asp.*, vol. 504, pp. 210–218, 2016.

[75] M. A. Sarshar, C. Swarctz, S. Hunter, J. Simpson, and C.-H. Choi, "Effects of contact angle hysteresis on ice adhesion and growth on superhydrophobic surfaces under dynamic flow conditions," *Colloid Polym. Sci.*, vol. 291, no. 2, pp. 427–435, Feb. 2013.

[76] P. Guo, Y. Zheng, M. Wen, C. Song, Y. Lin, and L. Jiang, "Icephobic/anti-icing properties of micro/nanostructured surfaces," *Adv. Mater.*, vol. 24, no. 19, pp. 2642–2648, 2012.

[77] R. Jafari, R. Menini, and M. Farzaneh, "Superhydrophobic and icephobic surfaces prepared by RF-sputtered polytetrafluoroethylene coatings," *Appl. Surf. Sci.*, vol. 257, no. 5, pp. 1540–1543, 2010.

[78] Y. Wang, J. Xue, Q. Wang, Q. Chen, and J. Ding, "Verification of Icephobic/Anti-icing Properties of a Superhydrophobic Surface," *ACS Appl. Mater. Interfaces*, vol. 5, no. 8, pp. 3370–3381, Apr. 2013.

[79] S. Farhadi, M. Farzaneh, and S. A. Kulinich, "Anti-icing performance of superhydrophobic surfaces," *Appl. Surf. Sci.*, vol. 257, no. 14, pp. 6264–6269, 2011.

[80] L. Foroughi Mobarakeh, R. Jafari, and M. Farzaneh, "The ice repellency of plasma polymerized hexamethyldisiloxane coating," *Appl. Surf. Sci.*, vol. 284, pp. 459–463, 2013.

[81] K. Chen and T. Sun, "Effects of microstructure design on aluminum surface hydrophobic and ice-retarding properties," *Asia-Pacific J. Chem. Eng.*, vol. 12, no. 2, pp. 307–312, 2017.

[82] L. Foroughi Mobarakeh, R. Jafari, and M. Farzaneh, "Robust icephobic, and anticorrosive plasma polymer coating," *Cold Reg. Sci. Technol.*, vol. 151, no. March, pp. 89–93, 2018.

[83] E. Grimoldi, S. Zanini, R. A. Siliprandi, and C. Riccardi, "AFM and contact angle

investigation of growth and structure of pp-HMDSO thin films," *Eur. Phys. J. D*, vol. 54, no. 2, pp. 165–172, 2009.

[84] R. Jafari, L. F. Mobarakeh, and M. Farzaneh, "Water-repellency enhancement of nanostructured plasma-polymerized HMDSO coatings using grey-based taguchi method," *Nanosci. Nanotechnol. Lett.*, vol. 4, no. 3, pp. 369–374, 2012.

[85] Y.-Y. Ji, Y.-C. Hong, S.-H. Lee, S.-D. Kim, and S.-S. Kim, "Formation of super-hydrophobic and water-repellency surface with hexamethyldisiloxane (HMDSO) coating on polyethyleneteraphtalate fiber by atmosperic pressure plasma polymerization," *Surf. Coatings Technol.*, vol. 202, no. 22–23, pp. 5663–5667, Aug. 2008.

[86] L. Foroughi Mobarakeh, R. Jafari, and M. Farzaneh, "Superhydrophobic Surface Elaboration Using Plasma Polymerization of Hexamethyldisiloxane (HMDSO)," *Adv. Mater. Res.*, vol. 409, pp. 783–787, 2011.

[87] S. Zanini *et al.*, "Surface properties of HMDSO plasma treated polyethylene terephthalate," *Surf. Coatings Technol.*, vol. 200, no. 1–4, pp. 953–957, Oct. 2005.

[88] Jynto, "Ball-and-stick model of the hexamethyldisiloxane molecule," *Wikimedia Commons*. [Online]. Available: https://commons.wikimedia.org/wiki/File:Hexamethyldisiloxane-3D-balls.png. [Accessed: 25-Feb-2016].

[89] J. Robertson, "Diamond-like amorphous carbon," *Mater. Sci. Eng. R Reports*, vol. 37, no. 4–6, pp. 129–281, May 2002.

[90] L. Martinu, O. Zabeida, and J. E. E. Klemberg-Sapieha, "Plasma-Enhanced Chemical Vapor Deposition of Functional Coatings," in *Handbook of Deposition Technologies for Films and Coatings*, William Andrew Publishing, 2010, pp. 392–465.

[91] R. Colaço, A. P. Serro, O. L. Eryilmaz, and A. Erdemir, "Micro-to-nano triboactivity of hydrogenated DLC films," *J. Phys. D. Appl. Phys.*, vol. 42, no. 8, 2009.

[92] O. L. Eryilmaz and A. Erdemir, "TOF-SIMS and XPS characterization of diamond-like carbon films after tests in inert and oxidizing environments," *Wear*, vol. 265, no. 1–2, pp. 244–254, Jun. 2008.

[93] M. L. Wu, K. Howard, K. Grannen, J. Gui, G. C. Rauch, and P. J. Sides, "Properties and

durability of thin a-C:H overcoats produced by plasma enhanced chemical vapor deposition," *Thin Solid Films*, vol. 377–378, pp. 249–253, 2000.

[94] T. D. Martin, "Raman spectroscopy of diamondlike carbon films deposited by plasma-assisted chemical vapor deposition," Carnegie Mellon University, Ann Arbor, 1995.

[95] S.-C. Lee, F.-C. Tai, and C.-H. Wei, "Correlation between sp2/sp3 Ratio or Hydrogen Content and Water Contact Angle in Hydrogenated DLC Film," *Mater. Trans.*, vol. 48, no. 9, pp. 2534–2538, 2007.

[96] M. I. Jones, I. R. McColl, D. M. Grant, K. G. Parker, and T. L. Parker, "Protein adsorption and platelet attachment and activation, on TiN, TiC, and DLC coatings on titanium for cardiovascular applications," *J. Biomed. Mater. Res.*, vol. 52, no. 2, pp. 413–421, 2000.

[97] M. Grischke, A. Hieke, F. Morgenweck, and H. Dimigen, "Variation of the wettability of DLC-coatings by network modification using silicon and oxygen," *Diam. Relat. Mater.*, vol. 7, no. 2–5, pp. 454–458, 1998.

[98] L. K. Randeniya *et al.*, "Incorporation of Si and SiOx into diamond-like carbon films: Impact on surface properties and osteoblast adhesion," *Acta Biomater.*, vol. 5, no. 5, pp. 1791–1797, 2009.

[99] Y. Rahmawan, M. W. Moon, K. S. Kim, K. R. Lee, and K. Y. Suh, "Wrinkled, dual-Scale structures of diamond-Like carbon (DLC) for superhydrophobicity," *Langmuir*, vol. 26, no. 1, pp. 484–491, 2010.

[100] J. C. Damasceno and S. S. Camargo, "Plasma deposition and characterization of silicon oxide-containing diamond-like carbon films obtained from CH4:SiH4:O2 gas mixtures," *Thin Solid Films*, vol. 516, no. 8, pp. 1890–1897, Feb. 2008.

[101] L. Zajíčková, V. Buršíková, V. Peřina, A. Macková, and J. Janča, "Correlation between SiOx content and properties of DLC:SiOx films prepared by PECVD," *Surf. Coatings Technol.*, vol. 174–175, pp. 281–285, Sep. 2003.

[102] Š. Meškinis and A. Tamulevičiene, "Structure, properties and applications of diamond like nanocomposite (SiOx containing DLC) films: A review," *Medziagotyra*, vol. 17, no. 4, pp. 358–370, 2011.

[103] P. L. Fauchais, J. V. R. Heberlein, and M. I. Boulos, “Overview of Thermal Spray,” in *Thermal Spray Fundamentals: From Powder to Part*, Boston, MA: Springer US, 2014, pp. 17–72.

[104] J. Petzing, J. Coupland, and R. Leach, “The Measurement of Rough Surface Topography using Coherence Scanning Interferometry,” NPL Measurement Good Practice Guide No. 116, 2010.

[105] R. Leach, L. Brown, J. Xiangqian, R. Blunt, M. Conroy, and D. Mauger, “Guide to the Measurement of Smooth Surface Topography using Coherence Scanning Interferometry,” NPL Measurement Good Practice Guide No. 108, 2008.

[106] D. Nečas and P. Klapetek, “Gwyddion: an open-source software for SPM data analysis,” *Cent. Eur. J. Phys.*, vol. 10, no. 1, pp. 181–188, Feb. 2012.

[107] ISO-25178, “Geometrical product specifications (GPS) — Surface texture: Areal — Part 2: Terms, definitions and surface texture parameters.” International Standards Organization, Geneva, 2012.

[108] F. Blateyron, “The Areal Field Parameters,” in *Characterisation of Areal Surface Texture*, R. Leach, Ed. Berlin, Heidelberg: Springer Berlin Heidelberg, 2013, pp. 15–43.

[109] A. F. Stalder, G. Kulik, D. Sage, L. Barbieri, and P. Hoffmann, “A snake-based approach to accurate determination of both contact points and contact angles,” *Colloids Surfaces A Physicochem. Eng. Asp.*, vol. 286, no. 1–3, pp. 92–103, Sep. 2006.

[110] G. M. Pharr and W. C. Oliver, “Measurement of Thin Film Mechanical Properties Using Nanoindentation,” *MRS Bull.*, vol. 17, no. 7, pp. 28–33, 1992.

[111] D. De Pauw, “Effect of a Superhydrophobic Coating on the Anti-Icing and De-Icing of an Airfoil,” Concordia University, 2014.

[112] E. F. Tobin, T. M. Young, D. Raps, and O. Rohr, “Comparison of liquid impingement results from whirling arm and water-jet rain erosion test facilities,” *Wear*, vol. 271, no. 9–10, pp. 2625–2631, Jul. 2011.

[113] S. A. Kulinich, S. Farhadi, K. Nose, and X. W. Du, “Superhydrophobic Surfaces: Are They Really Ice-Repellent?,” *Langmuir*, vol. 27, no. 1, pp. 25–29, Jan. 2011.

[114] E. Bousser, L. Martinu, and J. E. Klemberg-Sapieha, “Solid particle erosion mechanisms of hard protective coatings,” *Surf. Coatings Technol.*, vol. 235, pp. 383–393, Nov. 2013.